2006

Instantaneous Fourier Series Estimation

Yujuan Sun
Western University

Instantaneous Fourier Series Estimation

(Spine title: Instantaneous Fourier Series Estimation)

(Thesis format: Monograph)

by

Yujuan Sun

Graduate Program
in
Engineering Science
Department of Electrical and Computer Engineering

A thesis submitted in partial fulfillment
of the requirements for the degree of
Master of Engineering Science

Faculty of Graduate Studies
The University of Western Ontario
London, Ontario, Canada

THE UNIVERSITY OF WESTERN ONTARIO
FACULTY OF GRADUATE STUDIES

CERTIFICATE OF EXAMINATION

Chief Advisor:

Dr. Lyndon J. Brown

Advisory Committee:

Examining Board:

Dr. Serguei L. Primak

Dr. Ken McIsaac

Dr. J. M. Floryan

The thesis by

Yujuan Sun

entitled:

Instantaneous Fourier Series Estimation

is accepted in partial fulfillment of the

requirements for the degree of

Master of Engineering Science

Date: August 2, 2006

Chair of Examining Board
Dr. Hanif Ladak

ABSTRACT

This thesis presents two improved approaches to extend a periodic disturbance cancellation algorithm to achieve different desired goals in active noise control and resistance spot welding (RSW). The original algorithm is adopted from the internal model based frequency estimation and noise cancellation principle in the error feedback control field.

One improvement of the algorithm is made and applied for an acoustic duct system to increase the stable frequency band. A design method of adaptively tuning the two control gains with the estimated frequency is presented. Simulations show that the improved algorithm not only broadly increases the working frequency band of the system, but also decreases the worst case error with minimum loss of speed.

The other extension of the algorithm is interpreting its results as an instantaneous Fourier series. This is then used for online estimation of the dynamic resistance in the secondary circuit of a resistance spot welding machine by instantaneous Fourier decomposition. The Fourier decomposition system is developed behaving as a bandpass filter with notch filters. Simulations on synthesized data show good agreements between the estimates of the resistance and tip voltage magnitude and their respective known values. Application on experimental data gives very reasonable results.

Keywords: Active noise control; Resistance spot welding; Internal model; Frequency estimation; Noise cancellation; Feedback control; Acoustic duct; Dynamic resistance; Instantaneous Fourier decomposition; Bandpass filter; Notch filter.

ACKNOWLEDGEMENTS

I would like to gratefully acknowledge my supervisor, Professor Lyndon J. Brown, for accepting me as a graduate student and guiding me through the maze of literature on my research. No matter how vague the idea was, he was able to provide me with enough insights and support to bring the idea to maturation. It was a memorable experience to work with a mentor with such wisdom and graciousness.

I would also like to thank my course professors and peers for their invaluable references and suggestions on my study and research.

I also want to express my thanks to those who provided excellent services and made Western a great experience, academic and otherwise.

The last but not the least, I would like to thank my husband, Xiangjun Song, and my lovely son, Michael, for their constant love, encouragement and support throughout the years.

TABLE OF CONTENTS

1. The content of this chapter is truncated from a paper submitted for review.
Lyndon Brown and Yujuan Sun, "Tuning to Stabilize Adaptive Internal Model Controller for Periodic Disturbance Cancellation", *Proc. 45th IEEE Conference on Decision and Control.*

LIST OF TABLES

LIST OF FIGURES

ABBREVIATIONS

ARMA	Autoregressive-Moving-Average
ASTFT	Adaptive Short-time Fourier Transform
EMD	Empirical Mode Decomposition
FFT	Fast Fourier Transformation
FT	Fourier Transform
HT	Hilbert Transform
HHT	Hilbert-Huang Transform
IF	Instantaneous Frequency
IFD	Instantaneous Fourier Decomposition
IM	Internal Model
IMC	Internal Model Controller
IMF	Intrinsic Mode Functions
IMP	Internal Model Principle
LQR	Linear Quadratic Regulator
PSD	Power Spectral Density
RMS	Root Mean Square
RSW	Resistance Spot Welding
SCR	Silicon-Controlled-Rectifier
STFT	Short-Time Fourier Transform
TFR	Time-Frequency Representations
TITO	Two-Input-Two-Output

Chapter 1

Introduction

1.1 Motivation

Since the internal model (IM) based adaptive algorithm for periodic disturbance cancellation with uncertain frequency was proposed by Brown and Zhang in [1], it has been successfully employed on several applications, such as musical pitch tracking [2], power systems [3], and sound and vibration control [4], etc.. The results of these applications have proven that the algorithm is powerful in instantaneous frequency (IF) estimation, signal identification and noise cancellation when the input is composed of narrow band signals.

The research of this thesis was motivated by two of the applications - one is an acoustic duct system studied by Brown and Lu in [4]; the other is a resistance spot welding (RSW) process investigated by Malhotra in [5]. Modifications to this basic algorithm were appropriately made attempting to meet other requirements in addition to IF estimation and/or noise cancellation, i.e., stability in acoustic duct system and dynamic resistance measurement in RSW.

In [4], the algorithm was applied to an acoustic duct and excellent disturbance rejection was achieved. However, the system is stable only when the disturbance frequency

varies in a very narrow band of frequency. The problem can be intuitively explained as follows: on one hand, the system has large phase variation (exceeding 180°) over the range of the frequencies of interest; on the other hand, the control gains of the IM are fixed. Stability for the basic algorithm can be guaranteed as long as control gains can be selected that stabilize the system in the nonadaptive case. With fixed gains, stability can only be achievable when the systems have frequency responses with fairly constant phase responses (changing by no more than 90°). However, this is not possible for systems that have significant phase variations like the system of an acoustic duct, where possible positive feedback would be caused when the change of the phase is greater than 180° over certain frequency ranges. New insights into the algorithm need to be gained in order to improve the stability of the system. By adaptively tuning the control gains, letting them rotate with the frequency such that the phase of the system at resonance remains constant as possible, it may be hoped to get better stability performance over a wide range of frequency.

The two states of an IM exhibit many nice characteristics. They are sinusoidal, and orthogonal such that they can be used to form an analytic signal of the input as given in Hilbert Transform (HT) theory. This recognition triggers significant interest in signal processing, e.g., instantaneous Fourier decomposition (IFD) for an nonstationary signal composed of sums of narrow band signals. This decomposition was first applied to RSW for real time dynamic resistance estimation in secondary circuit by Malhotra [5]. The algorithm present in [5] gave fairly good decompositions of signals with a finite number of harmonics, but had poor transient response, and performed poorly with experimental weld data which is composed of an infinite number of harmonics. To decrease the transient response and to reduce the overshoot, the initial conditions of each IM are re-investigated in

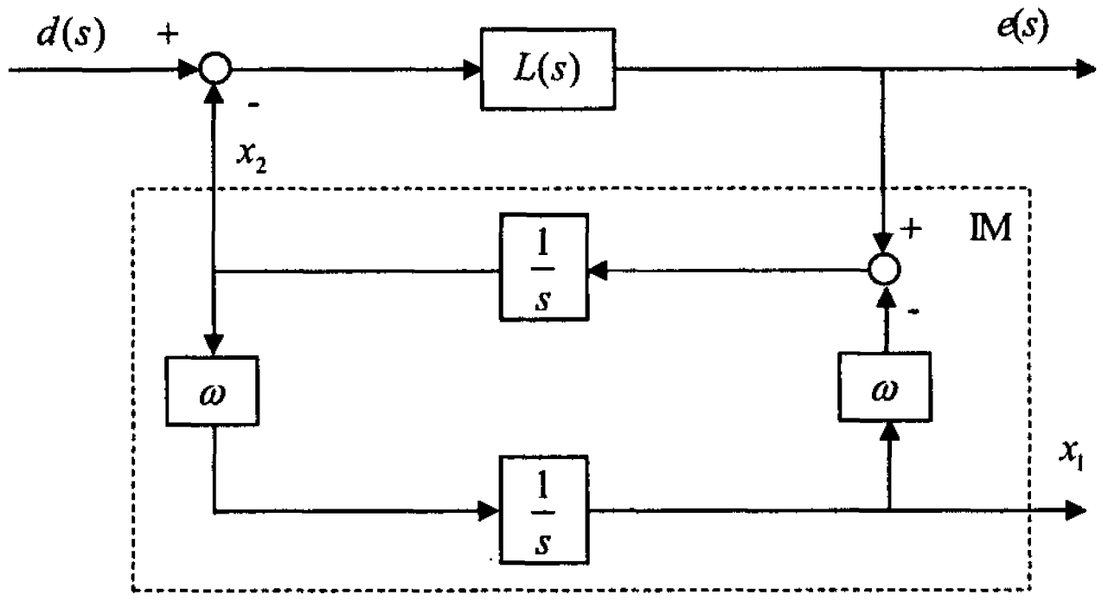

Figure 1.1: The block diagram of the basic internal model based periodic disturbance cancellation system

this thesis, the tuning of the estimation system is re-developed, so that tracking performance is improved and the estimation is more accurate.

1.2 Review of the Basic Algorithm

The foundation of this thesis utilizes an internal model based adaptive algorithm to improve the stability of the acoustic duct system and to measure the dynamic resistance in RSW. The modified algorithms are rooted in the works of Zhang [6] and Brown [7].

The novel algorithm was based on the internal model principle (IMP) [8]. It was originally constructed to identify and cancel a periodic disturbance with unknown frequency as present in [1, 6, 7]. The block diagram of the control system with an IM in the feedback loop is shown in Fig. 1.1, in which $L(s)$ is a fictitious plant or a tuning function. The disturbance $d = A\cos(\omega_d t + \varphi)$ is the input signal, where ω_d is the true frequency of the disturbance of interest to be identified, φ is the initial phase, e is the feedback error that serves as the input of the IM, x_1 and x_2 are the two states of the IM. x_2 is the output of the IM which is identical to the input d. The transfer function of the IM from e to x_2 is $\frac{s}{s^2+\omega^2}$,

where ω is the estimate of ω_d. The state space representation of the IM is given by

$$\begin{bmatrix} \dot{x}_1 \\ \dot{x}_2 \end{bmatrix} = \begin{bmatrix} 0 & \omega \\ -\omega & 0 \end{bmatrix} \begin{bmatrix} x_1 \\ x_2 \end{bmatrix} + \begin{bmatrix} 0 \\ 1 \end{bmatrix} e$$

$$y = \begin{bmatrix} 0 & 1 \end{bmatrix} \begin{bmatrix} x_1 \\ x_2 \end{bmatrix} \tag{1.1}$$

Based on the IMP, in steady state, we have

$$x_1(t) = A\sin(\omega_d t + \phi) \tag{1.2}$$

$$x_2(t) = A\cos(\omega_d t + \phi) \tag{1.3}$$

$$e(t) = A_e \sin(\omega_d t + \phi) \tag{1.4}$$

where $A = \frac{A_e}{\omega^2 - \omega_d^2}$, and ϕ denotes the phase of e. The difference $\Delta\omega$ between the estimate ω and the true frequency ω_d can be expressed by a non-linear function

$$\Delta\omega = \omega - \omega_d \approx \frac{ex_1}{x_1^2 + x_2^2}$$

A simple integrator can be used to update the frequency estimate ω and thus drive the difference $\Delta\omega$ to zero, i.e.

$$\frac{d\omega}{dt} = K_e \Delta\omega \approx K_e \frac{ex_1}{x_1^2 + x_2^2 + \varepsilon} \tag{1.5}$$

where K_e is the adaptation gain, ε is a very small constant to ensure no division by zero problem. By this means, frequency, and magnitude of the disturbance can be obtained. The stability and convergence of the adaptive algorithm are proven in [6, 7].

1.3 Review of Literature

The contents of this thesis build on a large volume of literature covering signal decomposition in signal processing and resistance measurement in RSW in control field. Prior to describing the contributions of this thesis, the relevant literature will be first reviewed in this section.

1.3.1 Literature Review on Signal Decomposition

Signal decomposition is a common theme in signal processing. The field of signal processing is mature, yet active [9]. The techniques of signal analysis and synthesis are various. From filtering to transforms, from subband decomposition to time-frequency representations (TFR), the details of the methods can be easily found in many published books [9, 10, 11].

Fourier Series Fourier series is a classical frequency representation that has been a key technique for signal decomposition and reconstruction [12]. The theory of Fourier series says that any periodic signal can be formed by a sum of weighted sinusoids with frequencies are integer multiples of the reciprocal of the period. This is extended to more general signals through Fourier transform (FT) analysis and to a time-frequency analysis by using windows of data. During recent years, Fourier analysis has been supplemented by

other approaches, most notably are orthogonal transforms, subbands and wavelets. These alternatives hold promise for providing more useful ways of analyzing and processing signals for different applications, but Fourier series is still the prime vehicle for a large class of signal processes, and provides a useful theoretical tool for evaluating the new methods.

However, the majority of signals encountered in the real world are nonstationary, that is, the salient features of the signals change with time [9]. For such signals, the standard Fourier analysis is inadequate in highlighting local features of a signal due to its performance limitations [13]. The most prominent limitations are: 1) frequency resolution, i.e., the ability to distinguish the spectral responses of two or more signals; 2) leakage in the spectral domain due to evenly windowing of the data. These performance limitations are particularly troublesome when analyzing short data records and nonstationary signals.

To overcome the limitations of the standard Fourier analysis, Gabor resorted to the windowed, short-time Fourier transform (STFT)[9]. It is suitable for locally stationary but globally nonstationary signals, but it still has the frequency resolution problem due to the fixed-duration widow inheriting from the classical Fourier transform. Though an adaptive short-time Fourier transform (ASTFT) [14] can outperform conventional STFT, it is at the expense of higher computational and storage cost.

Wavelet Transform The wavelet transform [15, 16, 17, 18] is a mathematical tool that decomposes a signal into linear combinations of local, time-dilated and time-translated wavelet components. A wavelet is a small wave (oscillatory) whose amplitude quickly decays to zero in both the positive and negative directions. The main advantages of wavelet transform over traditional Fourier series are the use of localized basis functions and the faster computation speed. The wavelet transform is similar to the STFT in that the signal

is multiplied by a function similar to windows function in STFT, but the transform is done separately for different segments of the signal. The main differences between the wavelet transform and the STFT are that in wavelet transform, the width of the window is changed as the transform is computed for every single spectral component [19]. Though wavelet transform is suitable for a variety of systems, it is typically well-suited for approximating data with sharp discontinuities. The difficulty of using wavelet transform is choosing or designing the appropriate mother wavelet for a given application.

Hilbert-Huang Transform Hilbert-Huang Transform (HHT) is a novel analysis method for nonstationary data, which was developed by Huang *et al* in 1998 [20]. The key part of HHT is the empirical mode decomposition (EMD), with which any complicated dataset can be adaptively decomposed into finite and often smaller number of monocomponent signals, defined as intrinsic mode functions (IMFs). With the Hilbert transform (HT), the IMFs form a time-frequency-energy representation of the data, and yield instantaneous frequencies as functions of time as well. Since the decomposition is based on the local characteristic time scale of the data, it is believed by many researchers [21, 22] that HHT is applicable to any time-varying process. When stationary datasets are used, HHT provides the same solution as the STFT. For analyzing nonstationary signals or data, HHT offers much better temporal and frequency resolutions. However, the signal analysis based on Hilbert transform is physically significant only on narrow band signals. The intrinsic mode functions have been conjectured to be narrow band if the signals are composed of the sum of narrow band signals.

1.3.2 Literature Review on Resistance Measurement in RSW

Resistance spot welding (RSW) is widely used for joining sheets because of its short duration time, low cost operation, and adaptability for automation in high volume production. However, due to the complexity of the basic process as well as from numerous sources of variation, RSW suffers from a major quality variation problem, i.e., inconsistent quality from weld to weld [23]. Though RSW has been continually studied since its invention [24], there is currently no satisfactory nondestructive quality evaluation for this type of welding.

The key to ensure weld quality through online measurement and process control is to choose the right control variables. There are many process variables involved in RSW as discussed by Malhotra in [5]. Some of them are extremely difficult to control and may cause weld problems, others are easy to control, such as the current and time. Electrical or mechanical variables, such as primary dynamic resistance [25, 26], secondary dynamic resistance [5, 27], welding current [28, 29], electrode displacement [30, 31], and electrode wear [32], have been often used as the monitoring parameters. The weld nugget has also been examined in [33, 34, 35].

As the name of RSW implies, electrical resistance is the most important factor affecting resistance spot welding [36]. It has physical meaning relating to the variation of the heating, the growth of the nugget diameter, and the penetration of the electrodes, etc.. For this reason, many researchers have employed resistance as a valuable input parameter for a monitoring of the process to obtain good weld quality. Brown *et al* [33] developed a neural network model to provide information about the nugget diameter and heat being generated at the weld using the entire dynamic resistance curve as one of the inputs. Lee *et*

al [24] selected the dynamic resistance as the indicator of expulsion during welding using a neuro-fuzzy algorithm. Hao *et al* [37] used the dynamic resistance, in addition tip voltage, to improve the detection of the online nugget expulsion. Li *et al* [35] used the dynamic resistance as the only input variable for their neural network model to estimate online nugget size. Livshits [38] proposed a universal quality assurance method based on dynamic resistance that is valid over a wide range of welding time, welding current, electrode force and electrode tip geometry.

The electrical resistance cannot be considered as a constant during resistance spot welding [39]. A determination of dynamic resistance is beneficial for monitoring the weld quality. Generally speaking, the resistance can be calculated by dividing the voltage by the current. However, due to the inductive noise in the measured voltage signal, the measured tip voltage cannot be directly used for calculating the resistance. In literature, a lot of work has been done attempting to obtain the accurate measurement of the tip voltage and dynamic resistance. Osman *et al* [40] discussed a peak value method in which the tip voltage is measured only when current derivative is zero at the peak. Hence, the induced voltage is zero. Cho *et al* presented a new technology to measure the dynamic resistance in [25, 26]. However, the base line of the approach is the same as the Osman's peak value method. The dynamic resistance is obtained once per half cycle. The only difference is that they measured primary dynamic resistance instead of measuring it on the secondary loop. The advantage of the peak value technique is that it can effectively eliminate the induced noise from the voltage signal, but the drawback is that the measurement is discontinuous since the voltage and current are available only once per half cycle. In order to obtain the continuous measurement of the resistance, Hao *et al* proposed a data acquisition and signal

processing system for spot welding aluminium in [41], where a scaled measurement of the derivative of the current was subtracted from the measured tip voltage signal. However, the compensated voltage by the extra loop cannot be guaranteed to be the same as the induced voltage, an accurate calibration of the scaling. It may change as soon as the area encompassed by the voltage measuring leads changes. A recursive least square technique with a forgetting factor for time varying resistance measurement and mutual inductance estimation is proposed by Garza *et al* in [42]. The tip voltage was calculated by subtracting a scaled version of $\frac{dI}{dt}$ from the measured tip voltage. The scaling constant was determined online by autoregressive moving-average (ARMA) model. By this means, the time varying dynamic resistance can be obtained. However, the estimate of the resistance in that work indicates very rapid changes with time which seems very unrealistic. This could be attributed to the highly variable values of the scaling constant that they estimated. More recently, a fuzzy adaptive algorithm [43] and a neuro-fuzzy algorithm [24] are proposed in literature to estimate the dynamic resistance. However, too many input variables and fuzzy rules are required to identify the time varying dynamic resistance.

1.4 Major Contributions in This Thesis

In this thesis, after further investigation of the aforementioned internal model based adaptive algorithm, new insights are gained, appropriate modifications are made, and successful implementations are completed to employ it on two practical applications: an acoustic duct system to improve stability performance, and RSW process to estimate the dynamic resistance.

1.4.1 An Application to an Acoustic Duct System for Stability Improvement

1) A modified transfer function in the adaptive form $\frac{K_2(\omega)s^2+K_1(\omega)s}{s^2+\omega^2}$ is presented.

2) The design method how to choose K_1 and K_2 such that K_1 and K_2 can rotate with the IF ω is given.

3) The improvement of the stability performance of the modified algorithm is achieved in that the stable frequency band for a widely phase varying system is significantly increased.

4) Simulations on an acoustic duct verify the algorithm on both independent pure sinusoidal signals and a chirp signal corrupted with Gaussian white noise.

1.4.2 An Application to RSW Process for Dynamic Resistance and Tip Voltage Estimation

1) A modified output state space representation in the form of $y_i = \begin{bmatrix} K_{1i} & K_{2i} \end{bmatrix} \begin{bmatrix} x_{1i} \\ x_{2i} \end{bmatrix}$ is presented.

2) The design method how to choose K_{1i} and K_{2i} to achieve a bandpass filter with notches is given.

3) A new application on RSW process to estimate the online values of the tip voltage (with no loop area calibrations) and dynamic resistance is implemented. A tip voltage and dynamic resistance measurement system is investigated and developed.

4) A model of a simple exponential decay is incorporated to improve transient performance.

4) Multiple IMs are used to cancel harmonics present in the input signals.

5) Information such as an expulsion can be provided by the estimate of the dynamic resistance.

6) Simulations verify the algorithm on synthesized data.

7) Application on real data gives very reasonable results.

1.5 Outline of the Thesis

The organization of the thesis is as follows. In Chapter 2, the work on tuning to stabilize adaptive internal model controller for periodic disturbance cancellation on an acoustic duct is presented. In Chapter 3, the novel algorithm of instantaneous Fourier decomposition is proposed. By connecting multiple internal models in parallel in the feedback loop, an real time Fourier series representation for a signal composed of harmonics can be achieved. The application of the modified algorithm to RSW process for tip voltage magnitude and dynamic resistance estimation is addressed in Chapter 4. Conclusions and future work are given in Chapter 5.

Chapter 2

Modifications and Design to Stabilize Adaptive Internal Model Controller for Periodic Disturbance Cancellation [1]

2.1 Introduction

Acoustic noise cancellation is an interesting and challenging problem in the area of sound and vibration control due to computational complexity and uncertainties of acoustic systems. A major source of destructive noise is periodic acoustic noise, which is generated in a wide range of active and dynamic systems including systems with AC power, electric fans and air blowers, etc. [44]. Often the noise is contained in ducting where it is possible to create opposing sounds that eliminate the noise. An introduction to this topic and summary of the relevant active control techniques are given by Fuller and Flutow in [45]. One of the challenges of this application is that the systems to be controlled typically exhibit dead-time or transport delays leading to large and rapidly varying phase lags.

---

1. The content of this chapter is truncated from a paper submitted for review.
Lyndon Brown and Yujuan Sun, "Tuning to Stabilize Adaptive Internal Model Controller for Periodic Disturbance Cancellation", *Proc. 45th IEEE Conference on Decision and Control.*

There are many methods specifically applicable to perform periodic disturbance cancellation. One of the well-known methods is the internal model principle (IMP) approach, proposed by Francis and Wonham [8] in 1976. For perfect disturbance rejection, a suitably reduplicated model of the exosystem generating the disturbance has to be included in the stable closed-loop system. This is a simple extension of integral control to non-constant disturbances. As with integral control, a minimum requirement for stability is that the phase angle of the controller, at the frequency where the controller gain is infinite, has the opposite orientation as that of the plant, resulting in negative feedback. If this condition is not satisfied, positive feedback and instability result.

Furthermore, it is not always the case that the disturbance model is completely known or that the disturbance properties are constant over time [46]. To overcome the limitation of the IMP approach, an adaptive version of the internal model controller (IMC) was constructed in [1, 7] to cancel periodic disturbances with unknown frequency. The application of the IMC on a model of an acoustic duct presented in [4] shows that this internal model based adaptive control algorithm can achieve perfect disturbance rejection within a reasonable narrow band of frequency. For a fixed-gain, adaptive-frequency IMC, stability can only be achieved over ranges of frequency when the plants have frequency responses with fairly constant phase responses (changing by no more than 90°). Unfortunately, it is seldom the case that this holds true over all frequencies.

To keep the system stable over a large range of frequency, a new alternative form $\frac{K_2(\omega)s^2+K_1(\omega)s}{s^2+\omega^2}$ for the transfer function of the IMC is adopted. The two control gains, K_1 and K_2, are functions of ω, chosen so that the phase margin resulting from the critically stable poles is fixed. This ensures that the system has negative feedback everywhere in the

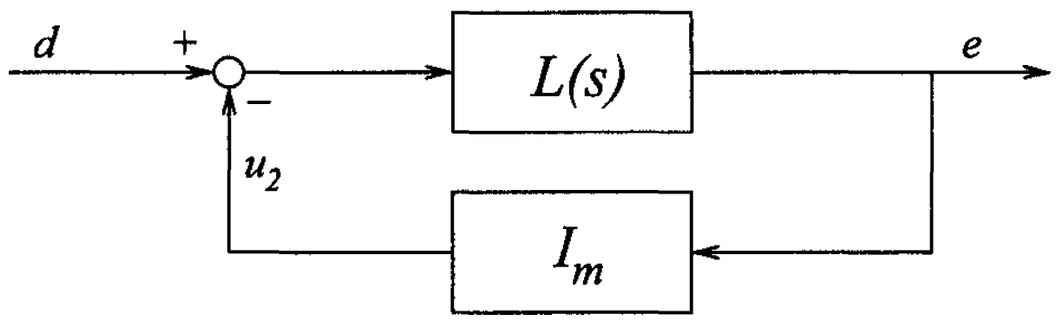

Figure 2.1: The general block diagram of an internal model control system

desired frequency range. Thus the stable frequency band can be significantly broadened for an acoustic system which previously was stable only for a very narrow band of disturbance frequency.

2.2 Improved Internal Model Based Adaptive Algorithm

The block diagram of the original internal model based adaptive algorithm described in section 1.2 is simplified as Fig. 2.1, in which, I_m stands for an adaptive IMC which is used to identify d, and then to cancel it. u_2 is the output signal of the IMC, which, in steady state, has the exact frequency, magnitude and phase of the disturbance d that can cancel the disturbance perfectly. The system $L(s)$ is assumed to be a well behaved plant or properly designed feedback system. For this reason, while we would like our closed loop transfer function $\frac{L(s)}{1+L(s)\cdot I_m}$ to be zero at the disturbance frequency, we would like it to be equal to $L(s)$ elsewhere.

When the disturbance d is a pure sinusoid, $d(t) = a\sin(\omega_d t + \varphi)$, where ω_d is the true frequency of the disturbance, and φ is the initial phase. The transfer function of I_m, in the form of

$$I_m(s) = \frac{s}{s^2 + \omega^2} \tag{2.1}$$

where ω is the estimate of ω_d from the IMC, was used in [4] to cancel the disturbance. The single zero at the origin causes the frequency response of IMC to be very small for both large and small frequencies satisfying our design goal of minimally affecting the behavior of our system.

The basic form of I_m described above was proven to be exponentially stable [7] under the assumptions that the adaption gain K_e in (1.5) is chosen sufficiently small, and the phase of $L(j\omega)$ remains between $-90°$ and $+90°$ for all ω that are encountered. The difficulty is that for many noise cancellation applications, the latter assumption restricts ω to a narrow range. This can be interpreted by considering the Nyquist plot of (2.1). The plot is a simple half circle which encircles the entire right half plane. Thus the Nyquist plot of the loop transfer function will form a half circle at infinity that will contain the negative real axis if $L(s)$ has angle between -90° and -270°. When the Nyquist plot of the open-loop system encircles the negative real axis at infinity, it is likely to include $(-1, j0)$ point implying an unstable nominal system.

Since most adaptive noise cancellation problems have significant transport delays resulting in large changes in their phase responses, the nominal system is likely to be unstable for some values of ω and thus unstable for all but certain values of ω_d. This has been verified by an application of an acoustic system in [4]. The model of the acoustic system includes resonant peaks which dominate the dynamics [47] and transport delays. Generally, the precise locations of the resonances have significant uncertainty. Fig. 2.2 shows a typical Bode diagram of a finite degree state space model of an acoustic duct [48] with a linear quadratic regulator (LQR) in a feedback loop. From Fig. 2.2, it is obviously seen that the system has a constant gain/phase at very low frequencies, but they change rapidly

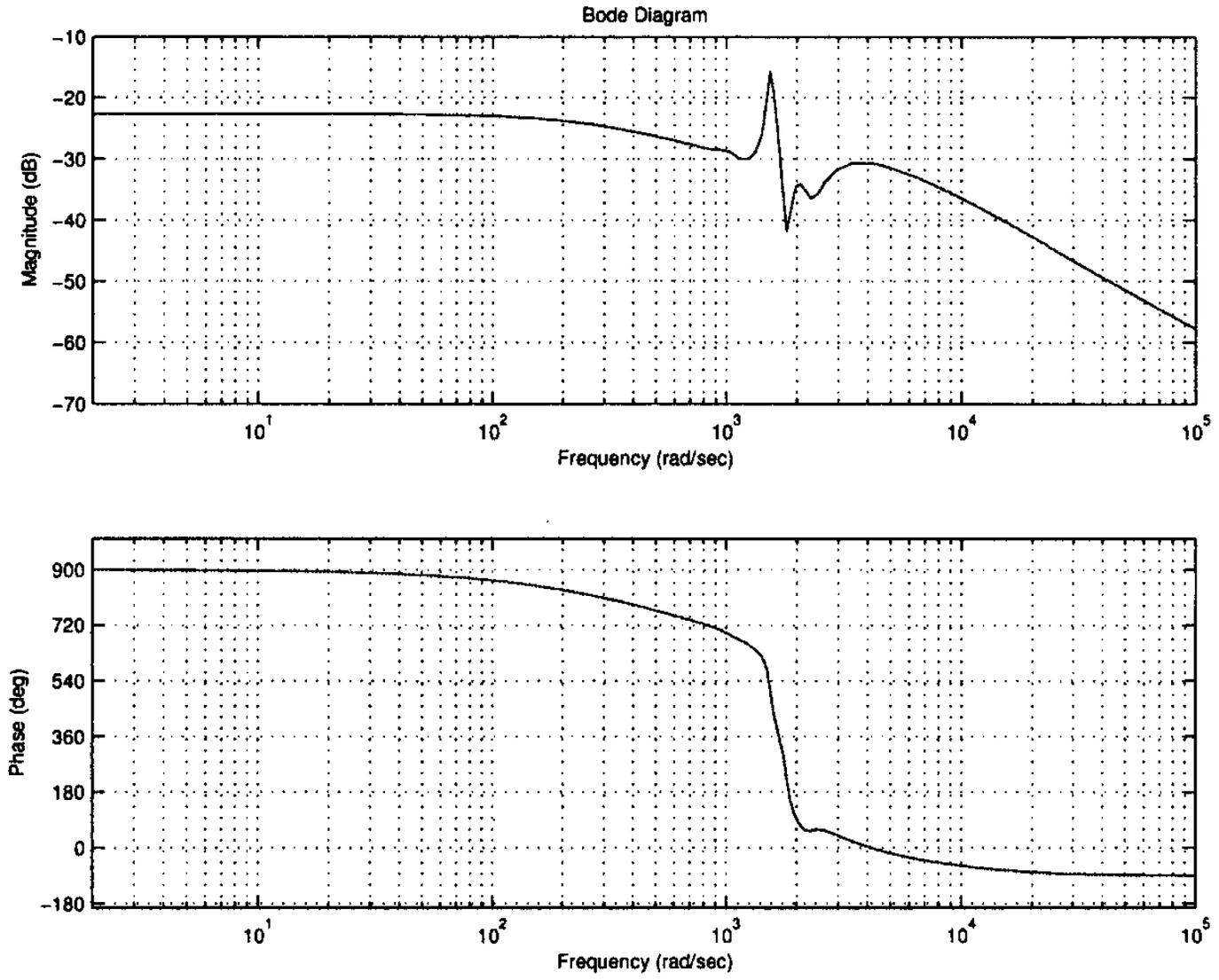

Figure 2.2: The Bode plot of $L(j\omega)$

at high resonant frequencies.

As discussed earlier, it is assumed that $L(s)$ has been designed to have satisfactory behaviour at all frequencies except ω_d. Thus, ideally we would like I_m to be small outside some region about ω_d as in the aforementioned form. Unfortunately, the simplest modifications, either adding a PD or PI controller in series with I_m, result in a transfer function that is non-small either above or below ω. In general, $L(s)$ will have a low pass nature, hence it will be small for large frequencies, mitigating the need for I_m to be small here. In addition, if I_m is non-small at low frequencies, its sign will need to be fixed, reducing our tuning flexibility. For these reasons, we will add an adaptive PD controller in series with the original I_m or equivalently add a zero to the basic transfer function. The modified transfer function is thus $\frac{(K_2(\omega)s+K_1(\omega))s}{s^2+\omega^2}$, where K_1 and K_2 rotate with the instantaneous frequency ω estimated by the improved algorithm. The corresponding Nyquist plot near ω

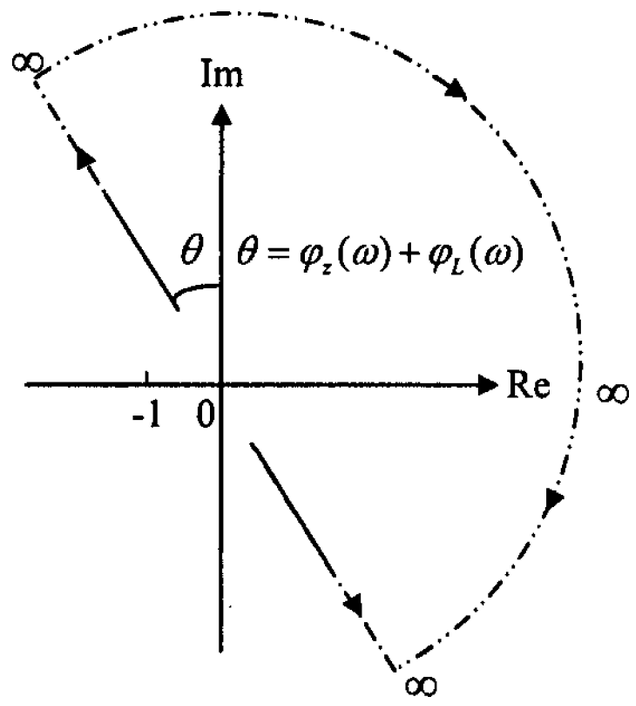

Figure 2.3: The sketched Nyquist plot of the open-loop system with the modified IMC, $\frac{(K_2(\omega)s+K_1(\omega))s}{s^2+\omega^2}$, in range of $[\omega-\varepsilon, \omega+\varepsilon]$, where ε is a small constant

for the open-loop system with the modified transfer function of the IMC is shown in Fig. 2.3, in which, $\theta = \varphi_z(\omega) + \varphi_L(\omega)$, where $\varphi_L(\omega)$ is the instantaneous phase angle of the plant $L(s)$, $\varphi_z(\omega)$ is the phase of the zero term $K_2(\omega)s + K_1(\omega)$ in the modified transfer function of IMC, which is given by

$$\varphi_z(\omega) = \tan^{-1}(\frac{\omega K_2(\omega)}{K_1(\omega)})$$

For the application present in this chapter, the zero location is selected by choosing $\theta = 0$, or $\varphi_z(\omega) = -\varphi_L(\omega)$, though it is not clear that another choice, such as adding phase lead by further rotating the half circle counterclockwise, might produce better results. Thus K_1 and K_2 are given by

$$K_2(\omega) = K(\omega)\sin(-\varphi_L(\omega)) \tag{2.2}$$

$$K_1(\omega) = \omega K(\omega)\cos(-\varphi_L(\omega)) \tag{2.3}$$

This leaves a free gain parameter, $K(\omega)$, to be chosen such that the overall system remains stable. This value will need to be chosen such that, for all other points where the loop transfer function has angle close to $180°$, the loop transfer function magnitude is sufficiently less than one. Note, for noise cancellation problems, $L(s)$ is desired to be small wherever feasible. Thus $K(\omega)$ will need to be chosen small when the phase of $L(s)$ is less than $-45°$ or when the magnitude is large as a result of resonances. The proper selections of this scaling factor $K(\omega)$ and the combined phase θ guarantee the Nyquist plot does not encircle the critical point $(-1, j0)$. The system can thus be stable for all ω.

2.3 Application and Simulations to an Acoustic Duct Model

To demonstrate the effectiveness of the improved algorithm, an acoustic duct model given by Ben Amara in [48] has been investigated. The acoustic duct model shown in Fig. 2.4 is a two-input two-output (TITO) system. The two inputs are the noise d, and the voltage u applied to the noise cancellation speaker. The two outputs are the sound y measured at a microphone near the noise source, and the measured error e at the end of the duct where the noise is to be eliminated.

The block diagram of the closed-loop system with n internal models in the original form in parallel is shown in Fig. 2.5 [4]. For a single sinusoidal disturbance, Fig. 2.5 can be simplified to Fig. 2.6. The plant G is given by a discrete time state space representation (A,B,C,D) in [48], with a sampling period $T_S = 0.5\ msec$. The disturbance d adopted

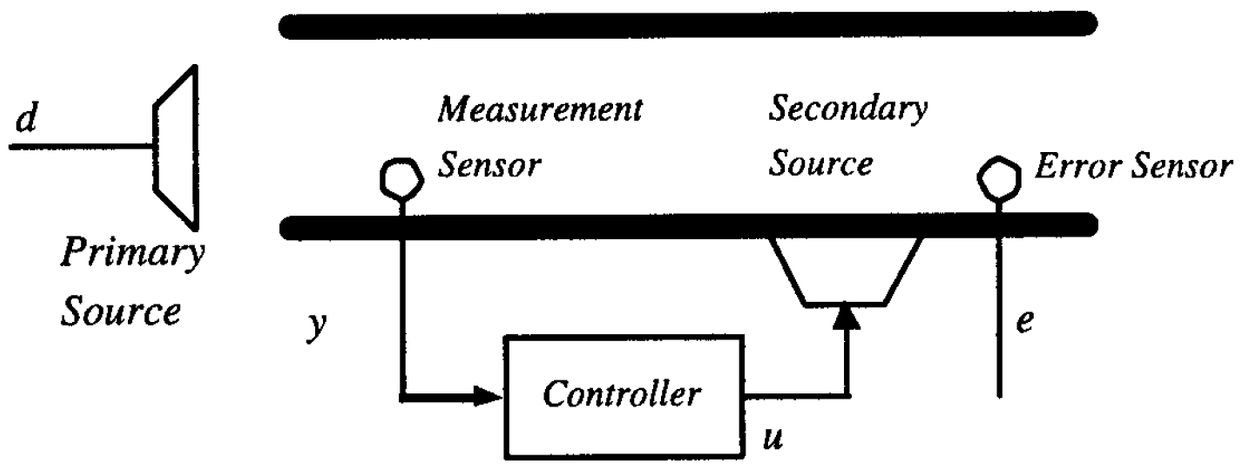

Figure 2.4: An acoustic duct model

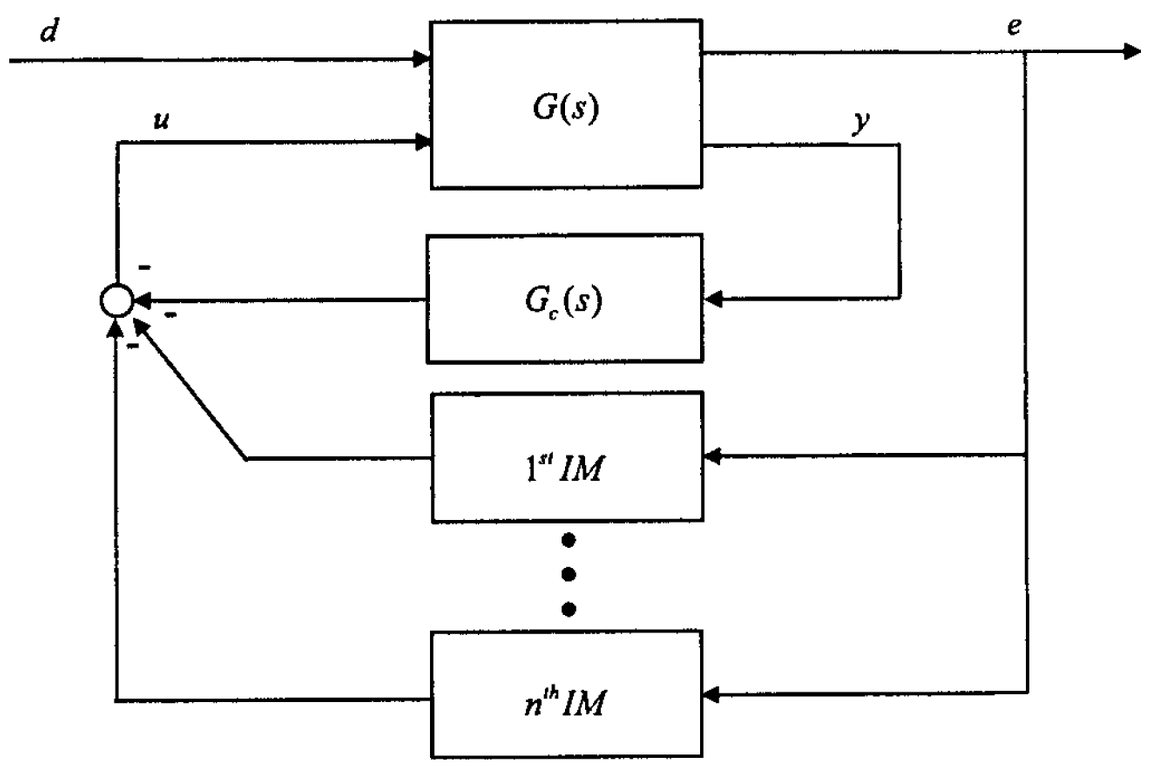

Figure 2.5: The block diagram of a control system with multiple internal models

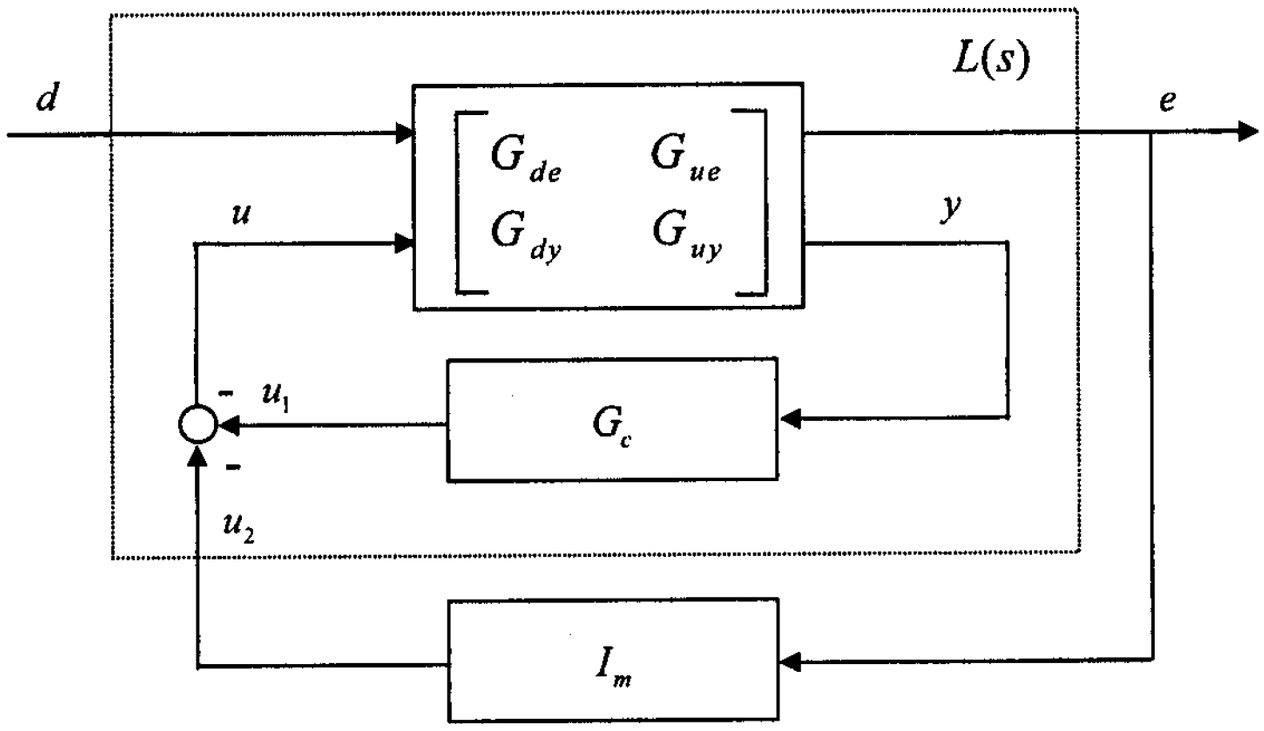

Figure 2.6: The block diagram of an internal model based acoustic duct system

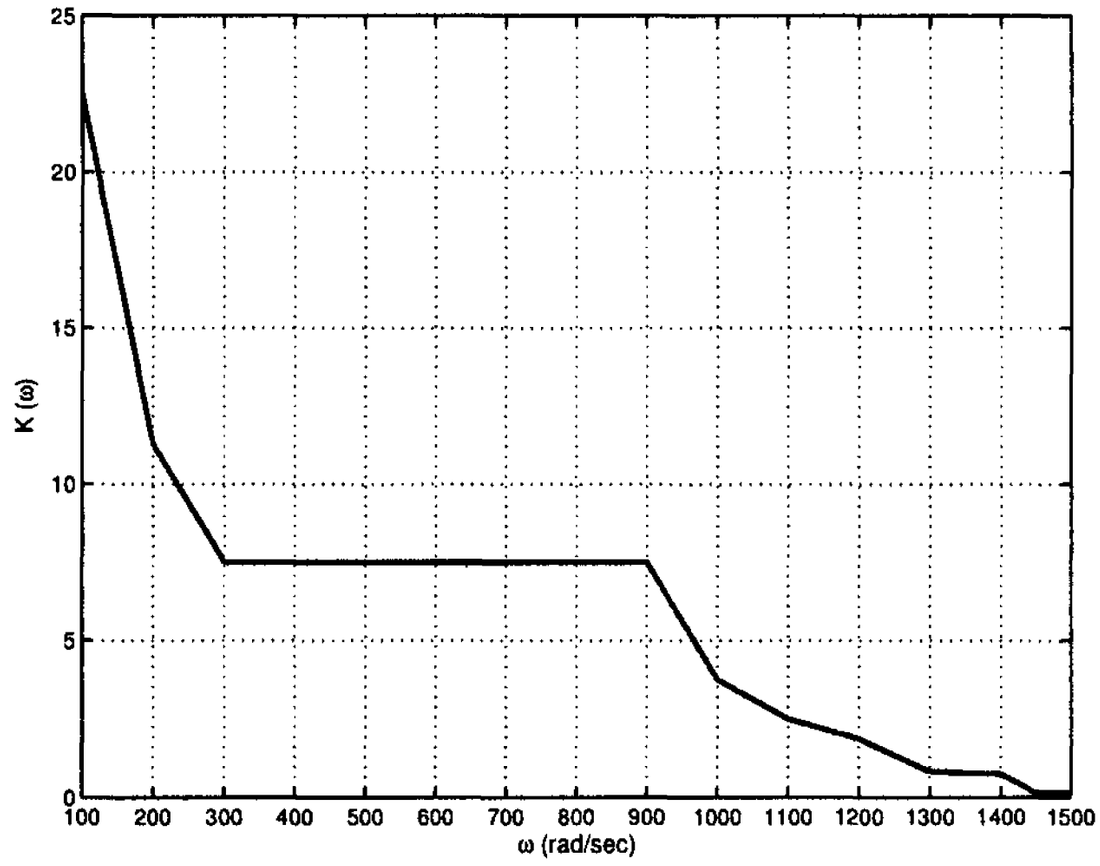

Figure 2.7: Scaling factor $K(\omega)$

by [4] is a single sinusoid with Gaussian white noise (zero-mean, PSD 0.001) added. The controller G_c is chosen as an optimal linear quadratic regulator. All the specified parameters can be found in [4] and [48] . The performance of the original disturbance cancellation is shown by Figure 3 in [4]. However, as the authors mentioned in [4], the closed-loop system could remain stable only over a narrow range of disturbance frequencies for fixed control gains. In particular, when $K_e = 0.015$, the system with I_m in the form of $\frac{s}{s^2+\omega^2}$ failed for frequencies just outside the range of [1040, 1280] rad/sec.

The improved internal model based algorithm is applied to the system in order for the adaptive system in [4] to be nominally stable over a large range of frequency. In this particular case, the overall transfer function of the plant is represented by $L(s) = \frac{G_{ue}}{1+G_c G_{uy}}$, in continuous form by using pole-zero matched approximation. The Bode plot of $L(s)$ is shown in Fig. 2.2. To validate the improved algorithm, simulations are conducted under Mathworks SIMULINK environment with the integration algorithm ODE5 at different frequencies. The parameters are chosen as $\theta = 0$, and $K(\omega)$ shown in Fig. 2.7. Since $K(\omega)$

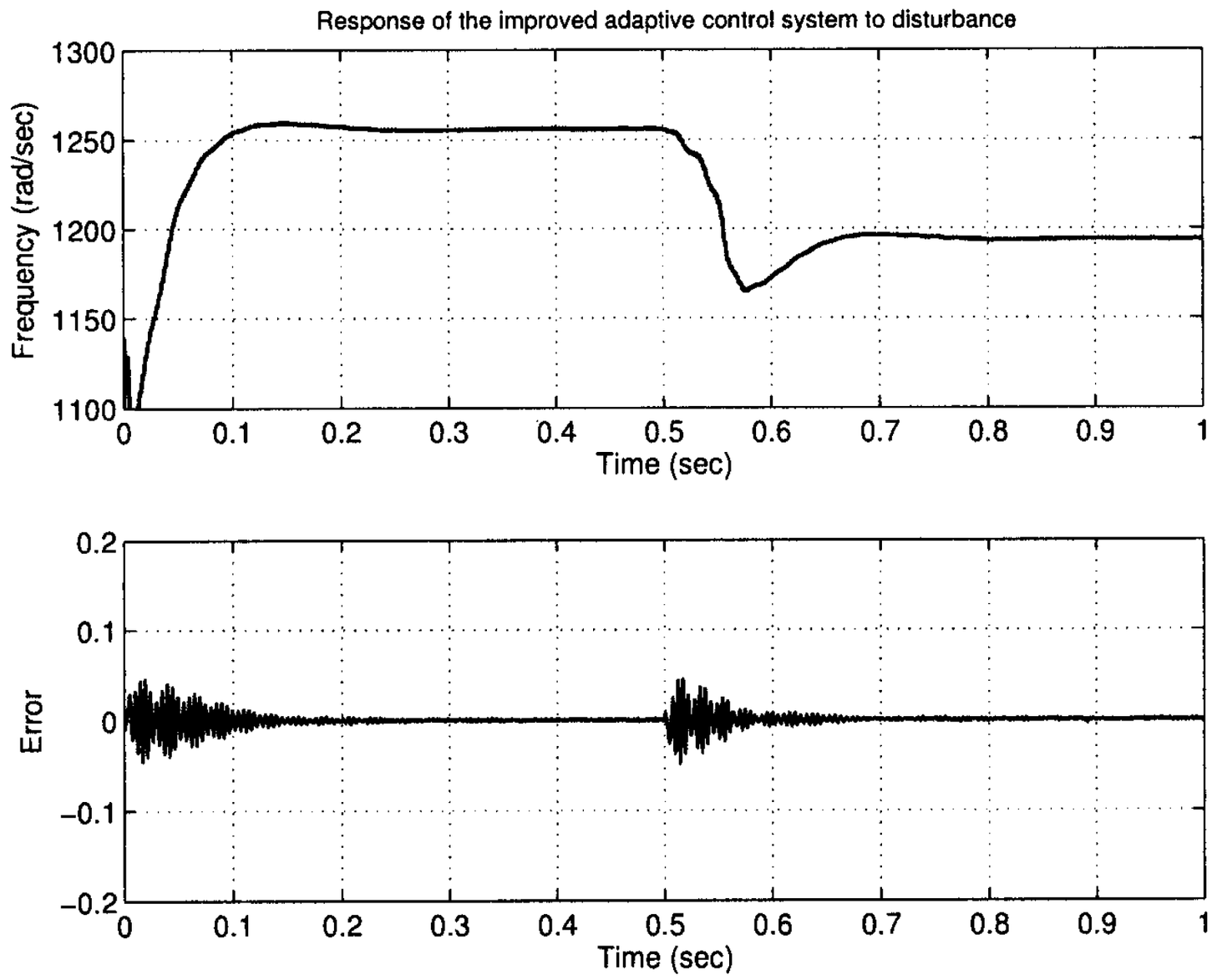

Figure 2.9: Response of the improved adaptive control system to single tone disturbance

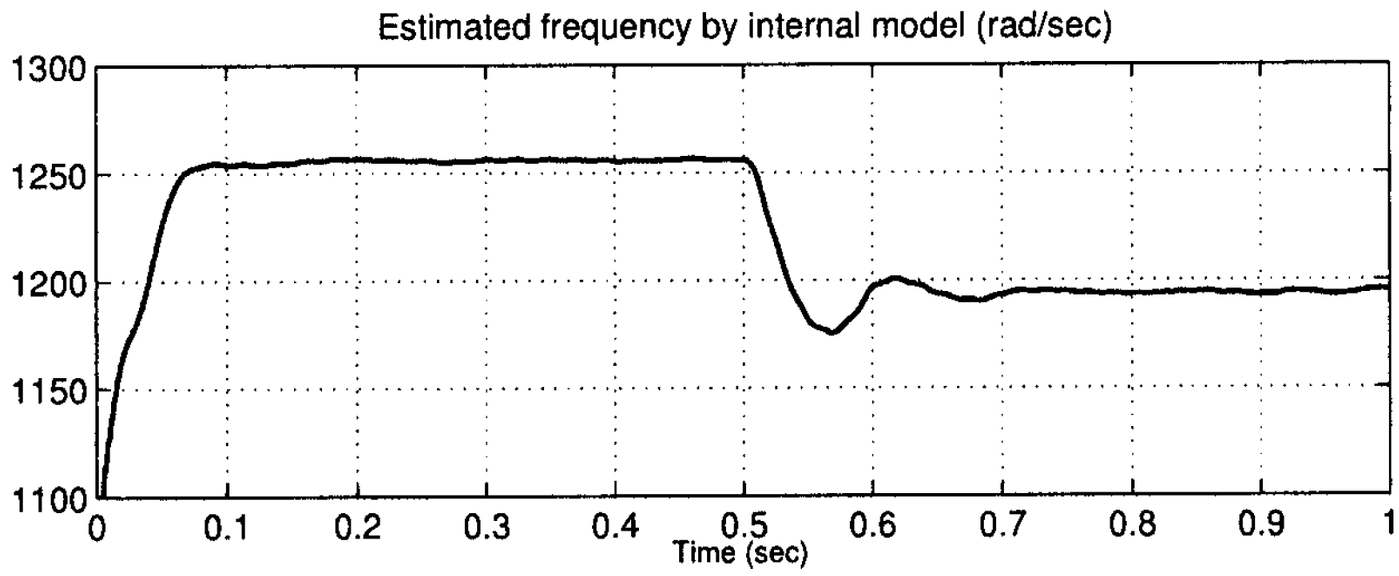

Figure 2.10: Response of the original internal model based algorithm to single tone disturbance taken from [4]

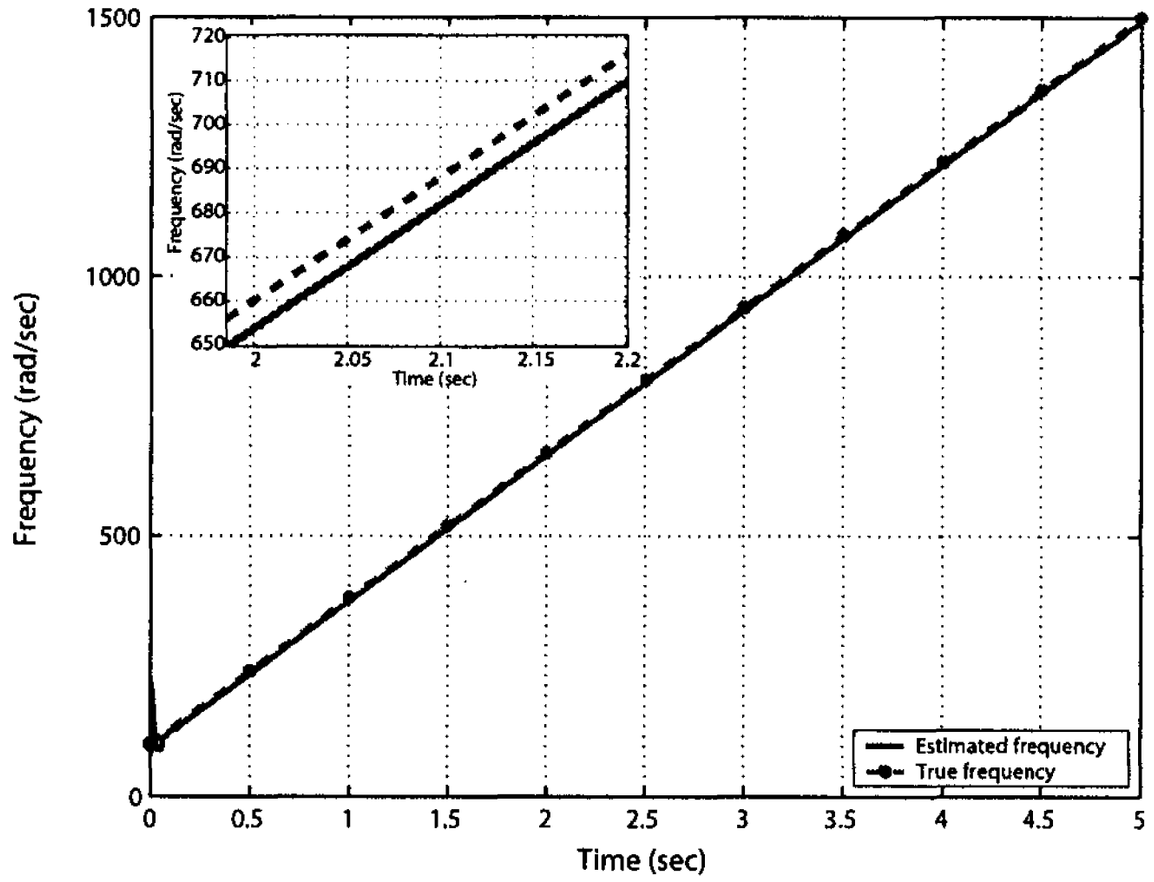

Figure 2.11: The estimated frequency of $\omega_d(t) = (100 + 280t) rad/sec$ with noise

is (1, 1256 rad/sec, 3 rad) for $0 \leq t \leq 0.5$ sec and then changes to (0.5, 1194 rad/sec, 1.5 rad) for $t > 0.5$ sec. n is a Gaussian white noise with zero-mean and PSD 0.001. The corresponding transient response is shown in Fig. 2.9. The response to the same disturbance for the original internal model based algorithm is shown by Fig. 2.10 taken from [4]. It can be seen that the proposed improved algorithm decreases the worst case error a small amount with minimum loss of speed. Thus, a major improvement in stability is achieved with no loss of performance.

To guarantee the system is stable for the entire frequency band, a chirp signal $\omega_d(t) = (100 + 280t)$ rad/sec with Gaussian white noise (zero-mean, PSD 0.001) was applied as an input test signal. The value of K_e is chosen as 0.025. The simulation result of the estimated frequency is shown in Fig. 2.11. The small embedded figure on the left corner is a partially magnified plot. The result in Fig. 2.11 shows that the estimated frequency tracks the true time varying frequency with delay about 7 rad/sec, which is equivalent to 25 $msec$ of time delay.

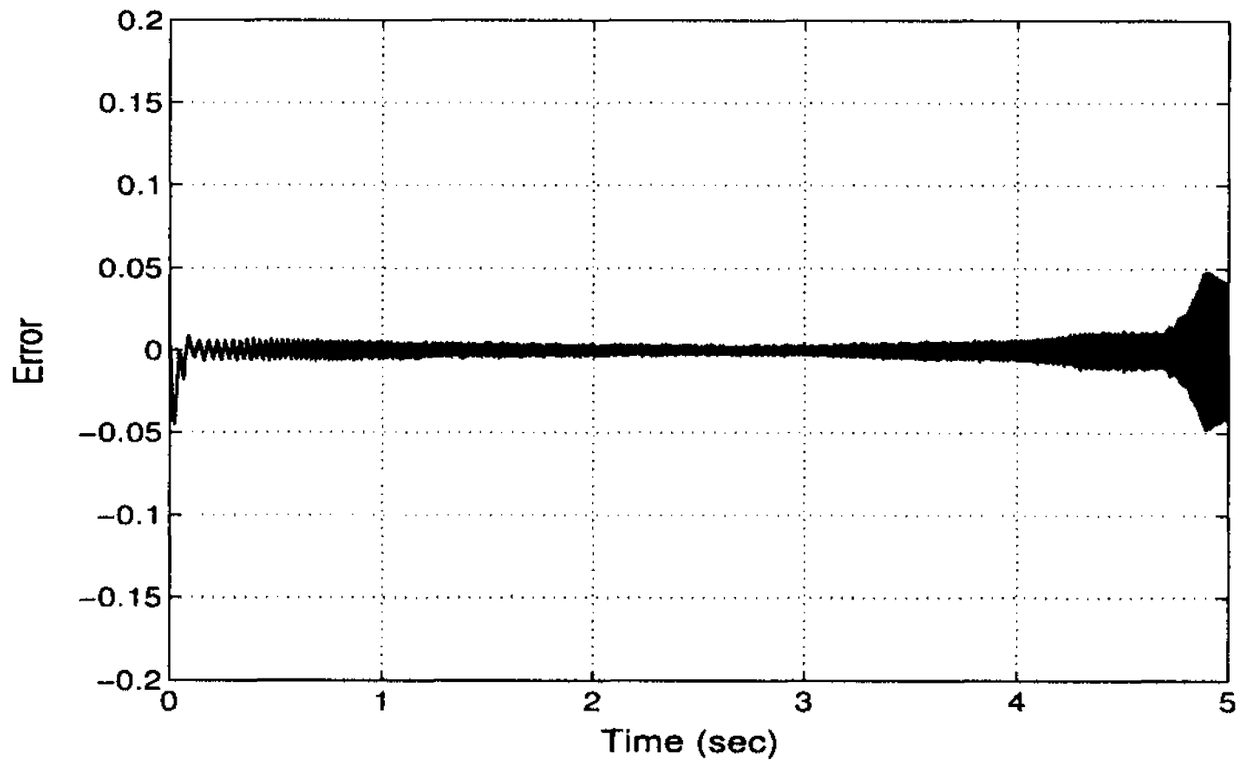

Figure 2.12: Error response of the improved adaptive control system to chirp signal (magnitude 1) with noise

Fig. 2.12 shows the error response of the improved internal model based control system to chirp system (magnitude 1) with white noise added. Note that the residual error is a result of delay between ω and ω_d. For fixed ω_d, ω converges to ω_d with delay of 25 *msec* when $K_e = 0.025$. If ω_d is fixed, the error will go to zero. A double integrator for updating ω should enable the system to exactly track ramps, thus eliminating the delay, and thus also resulting in perfect cancellation of the chirp signal. The corresponding estimated frequency and error response when using a double integrator with this noise free chirp signal are shown in Fig. 2.13 and Fig. 2.14. Comparing with Fig. 2.11, Fig. 2.13 shows the delay drops from 7 rad/sec to 0.7 rad/sec when the adaptation law for updating frequency is modified from single integration to double integration. It is believed the residual error derives from lag in the closed loop system represented in Figure 1.1.

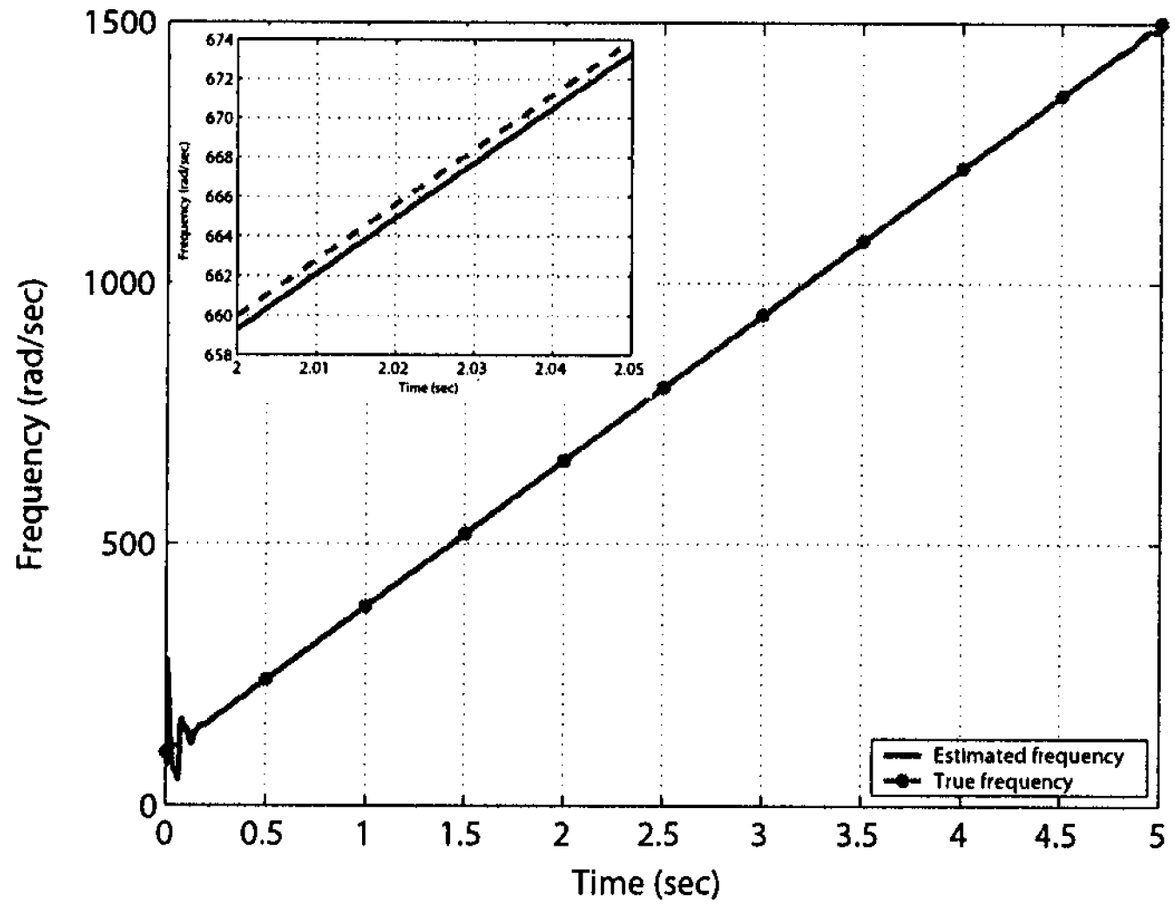

Figure 2.13: The estimated frequency to the noise free chirp signal by using double integration

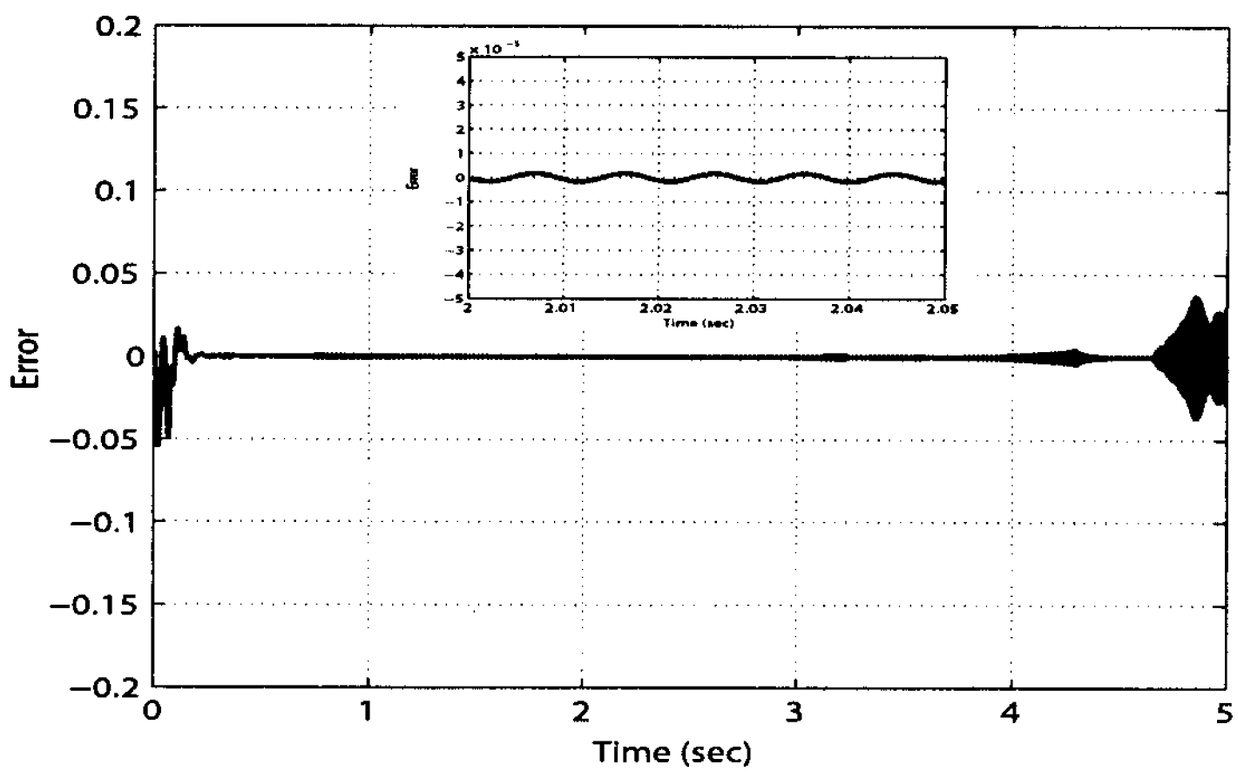

Figure 2.14: The error response to the noise free chirp signal by using double integration

2.4 Conclusions

In this chapter, an adaptive approach to improve the control capability for periodic disturbance cancellation is presented. The improved approach is based on the behavior of an adaptive internal model in an error feedback control system. The design method of the proposed improved algorithm is equivalent to placing a PD controller in series with the basic internal model in the feedback loop. The two control gains of the PD controller are made functions of the estimated frequency to keep the system as stable as possible. Simulations show that the proposed approach not only widely increases the working frequency band of the system, but also decreases the worst case error with minimum loss of speed for an acoustic system which previously was stable only for a very narrow band of disturbance frequency.

Chapter 3

Instantaneous Fourier Decomposition by Internal Model Based Adaptive Algorithm

3.1 Introduction

Signal decomposition is an important topic in pure research and practical applications in signal processing. Through signal decomposition, a complex signal or function can be decomposed into its primitive or fundamental constituents. Then simple operations can be performed separately on each component, thereby extremely sophisticated operations can be accomplished by a combination of individual simple operations [49].

Historically, the Fourier decomposition has been the prime vehicle for signal decomposition since its invention. It decomposes an arbitrary time-domain signal into complex exponentials [50], i.e., a sum of zero phase sine and cosine pairs. A Fourier transform offers a complete picture of frequency space, but for sampled data signals, it is limited in resolution, as the frequencies at which the sines and cosines are computed are equally spaced and fixed in number. Further, the signal should be strictly periodic and stationary, or be generated by a linear system.

Unfortunately, the real-world acquired data, whether from physical measurements or numerical modelling [20], most likely are from nonstationary and/or nonlinear processes. For such signals, the standard Fourier decomposition cannot give reasonable representations of the signals. Though other approaches, such as wavelet decomposition, have been studied extensively in recent years, many of them are just viewed as extensions of Fourier decomposition since the mathematical approach is very similar to Fourier analysis.

Hilbert-Huang transform (HHT), which is based on the empirical mode decomposition (EMD) method, has become one of the powerful tools to analyze nonlinear and nonstationary system data since it was introduced by Huang in 1998 [20]. The decomposition is based on the direct extraction of the energy associated with various intrinsic time scales, generating a collection of adaptive intrinsic mode functions (IMFs). Each IMF should represent a simple oscillatory mode, which is a counterpart to a simple harmonic function, but is much more general. Having obtained the IMF components, the Hilbert transform is then applied to each IMF component according to (3.1). Consequently, a set of instantaneous frequencies can be calculated, and the data can be reconstructed by an expansion in terms of the IMFs. The relevant formulae are given below [20, 21, 22].

For an arbitrary continuous signal, $x(t)$, its Hilbert transform, $y(t)$, is defined as

$$y(t) = \mathscr{H}\{x(t)\} = \frac{1}{\pi} \int_{-\infty}^{\infty} \frac{x(\tau)}{t-\tau} d\tau = x(t) * \frac{1}{\pi t} \tag{3.1}$$

where the integral is to be considered as a Cauchy principal value [51].

A complex analytic signal, $z(t)$, is formed by

$$z(t) = x(t) + iy(t) = a(t)e^{i\theta(t)} \tag{3.2}$$

where

$$a(t) = \sqrt{x^2(t) + y^2(t)}, \qquad \theta(t) = \arctan\left(\frac{y(t)}{x(t)}\right) \tag{3.3}$$

are the instantaneous amplitude and phase of $x(t)$.

The instantaneous frequency $\omega(t)$ of $x(t)$ is defined as

$$\omega(t) = \frac{d\theta(t)}{dt} \tag{3.4}$$

Since the representation of $y(t)$ is designated as the Hilbert spectrum that emphasizes the local properties of $x(t)$, and the polar coordinate expression (3.3) further clarifies the local nature of this representation, the Hilbert-Huang transform would be ideal for nonlinear and nonstationary system data analysis.

However, the Hilbert transform (3.1) is noncausal. It can not be implemented in real time [51]. Moreover, for the instantaneous frequency to make sense, Huang clearly stated in [20] that the data are restricted to be narrow band. With this restriction, the Hilbert transform (3.1) can be approximated by [52]

$$y(t) = \mathscr{H}\{x(t)\} \approx -\frac{1}{\omega}\dot{x}(t) \tag{3.5}$$

where ω is the best estimate of the instantaneous frequency. Thus, the integral operation in

(3.1) is replaced by an differential operation.

In this chapter, a new data analysis method adopted from the basic internal model based adaptive algorithm described in section 1.2 will be present. The key part of the method is instantaneous Fourier decomposition (IFD). This approach was first introduced by Malhotra in [5]. The decomposition is based on the sinusoidal and orthogonal state variables associated with internal models (IMs). In terms of the state variables, the instantaneous frequencies can be calculated, and the data can be reconstructed. Since the internal models can be adaptive in the form of sine and cosine pairs, it can be interpreted as a Fourier transform. When the frequencies are restricted to be integer multiples of each other, a Fourier series representation is generated. Thus, we can localize any event on the time as well as the frequency axis. Also, these state variables, based on and derived from the data, can serve as the basis of other operations which can be simple or sophisticated. Most importantly, this method can be implemented in real time.

3.2 Motivation of Instantaneous Fourier Decomposition

In Section 1.2, the structure of the basic internal model based adaptive algorithm was shown in Fig. 1.1. The two state variables x_1 and x_2 of the IM were proposed to be mapped into a 'measurement' of the instantaneous frequency of a pure sinusoidal signal. Unfortunately, most of the real data are not pure sinusoids. At any given time, the data may involve more than one oscillatory mode, either harmonics or multiple tones. Since any arbitrary quasi-periodic signal can be represented by a Fourier transform composed of a sum of delta functions, we can decompose the data into a sum of sine functions by employing multiple

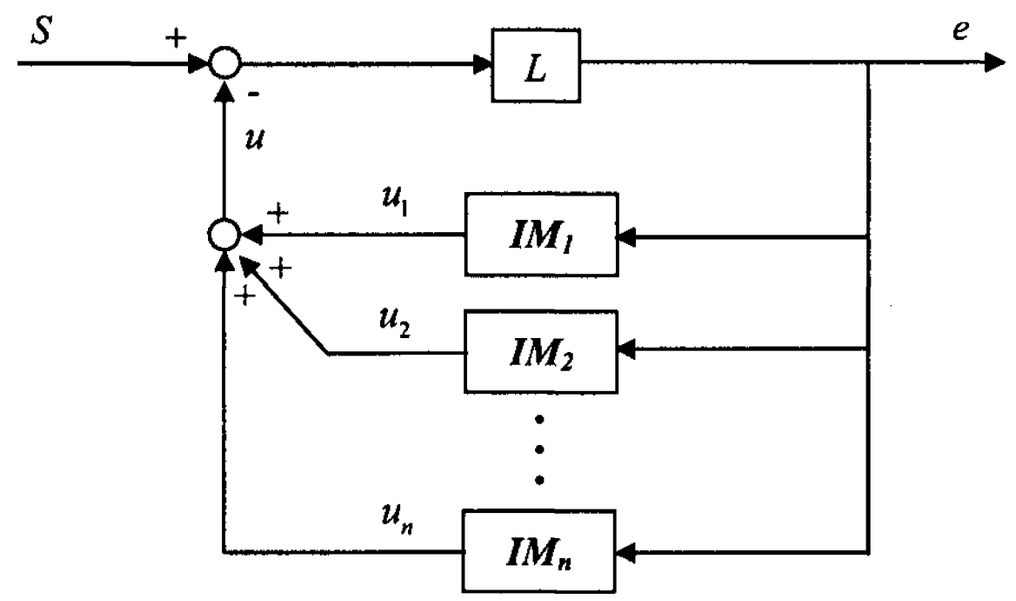

Figure 3.1: Instantaneous Fourier decomposition for an arbitrary periodic signal

IMs in the feedback loop. This can be extended to Fourier transforms that are composed of a set of narrow band signals by allowing the frequency and amplitude to vary slowly with time. This is what is referred to as instantaneous Fourier decomposition in this thesis. The block diagram of this decomposition is shown in Fig. 3.1, where L is a tuning function.

To motivate the algorithm, we consider the case where S is an arbitrary quasi-periodic signal in the form of

$$S(t) = \sum_{i=1}^{n} S_i \sin(\omega_i t + \varphi_i). \tag{3.6}$$

where ω_i and φ_i are the frequency and initial phase of the $i^{th}(i = 1,2,\cdots,n)$ are frequency component present in the signal. The essence of the decomposition is to use each individual IM to identify each component in the data. The two state variables of i^{th} IM are defined as $x_{1i}(t)$ and $x_{2i}(t)$. The state space representation of the IMs in the system as shown in Fig. 3.1 are given as follows

$$\dot{X} = \begin{bmatrix} A_1 & & & & \\ & A_2 & & & \\ & & \cdot & & \\ & & & \cdot & \\ & & & & A_n \end{bmatrix} X + \begin{bmatrix} B_1 \\ B_2 \\ \cdot \\ \cdot \\ B_n \end{bmatrix} e \tag{3.7}$$

$$u = [\, K_1 \quad K_2 \quad \cdot \quad \cdot \quad \cdot \quad K_n \,] X \tag{3.8}$$

where A_i, B_i and K_i $(i = 1, 2, \cdots, n)$ are given by

$$A_i = \begin{bmatrix} 0 & \omega_i \\ -\omega_i & 0 \end{bmatrix} \qquad B_i = \begin{bmatrix} 0 \\ 1 \end{bmatrix} \qquad K_i = [\; K_{1i} \quad K_{2i} \;] \tag{3.9}$$

and

$$X = \left[x_{11} \quad x_{21} \vdots \quad x_{12} \quad x_{22} \vdots \quad \cdots \quad x_{1n} \quad x_{2n} \right]^T \tag{3.10}$$

Without difficulty, the transfer functions from $e(s)$ to $x_{1i}(s)$ and $e(s)$ to $x_{2i}(s)$ can be easily obtained as $\frac{\omega_i}{s^2+\omega_i^2}$ and $\frac{s}{s^2+\omega_i^2}$. In steady state,

$$x_{1i}(t) = |x_i| \sin(\omega_i t + \phi_i) \tag{3.11}$$

$$x_{2i}(t) = |x_i| \cos(\omega_i t + \phi_i) \tag{3.12}$$

where

$$|x_i| = \sqrt{x_{1i}^2(t) + x_{2i}^2(t)}\,, \qquad \phi_i = \arctan\left(\frac{x_{2i}}{x_{1i}}\right) \tag{3.13}$$

The two state variables $x_{1i}(t)$ and $x_{2i}(t)$ are orthogonal, and have the same relationship as (3.5), a common causal approximation for the Hilbert transform. Therefore, we can assume $x_{2i}(t)$ is the Hilbert transform of $x_{1i}(t)$. Furthermore, just as Huang's empirical

mode decomposition is able to decompose a complicated signal into finite and often small number of IMFs, we expect the multiple IMs will decompose a quasi-periodic signal into a sum of sinusoids in terms of the state variables corresponding to each IM, generating a real time Fourier representation of the input signal.

In view of the feedback signal $u(t)$, it is a summation of the output from each IM, which is given by

$$u(t) = \sum_{i=1}^{n} u_i(t) = \sum_{i=1}^{n} (K_{1i}x_{1i} + K_{2i}x_{2i}) \tag{3.14}$$

$u(t)$ can be given in the form of

$$u(t) = \sum_{i=1}^{n} |K_i||x_i| \sin\left(\omega_i t + \arctan(\frac{K_{2i}x_{2i}}{K_{1i}x_{1i}})\right) \tag{3.15}$$

where $K_i = \sqrt{K_{1i}^2 + K_{2i}^2}$. With proper design of the feedback gain K_i, the system can be stable, and thus $u(t) = S(t)$, which implies

$$S_i(t) = |K_i||x_i| \tag{3.16}$$

$$\varphi_i(t) = \omega_i t + \arctan\left(\frac{K_{2i}x_{2i}}{K_{1i}x_{1i}}\right) \tag{3.17}$$

Thus, instantaneous Fourier decomposition is achieved, which has the same goal as EMD does.

To guarantee stability, the control gain K, where $K = [\ K_1\ K_2\ \cdots\ K_n\ ]$, has to be properly designed. Thus, the Fourier decomposition problem is translated into a control problem: How to choose L and K such that the system as shown in Fig. 3.1 is stable? In this thesis, we propose to incorporate a bandpass filter into the algorithm, so as to enforce

the condition that only a small number of tones will be considered as relevant. Considering the IM exhibits one distinguished property of a narrow band notch filter, multiple notch filters should be incorporated in the system as well. Thus the desired system behaves as a bandpass filter with notches. The system can thereby generate the instantaneous Fourier series of the input signal as well as has the ability to isolate the useful signal and reject noises. The details of the design of an adaptive bandpass filter with an adjustable notch can be found in [51, 53].

3.3 Instantaneous Fourier Decomposition for Signals with Exponentially Decaying Terms

In the preceding section, the instantaneous Fourier decomposition was applied to a quasi-periodic signal. In practice, however, real-world signals often have nonperiodic components. For a nonperiodic signal, the Fourier series can be given by

$$S(t) = S_0(t) + \sum_{i=1}^{n} S_i \sin(\varphi_i(t)) \tag{3.18}$$

where

$$\varphi_i(t) = \int_0^t \omega_i(t)dt + \varphi_i(0) \tag{3.19}$$

$S_0(t)$ in 3.18 represents the nonperiodic component of $S(t)$. $\varphi_i(0)$ in (3.19) is the initial phase. For a signal of voltage or current, the nonperiodic component is often a time-decaying exponential, that is, $S_0(t) = ae^{-\sigma t}$ $(\sigma > 0)$. Since $t \to \infty$, $e^{-\sigma t} \to 0$, this term

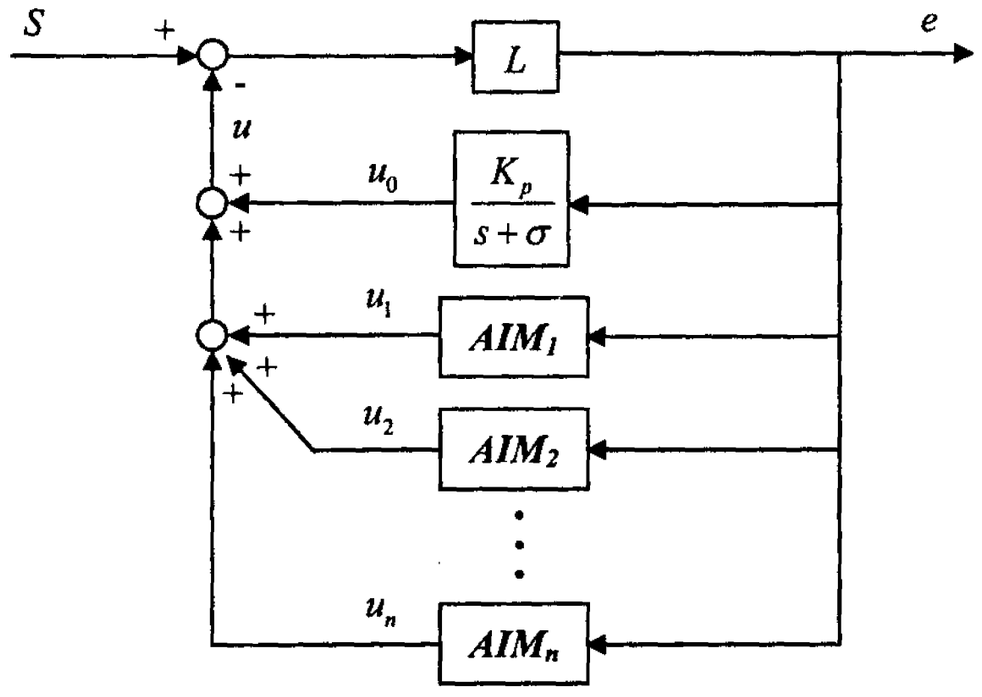

Figure 3.2: Instantaneous Fourier decomposition for a nonperiodic signal

does not affect the performance in steady state, but it will result in worse transient response. In order to obtain the most accurate representation of the signal, the system should reflect this nonperiodic component. Thus, a term with transfer function of $\frac{Kp}{s+\sigma}$ can be added in the feedback loop in parallel with the AIMs, each of which has the same structure as described in Section 1.2. Fig. 3.2 gives the block diagram for such signals. Correspondingly, L, K, K_p can be determined by designing the system as a bandpass filter with notches plus a zero with the zero located at $-\sigma$. A theoretical analysis of the system producing this signal is presented in **Appendix B**.

3.4 Application to Experimental Weld Voltage Data

To demonstrate the effectiveness of the proposed algorithm, an application to real time experimental weld voltage data collected from a welding machine is studied. The data, as shown in Fig. 3.3, is nonstationary, and will be applied to the proposed algorithm.

Fig. 3.4 shows both the magnitude and the phase of the data by fast Fourier transformation (FFT). It can be clearly seen from the subplot of the magnitude that four com-

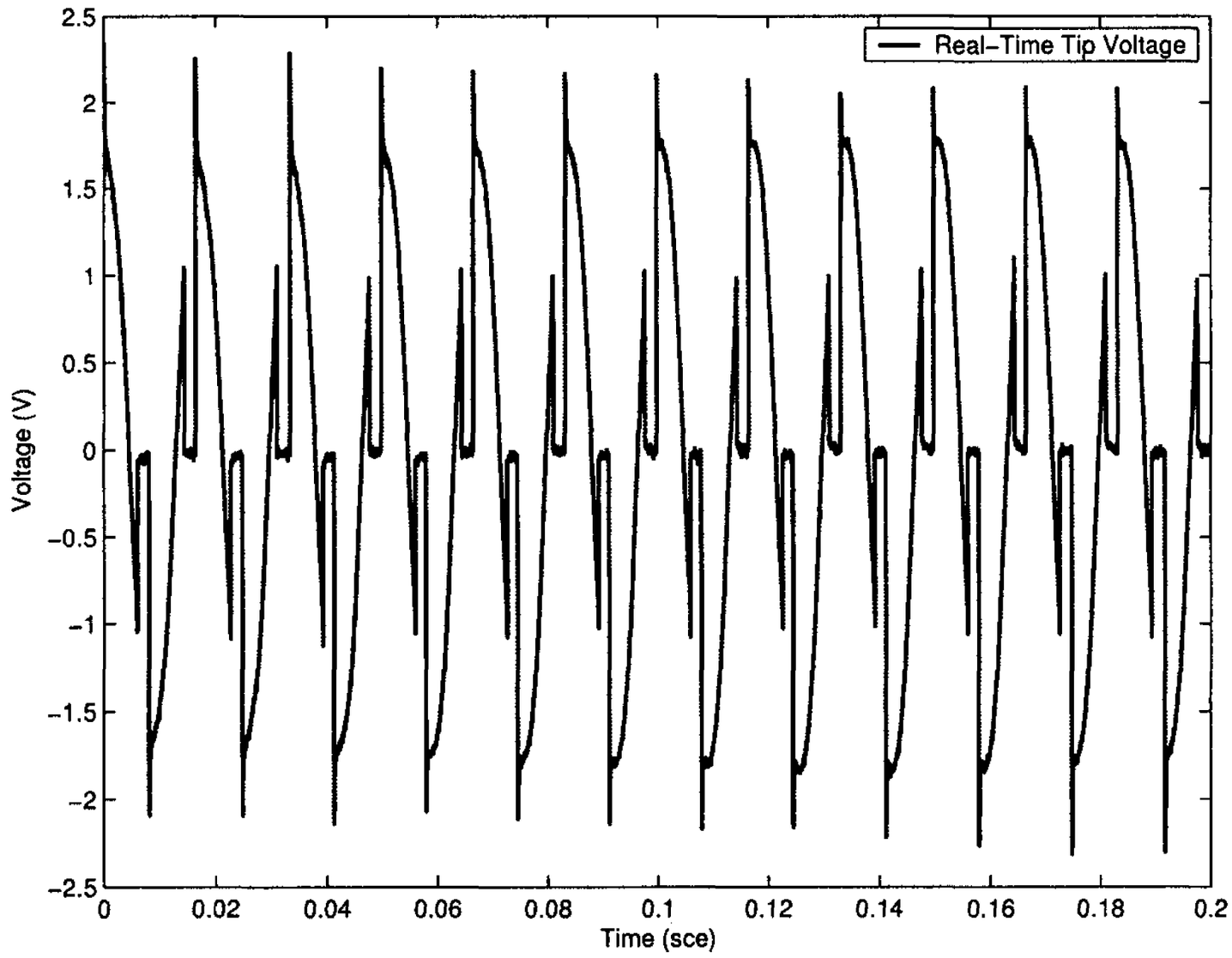

Figure 3.3: Experimental weld voltage data

ponents with frequencies of $60Hz$, $180Hz$, $300Hz$ and $420Hz$, dominate the experimental signal, but they cannot tell much about the dynamic characteristic of the signal.

Fig. 3.5 demonstrates the dynamic behaviour of these four components decomposed by our four IMs of the proposed algorithm from the same data. The relevant estimation system and the corresponding specified parameters will be discussed in detail in Subsection 4.5.2 in Chapter 4. For comparison purposes, the first four components obtained by FFT as shown previously are also plotted in Fig. 3.5. It clearly shows that the results from our instantaneous Fourier decomposition demonstrate the time varying behaviour of the relevant components, while Fourier transform can only give constant values.

Furthermore, Huang's empirical model decomposition does not result in decomposition into sums of narrow band signals for this class of signals. To demonstrate this, EMD is applied to a noise free, stationary truncated sinusoid as is produced by a silicon-controlled-

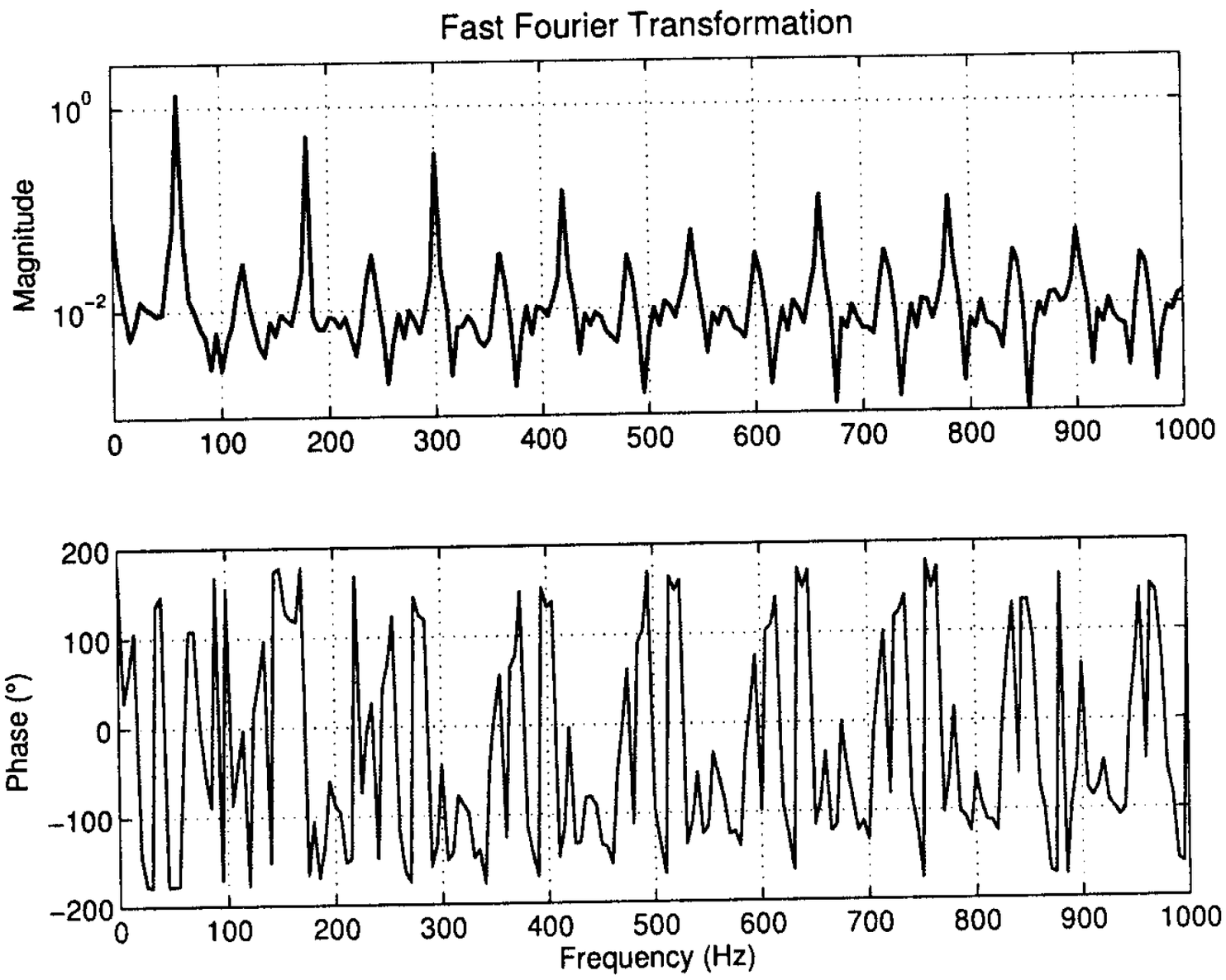

Figure 3.4: Fast Fourier transformation for experimental weld voltage data

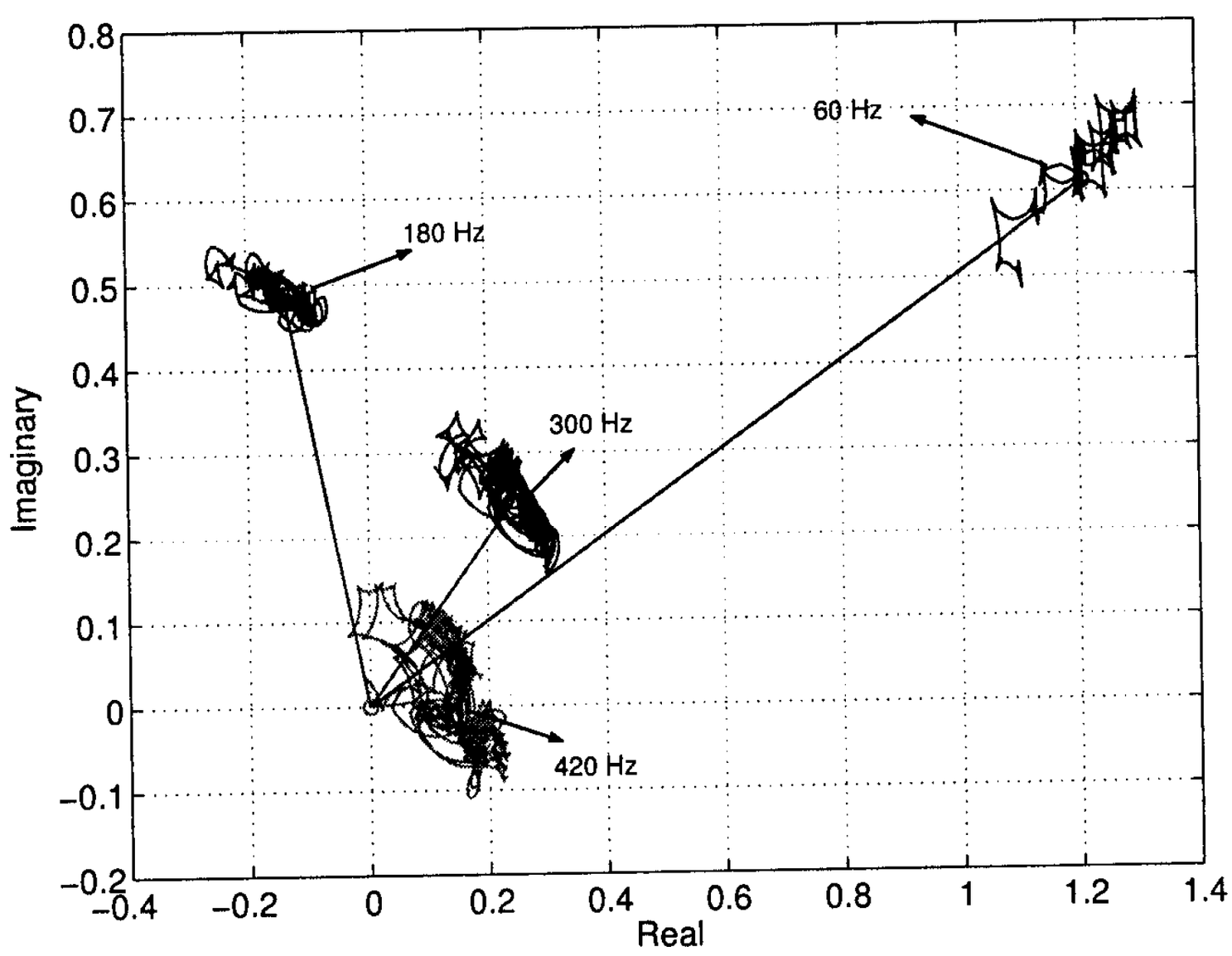

Figure 3.5: Instantaneous Fourier decomposition for experimental weld voltage data

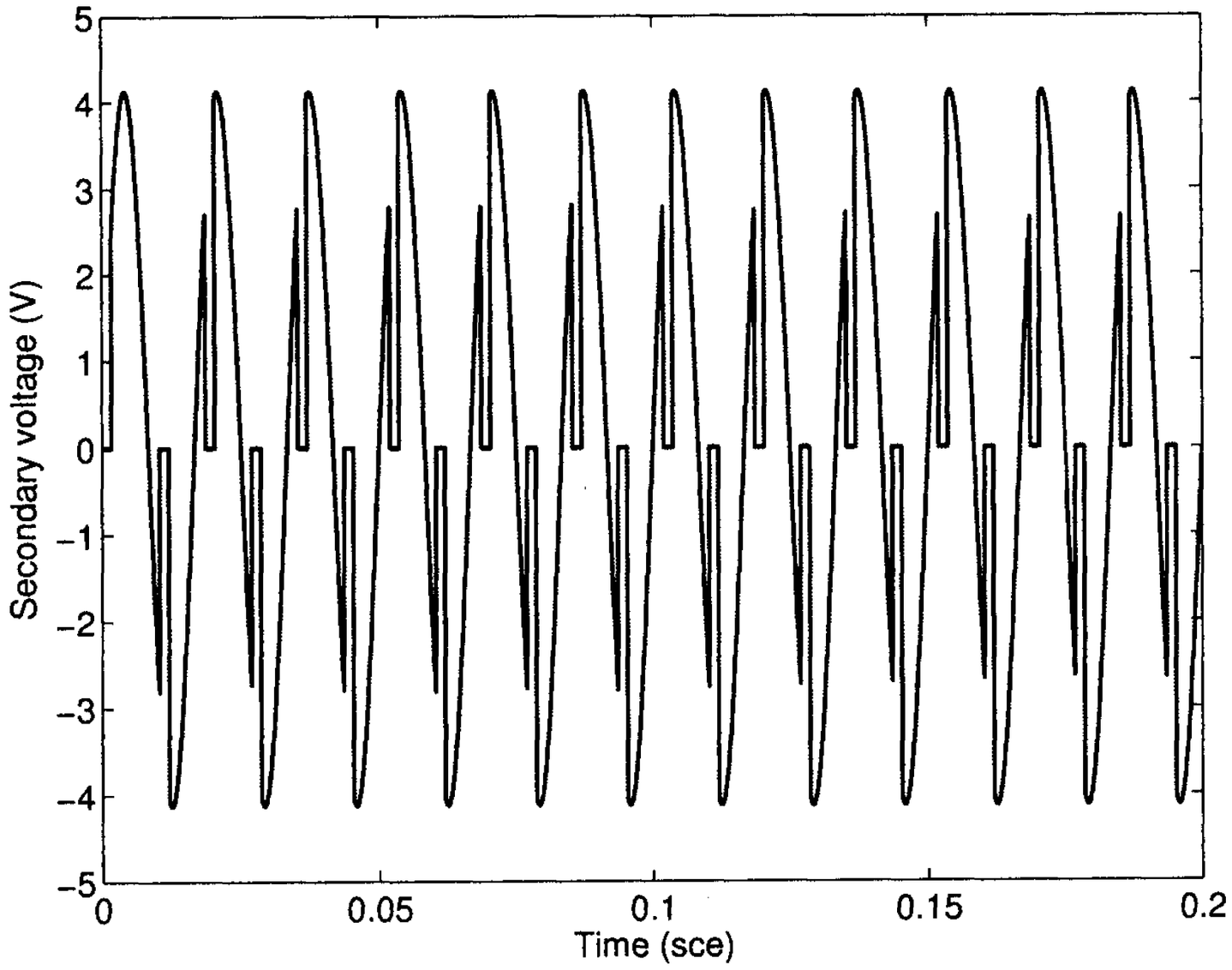

Figure 3.6: Synthesized secondary voltage from SCR model

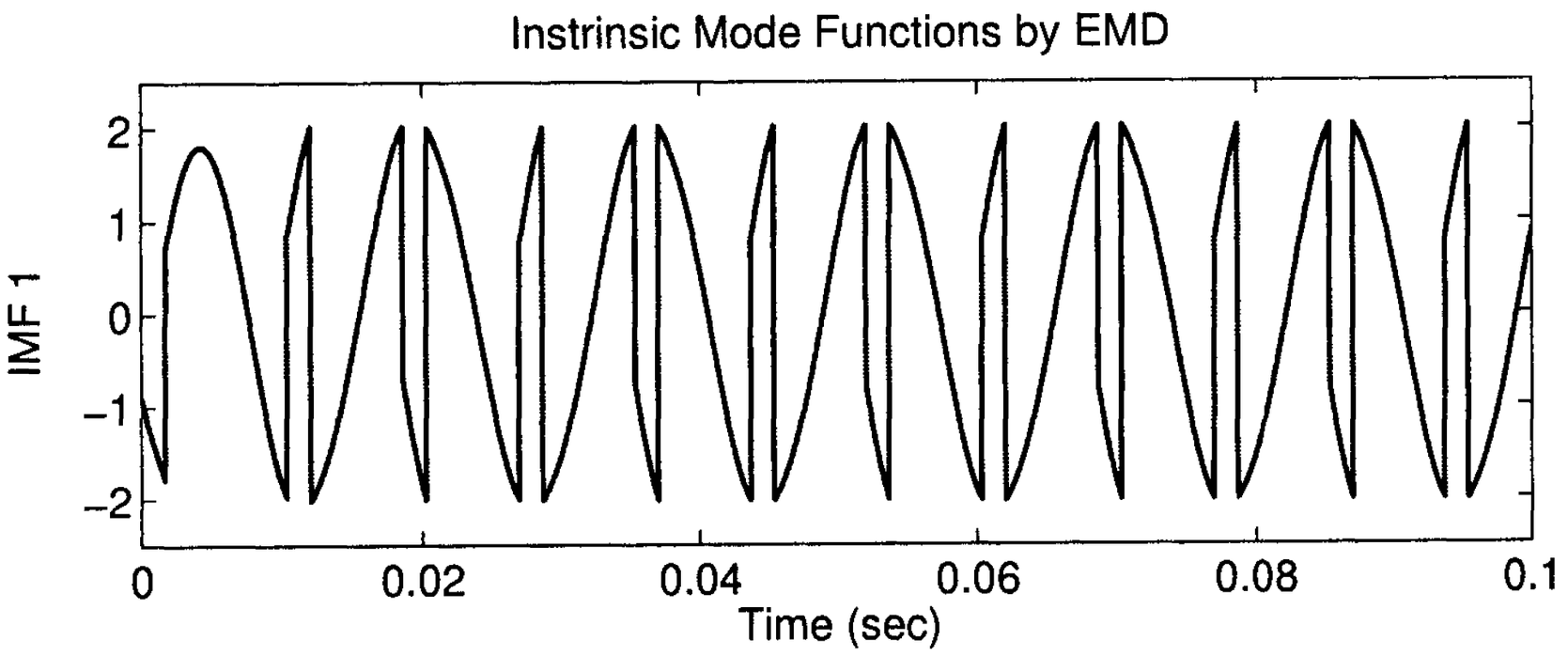

Figure 3.7: The first two IMFs by EMD for noise free and stationary voltage

rectifier (SCR) as shown in Fig. 3.6. This was done to show that the effect is not a result of noise or other artifact. Fig. 3.7 shows the first two intrinsic mode functions decomposed by EMD. Higher IMFs model the window applied to the data. The first IMF clearly represents a signal that is not narrow band but contains multiple harmonics.

3.5 Conclusion

In this chapter, a new method for analyzing nonstationary data has been developed. The key part of the method is the 'instantaneous Fourier decomposition' with which any complex data can be decomposed into a finite and often small number of sines and cosines, generating a Fourier series representation. Since the decomposition is based on the state variables of IMs connected in parallel in the feedback loop of the system, it is intuitive, direct, simple and adaptive, and can be implemented in real time.

Chapter 4

Instantaneous Fourier Decomposition Applied to Real Time Measurement in RSW Process

4.1 Introduction

Resistance spot welding (RSW) is one of the oldest but most productive and competitive joining techniques in use by automotive, aerospace, electrical, electronics, radiators and other metal processing industries. The process uses two shaped copper alloy electrodes to concentrate welding current between the materials to be welded. The result is a small 'spot' that is quickly heated to the melting point, forming a nugget of welded metal after the current is removed [54]. The principle benefits of RSW are high speed, low cost operation, and adaptability for automation in high volume production. In the automotive industry, for example, with an average of 2,000 to 5,000 spot welds performed on each manufactured car, RSW is used almost universally to weld the sheet metal forming a car.

However, despite its advantages, RSW suffers from a major quality variation problem, i.e., inconsistent quality from weld to weld [23]. This results from: 1) the complexity of the basic process which involves interactions among electrical, thermal, mechanical, and

metallurgical phenomena; 2) numerous sources of variation, noise, and errors, such as variations in surface conditions, available power, progressive degeneration of weld electrodes, and power cables [55], etc.. Though the relationship between weld quality and the various process conditions has not yet been systematically studied, any uncertainty in the process coming from variability surely reduces the weld quality, demands more welds to be produced than are needed if each was perfect, and thus drives up costs. For this reason, as well as to meet the recently great demands from industry to weld new materials such as high strength steels, aluminium and complex joints, new methods for process control and innovative applications for improving weld qualities are in great demand. Due to the extensive use of RSW, particularly in auto bodies, even a small improvement would bring significant economic benefits.

In order to detect and correct the defective welds as soon as they occur, it is very important to study the relationships between the quality of the resistance welding spots and signal curves measured during the welding event. If some indication of the quality of a joint could be gathered from the signal curves, real time monitoring could be achieved to ensure a perfect weld every time, the need for destructive testing could be reduced. This would lead to savings in material and production costs and more effective operation of the quality-assurance process.

As the name of RSW implies, it is the resistance to current flow of the material to be welded that causes localized heating in the part. The variation of weldment resistance over time, or more specifically, the dynamic resistance in the transformer secondary circuit during the course of the weld, is an important explanatory variable that can be monitored in real time for weld quality control. Moreover, in industrial environments, the welding

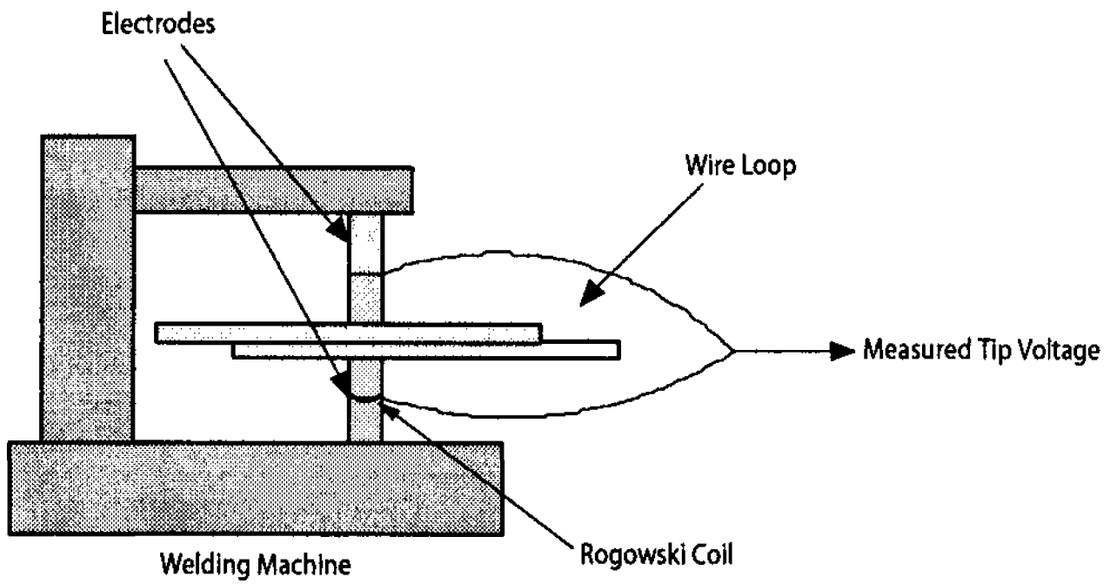

Figure 4.1: Illustration of the wire loop for tip voltage and current measurement

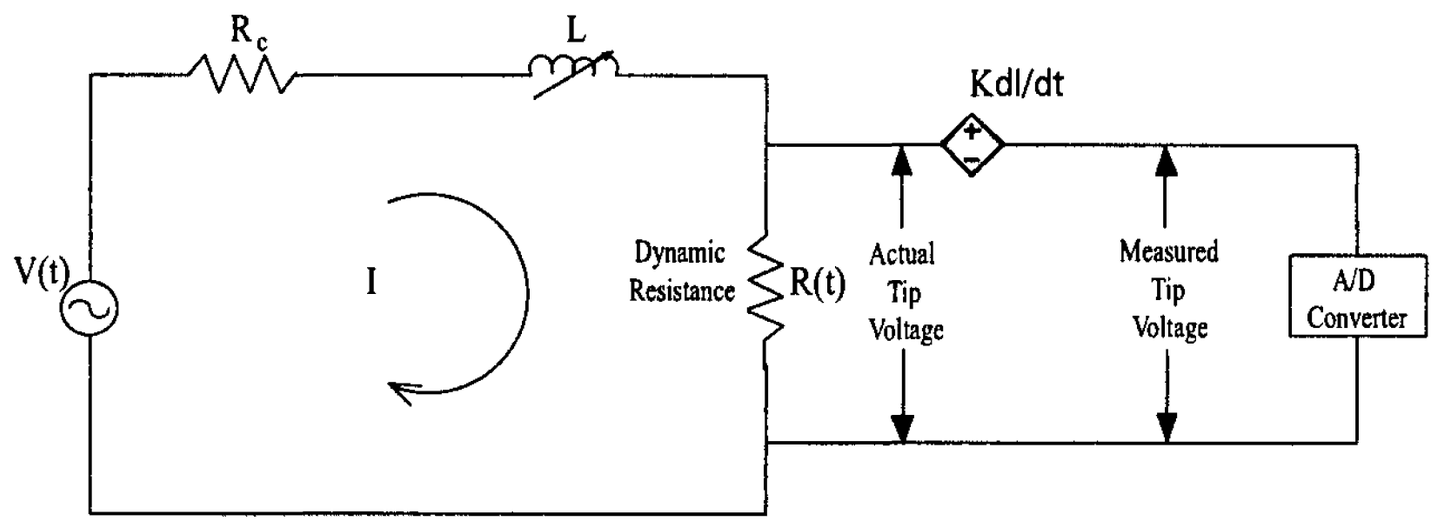

Figure 4.2: Electrical schematic of the secondary loop in RSW

current and tip voltage signals can be more easily and economically acquired than other signals. Thus, to provide a reliable real time measurement of the secondary dynamic resistance is our goal in this research.

4.2 Secondary Weld Circuit Measurements

The essence of the measurement of the secondary dynamic resistance is to measure the tip voltage at the electrodes and current through the electrodes in the secondary circuit of RSW. As an example, Fig. 4.1 illustrates the wiring of the measurements in lab environment for this study. Fig. 4.2 shows the corresponding equivalent electrical schematic of this measurements, in which $V(t)$ is the secondary voltage served as the power supply of the

secondary circuit, R_c is the cable resistance, L is the cable inductance, and $R(t)$ is the dynamic resistance across the electrodes that is being measured.

The current I is detected by a Rogowski coil, an air-cored toroidal coil that is placed around the conductor. The derivative of current is the measured quantity obtained from the toroid, presented as an induced voltage from a time varying magnetic field in the space around the conductor. This toroid voltage, which is defined as $v(t)$, can be electronically integrated to provide an indirect measurement of the weld current, via the equation [56]

$$I(t) = -\frac{1}{M}\int v(t)dt \tag{4.1}$$

The voltage drop due to the dynamic resistance $R(t)$ is measured by clipping two wires, one on each electrode. By doing so, a loop is formed in the circuit through which the magnetic flux is produced by the high current flows. This generates an error in the measured tip voltage. The induced error is proportional to the rate of the current change, given by Faraday's law [57]

$$V_n = K\frac{dI}{dt} \tag{4.2}$$

where V_n is the induced voltage error, dI/dt is the current change with respect to time, K is a scaling constant which is proportional to the area of the loop and the angle that the loop makes with the magnetic field. Though the induced error can be reduced to some extent by twisting the pair of sensing wires, enough slack must be left for allowing opening and closing of the electrodes, and insertion of the workpieces. With the very large current and the low tip voltage, the induced voltage is generally larger than the voltage signal being

measured. Therefore, the measured tip voltage, V_m, is not the actual voltage drop V_a at the electrodes. Instead, it includes two parts, which is given by

$$V_m = V_a + V_n \tag{4.3}$$

In practice, $V_a < V_n$. When the measured voltage signal is employed for calculating the dynamic resistance, this error can not be ignored.

4.3 Limitations of the Existing Methods for Dynamic Resistance Measurement

Generally, when the weld voltage and current are well measured, the resistance can be calculated straight forward by using Ohm's Law:

$$R = \frac{V}{I} \tag{4.4}$$

However, (4.3) shows that the measured tip voltage is not the actual tip voltage. It cannot be directly used for resistance calculation. Therefore, in order to extract meaningful information of the actual tip voltage from the raw measured voltage signal, elimination of induced error is crucial for accurate measurement of the dynamic resistance in RSW.

There are several techniques of doing this. Two of them are well-known as the peak method [40] and the compensation method [41], respectively. The peak value method achieves this by calculating $R(t)$ only at the time instants where current peaks occur [27].

At the peak, $\frac{dI}{dt} = 0$, hence $V_n = 0$, and $V_m = V_a$. This method is accurate as long as the sample rate is fast enough to catch the true peaks. However, it is inconvenient to find peaks and zero crossings. Moreover, the measurement is discontinuous since only one voltage measurement is available per half cycle. It cannot provide a complete time varying representation of the dynamic resistance. Also, the greatest resistance, and greatest resistance variance occur during the first quarter cycle of the weld, when no measurements are available. This is a serious disadvantage for any feedback control scheme using dynamic resistance [57].

Conversely, the compensation method can be achieved by two ways: one is to place two additional wires in parallel with the normal measurement wires and short them together instead of connecting them to electrodes. When the added loop is exactly the same as that of the measuring loop, continuous measurement of the induced noise is achieved and can be subtracted form the measured tip voltage. The drawback of this method is that it requires an extra measurement that needs to be taken precisely at that same time as the existing tip voltage. This precision in timing is necessary because the derivative of the current contains large steps as a result of the chopping of the current from the silicon-controlled-rectifiers. The need for exactly matching of the wire loops can be partially achieved by using twisted pair. However, to match loops at the electrodes requires a short circuit produced by the most direct path possible. This makes the approach impractical on the shop floor since the motion of the electrodes and access to workpieces require the short circuit to be produced by a relatively long path. Another way to achieve the compensation is to subtract the exact amount of the error from the measured signal when the current derivative is available. Since currents are commonly measured with a Rogaski coil, this measurement is often freely

available. To achieve this, the scaling constant K in (4.2) has to be precisely determined. However, this is only practical in laboratory environment. In the real world, K will vary with the wire placement. Since K is often predetermined offline, this variation makes the compensation not viable for measuring the resistance on factory floor.

In addition, for AC power welders, some other limitations arise when using (4.4) to calculate the dynamic resistance. They can be summarized as follows:

- Even when the measured V and I are continuous, since I is a sinusoid, calculating $R = \frac{V}{I}$ is still not valid when I is too small or close to 0. This will give a division by zero error in the calculations.

- The AC power supplies used in spot welding are primarily SCR controlled. The SCR controlled power supplies produce significant harmonics in the input signal. This makes the calculation of the resistance even more complicated.

4.4 A Reliable Technique for Estimation of the Dynamic Resistance

As discussed earlier, elimination of induced error from the measured voltage signal is the key step for accurate measurement of the dynamic resistance in RSW. Though many researchers [57, 58] have acknowledged it, no effective way is provided to deal with it up to date. In this thesis, a projection approach is proposed to extract the actual tip voltage magnitude from the measured noisy voltage signal.

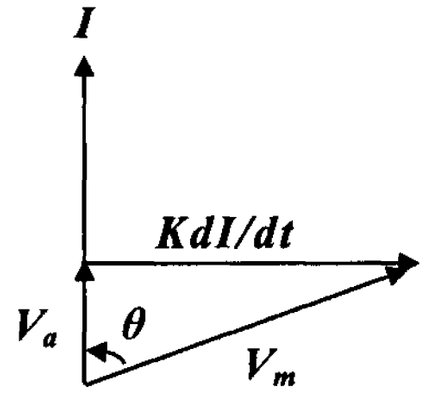

Figure 4.3: Relationship between V_a and V_m

4.4.1 Fundamentals of Dynamic Resistance Measurement

From (4.2) and (4.3), the actual tip voltage V_a can be solved from its measurement V_m by

$$V_a = V_m - K\frac{dI}{dt} \tag{4.5}$$

Since the dynamic resistance $R(t)$ is assumed to be purely resistive, the actual tip voltage V_a is in phase with the current I. Thus, by representing the sinusoidal current and voltage signals as phasors, for each single harmonic, the geometric relationship between V_a and V_m can be plotted as in Fig. 4.3. From the plot, we can see that the actual tip voltage V_a is the projection of the measured voltage V_m on the current I. Therefore, the magnitude of V_a can be calculated by dividing the dot product of V_m and I by the magnitude of I, which can be represented by

$$|V_a| = \frac{|V_m||I|\cos\theta}{|I|} = \frac{V_m \cdot I}{|I|} \tag{4.6}$$

With the magnitude of the actual tip voltage, the dynamic resistance can thereby be calculated by division of the magnitude of actual tip voltage by magnitude of current, which is represented by

$$R = \frac{|V_a|}{|I|} \tag{4.7}$$

The advantages of this projection approach to calculate the dynamic resistance include:

- The induced error is eliminated from the measured voltage signal.
- It provides a continuous measurement of the tip voltage and dynamic resistance without calibration.
- It does not have division by zero problem since the resistance is calculated by the magnitudes of voltage and current.
- It can be performed without measuring dI/dt.
- K can be estimated when dI/dt is measured.

Since the projection approach in (4.6) is based on single phasor, when the measured voltage and current contain harmonics, they have to be decomposed into a sum of single tone signals first. The previously proposed internal model based instantaneous Fourier decomposition algorithm can achieve this. For AC powered RSW, the fundamental frequency is $60Hz$, and the high frequency components are the odd harmonics of $60Hz$. Since the variations of the frequencies are very small, the frequencies are considered as known. Thus, they do not need to be updated. Therefore, for instantaneous Fourier decomposition, regular IMs are used rather than AIMs as shown in Fig. 3.2. Basically, the estimation requires: 1) online measurement of time series of $V_m(t)$ and $I(t)$ at uniform time intervals; 2) two internal model based estimation systems are used to decompose the measured signals $V_m(t)$ and $I(t)$ into sums of harmonics, representing instantaneous Fourier series representations; 3) estimation of the magnitude of current $|I|$ from the Fourier series representation of current; 4) estimation of the magnitude of the actual tip voltage $|V_a|$ from the projection of V_m

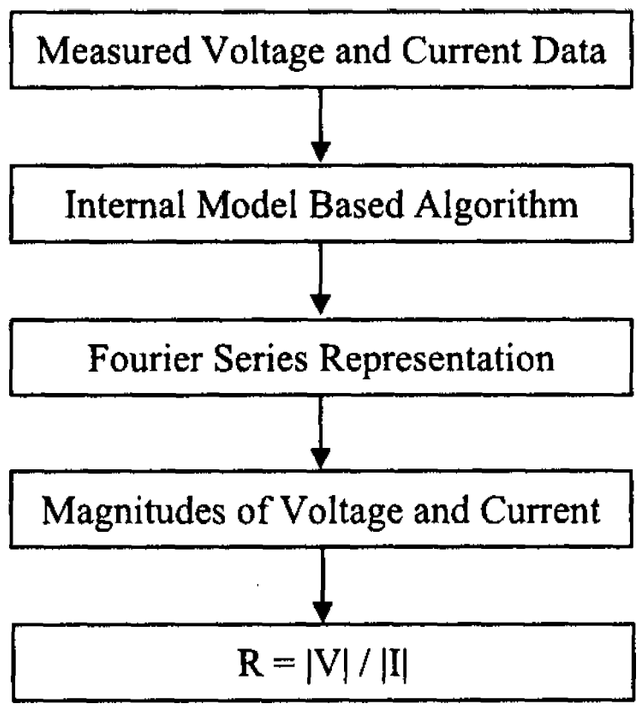

Figure 4.4: Illustration of the internal model based estimation scheme for dynamic resistance measurement

on I; 5) the dynamic resistance is calculated by (4.7) for each harmonic. Theoretically, they are identical to each other. Fig. 4.4 illustrates the estimation scheme for this procedure.

4.4.2 Tuning of Internal Model Based Instantaneous Fourier Decomposition System

In order to decompose the measured signals $V_m(t)$ and $I(t)$ into instantaneous Fourier series representations as stated above, the two internal model based estimation systems have to be properly designed. The two estimation systems are independent but have the same structure with same tuning parameters. Following will introduce a methodology to pick the tuning parameters. Goal is to incorporate a bandpass filter into design.

The original periodic disturbance cancellation system shown in Fig. 1.1 has the transfer function in the form of $\frac{L(s)(s^2+\omega^2)}{L(s)s+(s^2+\omega^2)}$. When $s = j\omega$, the magnitude of the transfer function is zero, exhibiting one property of a narrow band notch filter. Therefore, the internal model based estimation system described in Chapter 3 is designed to behave as a bandpass filter with notches to guarantee stability of the system and to enforce the condi-

tion that only a small number of harmonics will be considered as relevant. The bandpass filter, defined as $T_{bp}(s)$, is chosen as a commonly used Chebyshev bandpass filter with center frequency ω_0 and bandwidth BW, so that the input signal magnitude with frequencies outside the pass band will be monotonically decreased and eliminated. The designed tuning function $L(s)$ has the same order as that of the bandpass filter. The number of the IMs in the estimation system is the same as the number of the harmonics present in the input signal, with transfer function of $T_{fi}(s) = \frac{K_{2i}s+K_{1i}\omega_i}{s^2+\omega_i^2}$. The number of the notch filters is the same as the number of the IMs with transfer function of $T_{ni}(s) = \frac{s^2+\omega_i^2}{s^2+2\varepsilon_i\omega_i s+\omega_i^2}$. By matching the coefficients of the bandpass filter in series with the notch filters and the tuning function with IMs in the feedback loop given by

$$T_{bp}(s)\prod_{i=1}^{n}T_{ni}(s) = \frac{L(s)}{1+L(s)\sum_{i=1}^{n}T_{fi}(s)} \tag{4.8}$$

the form and the coefficients of $L(s)$ and the values of the feedback gains $(K_{1i},\ K_{2i})(i = 1,2,\cdots,n)$ can be determined. The detailed procedure can be found in **Appendix C**.

4.4.3 Estimate of $|I|$

With properly designed tuning function $L(s)$ and feedback gain K, the internal model based estimation system can decompose a multi-tone signal into single-tone signals, generating a Fourier Series as given by (3.14). When n IMs are employed to identify the input signal of voltage or current with n harmonics in the form of (3.6), the i^{th} $(n = 1,2,\cdots,n)$ harmonic

estimated from the i^{th} IM is given by

$$S_i \sin(\omega_i t + \varphi_i) = K_{1i} x_{1i} + K_{2i} x_{2i} \tag{4.9}$$

where K_{1i}, K_{2i} are the two feedback gains with respect to the two state variables x_{1i}, x_{2i} of the i^{th} IM. The magnitude of the i^{th} harmonic $|S_i|$ can be solved from (3.16), where the slowly time varying magnitude of the states $|x_i|$ has to be known. Since x_{1i}, x_{2i} are in the form of sine and cosine, respectively, $S_i \cos(\omega_i t + \varphi_i)$ can be easily obtained by

$$S_i \cos(\omega_i t + \varphi_i) = -K_{2i} x_{1i} + K_{1i} x_{2i} \tag{4.10}$$

Thus, as a alternative, $|S_i|$ can be solved directly from the two time varying state variables by

$$|S_i| = \sqrt{(K_{1i} x_{1i} + K_{2i} x_{2i})^2 + (-K_{2i} x_{1i} + K_1 x_{2i})^2} \tag{4.11}$$

In this way, the magnitude of the i^{th} harmonic of current $|I_i|$ $(i = 1, 2, \cdots, n)$ can be estimated when the input of the estimation system is the measured current signal.

4.4.4 Estimate of $R(t)$

Similarly, each harmonic contained in the measured voltage signal can be identified by the corresponding internal model incorporated in the voltage estimation system. For each harmonic, the magnitude of the actual tip voltage can be obtained by (4.6) in terms of the corresponding current and its magnitude. The overall root mean square (RMS) voltage

magnitude is given by $|V_a| = \sqrt{\frac{1}{2}\sum_{i=1}^{n}|V_{ai}|^2}$. With the estimates of the magnitudes of voltage and current for each harmonic, the dynamic resistance $R(t)$ can be estimated by (4.7) from each IM. Corresponding, n IMs provides n pairs of the estimates of the resistance.

4.5 Results

To demonstrate the effectiveness of the proposed estimation technique, simulations are conducted under Mathworks SIMULINK environment using computer generated data sets which address two concerns: 1) input data with finite harmonics; 2) SCR model controlled data with infinite harmonics. Finally, the algorithm is applied to experimental data from an actual resistance spot welder.

4.5.1 Simulation Results for Synthesized Data

To validate the algorithm, synthesized voltage and current data were used as the inputs of the estimation system to calculate the dynamic resistance. The estimated resistance is then compared with its known value to determine how well the algorithm works. A typical dynamic resistance curve that provides very meaningful information regarding the real-world nugget growth is shown in Fig. 4.5. Both the known resistance and the synthesized data set of voltage and current were generated on the values obtained from the experimental data acquired from welding machines located at The University of Waterloo with a sampling rate of 25 KHz and 5000 sample points.

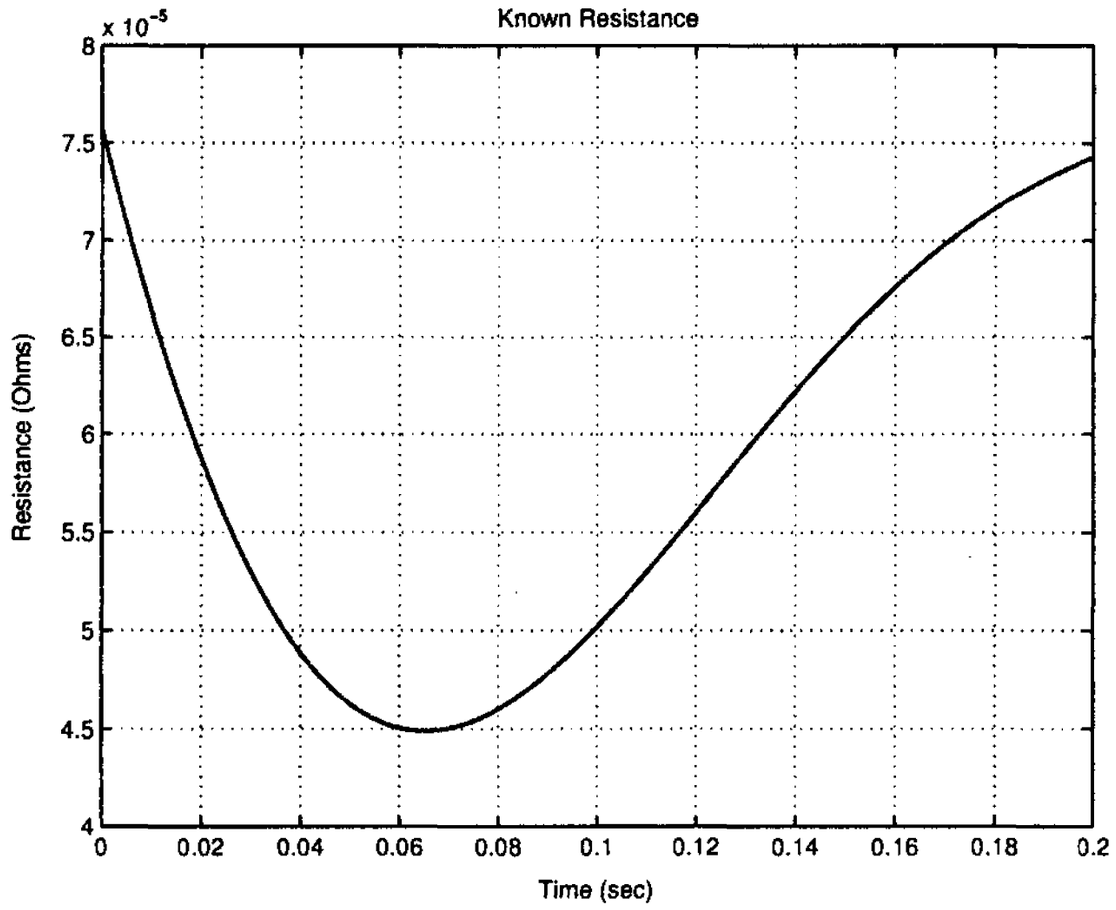

Figure 4.5: Typical dynamic resistance curve

4.5.1.1 Synthesized Data Generation

The synthesized voltage/current dataset is generated by a Simulink data generation model. The model is built based on the secondary electrical loop of welding circuit in Fig. 4.2. As an example, Fig. 4.6 shows a Simulink model to generate a pair of measured voltage/current data for a input with three harmonics. The values of R_c, L, and the scaling constant K were calculated from the shop-floor data acquired from laboratory welding system after noise filtration (see Appendix D). The typical values used here are $R_c = 161.5\mu\Omega$, $L = 0.5675\mu H$, and $K = 4.6298 \times 10^{-7}$, respectively. The secondary voltage $V(t)$ serves as the input of the data generation model with typical magnitude of $4.125V$.

As the outputs of the model, the measured tip voltage V_m and the current I provide the inputs for the internal model based estimation systems. The internal models can not only provide the Fourier series representations of the input signals, but also give the magnitude of the actual tip voltage V_a and the estimate of the dynamic resistance R. Ideally, for a pure

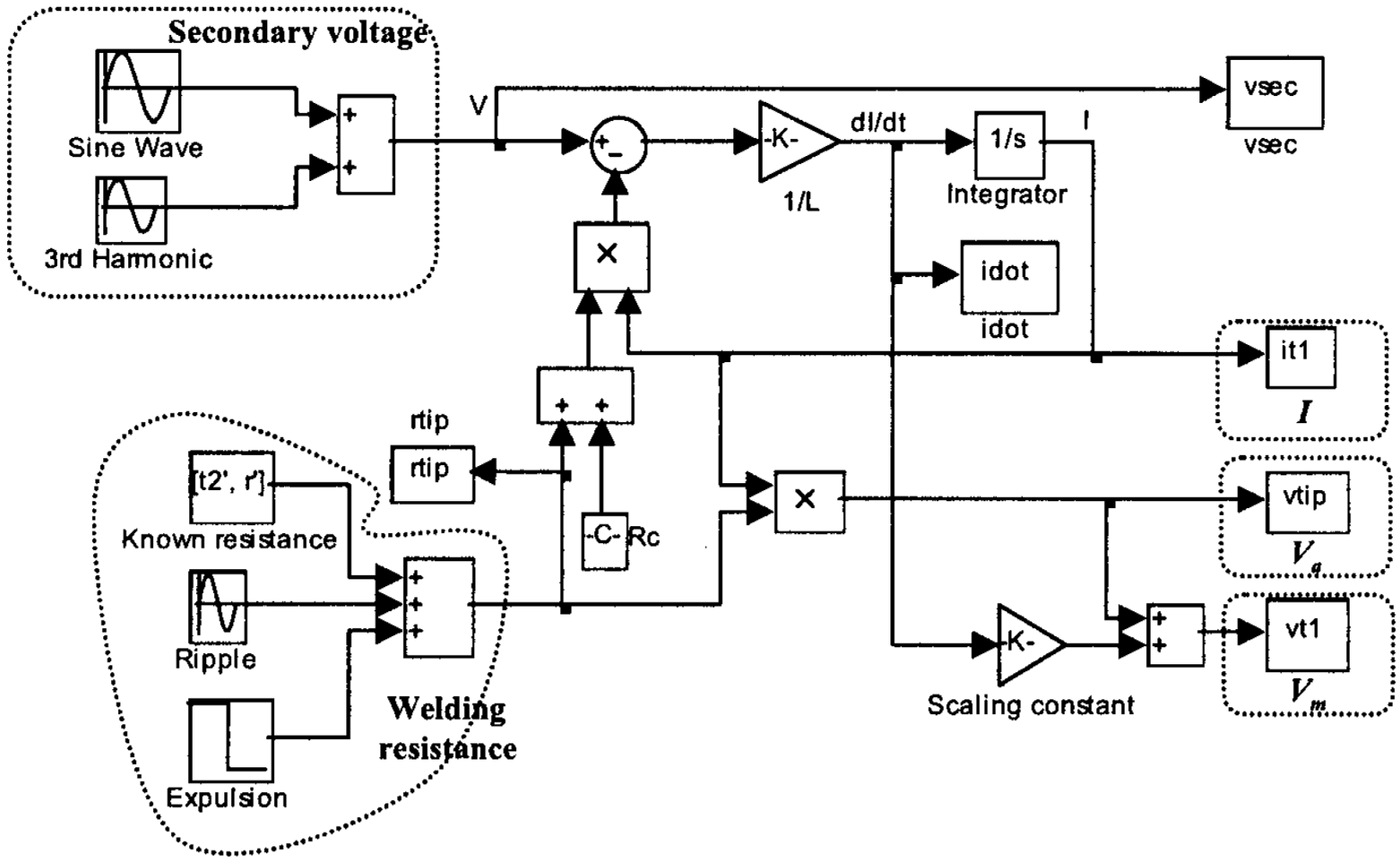

Figure 4.6: An example of a Simulink model to generate measured voltage and current

sinusoid case, where only one IM is used for each input signal, the estimated tip voltage magnitude will be the peak values of V_a; the estimate of the resistance will match its known values. For the case with harmonics, where multiple IMs are applied for each input, neither the individual magnitudes nor the RMS of the signal will have an obvious relation to the peak of the waveform.

4.5.1.2 Initial Conditions

The initial conditions is a critical factor for the internal model based estimation algorithm. Correct selection of the initial conditions for the IMs can minimize transient behaviour. Therefore, the initial values of the voltage or current signal and its derivative for each IM has to be carefully considered and incorporated in the system. In this thesis, the initial values were calculated based on the fundamental theory of the secondary weld circuit as shown in Fig. 4.2. From the concept of AC circuit, when one of the n harmonics contained in the secondary voltage $V(t)$ is $v_i(t) = V_i \sin \omega_i t$ $(i = 1, 2, \cdots, n)$, the current output of the

secondary loop in terms of v_i is given by Ohm's law

$$i_i(t) = I_i \sin(\omega_i t - \phi_i) = \frac{V_i}{Z_i} \sin(\omega_i t - \phi_i) \tag{4.12}$$

where Z is the equivalent impedance of the circuit, ϕ_i is the phase lag which are defined by

$$\begin{aligned} Z_i &= \sqrt{R^2(t) + R_c^2 + (\omega_i L)^2} \\ \phi_i &= \arctan\left(\frac{\omega_i L}{R(t) + R_c}\right) \end{aligned}$$

In steady state, the output of the corresponding i^{th} IM is identical to the input $i_i(t)$, that is

$$K_{1i}x_{1i} + K_{2i}x_{2i} = I_i \sin(\omega_i t - \phi_i) = i_i(t) \tag{4.13}$$

Furthermore,

$$-K_{2i}x_{1i} + K_{1i}x_{2i} = I_i \cos(\omega_i t - \phi_i) = \frac{di_i(t)}{dt}/\omega_i \tag{4.14}$$

Therefore, the initial conditions of $(x_{1i}(0), x_{2i}(0))$ for i^{th} IM with input of $i_i(t)$ can be solved by the following set of equations

$$\begin{cases} K_{1i}x_{1i}(0) + K_{2i}x_{2i}(0) = \dfrac{V_i}{\sqrt{R^2(0)+R_c^2+(\omega_i L)^2}} \sin\left(\arctan\left(\dfrac{-\omega_i L}{R(0)+R_c}\right)\right) = I_o^i \\ -K_{2i}x_{1i}(0) + K_{1i}x_{2i}(0) = \dfrac{V_i}{\sqrt{R^2(0)+R_c^2+(\omega_i L)^2}} \cos\left(\arctan\left(\dfrac{-\omega_i L}{R(0)+R_c}\right)\right) = I_{do}^i \end{cases} \tag{4.15}$$

Similarly, the initial conditions of $(x_{1i}v(0), x_{2i}v(0))$ for i^{th} IM with input of $v_{mi}(t) = i_i(t)R(t) + K\frac{di_i(t)}{dt}$ can be solved by

$$\begin{cases} K_{1i}x_{1iv}(0) + K_{2i}x_{2iv}(0) = I_o^i R(0) + K\omega_i I_{do}^i \\ \\ -K_{2i}x_{1iv}(0) + K_{1i}x_{2iv}(0) = I_{do}^i R(0) - K\omega_i I_o^i \end{cases} \tag{4.16}$$

where K is the scaling constant. When the initial conditions for each harmonic source are applied to its corresponding IM, the transient response of each output signal will be significantly reduced.

The voltage and current in a simple RL circuit will generally contain an exponentially decaying term. This term can be incorporated in the analysis as described in Section 3.3. A model with transfer function of $\frac{K_p}{s+\frac{R(0)+R_C}{L}}$ will be included in the feedback loop for each estimation system in parallel with the n IMs. The calculations of initial conditions of each IM will remain the same as above, while the initial value for the integrator of the compensated zero term is

$$i_s(0) = i(0) - \sum_{i=1}^{n} (K_{1i}x_{1i}(0) + K_{2i}x_{2i}(0)) \tag{4.17}$$

$$v_s(0) = v_m(0) - \sum_{i=1}^{n} (K_{1i}x_{1iv}(0) + K_{2i}x_{2iv}(0))$$

4.5.1.3 Simulation Results to Synthesized Data with Finite Harmonics

Following are the simulation results to synthesized data with finite harmonics. The synthesized data used as the test signals are listed as below:

- Pure sinusoidal input current and voltage signals to represent a clean power supply.
- Pure sinusoidal input with added white noise.
- Four odd harmonics added to the signal to simulate the real data behaviour.
- A step function added to $R(t)$ signal to represent a step change due to expulsion while welding.
- A 120Hz ripple added to the resistance $R(t)$ signal to represent the effect of heating in welding process.

Case 1: Pure Sinusoidal Input Signals

The pure sinusoid was applied to Simulink model of the resistance spot welder and the calculated I and V_m were applied as the input signals to the estimation system to estimate the actual tip voltage magnitude $|V_a|$ and the dynamic resistance $R(t)$. The secondary voltage $V(t)$, which was used to generate I and V_m, is based on its calculated value from the real data as given below

$$v(t) = 4.12\sin(2\pi 60t) \tag{4.18}$$

Since the input signals to the estimation system are pure sinusoids, only one internal model is used for each independent input. The design parameters for the second order bandpass filter with a notch are given as: $BW = 2\pi 160$, $\omega_0 = 2\pi 80$ and $\varepsilon =$

Table 4.1: Tuning values for a bandpass filter with a notch

$L(s)$	K_1	K_2
$\frac{1.114\times10^6 s^2}{s^4+1669s^3+2.244\times10^6 s^2+5.328\times10^8 s+6.384\times10^{10}}$	164.2191	521.8538

Table 4.2: Tuning values for a bandpass filter with a notch and a added zero term

$L(s)$	K_p	K_1	K_2
$\frac{1.114\times10^6 s^2}{s^3+1251s^2+9.091\times10^5 s+1.527\times10^8}$	0.23509	0.83726	0.49313

0.75. The values of the tuning function $L(s)$ and the state feedback gains K_1 and K_2 in the estimation system can be solved by (C.8) as given in Table 4.1. The initial conditions for the current and voltage were obtained from (4.15) and (4.16), and are given as: $(x_1(0) = -21.462,\ x_2(0) = -9.8111)$ and $(x_{1v}(0) = -0.0033,\ x_{2v}(0) = 0.003)$, respectively. The estimates of the dynamic resistance and the tip voltage magnitude are shown in Fig. 4.7. It clearly shows that the dynamic resistance estimate converges to its known value with some time delay, and the actual tip voltage magnitude tracks its known peak values, but the transient responses prevents accurate measurement of the resistance for greater than one full cycle.

To further reduce the transient responses, a zero term was added in the estimation system as shown in Fig. 3.2 with $\sigma = \frac{R(0)+R_c}{L}$. The design parameters for the bandpass filter and the notch remain the same. The values of $L(s)$, K_p, K_1 and K_2 can be solved by matching the coefficients in (C.11) and (C.12), and are given in Table 4.2. The corresponding initial conditions for IMs are $(x_1(0) = -12674,\ x_2(0) = 3988.2)$ and $(x_{1v}(0) = -0.26476,\ x_{2v}(0) = 2.5144)$ for the inputs of current and voltage, respectively. The initial conditions for the integrators of current and voltage are $8.6444kA$ and $-1.0183V$, respectively. The

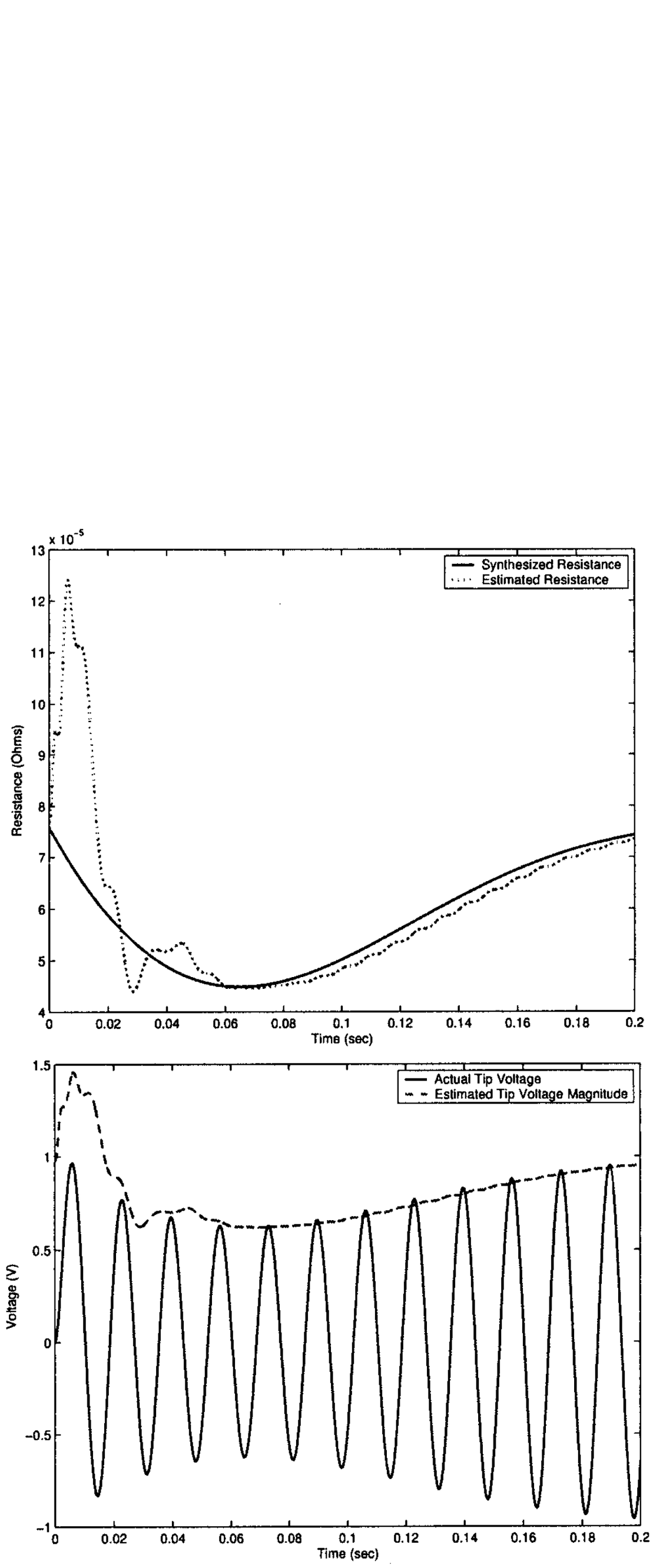

Figure 4.7: Estimates of dynamic resistance (above) and actual tip voltage magnitude (bottom) for a pure sinusoid input

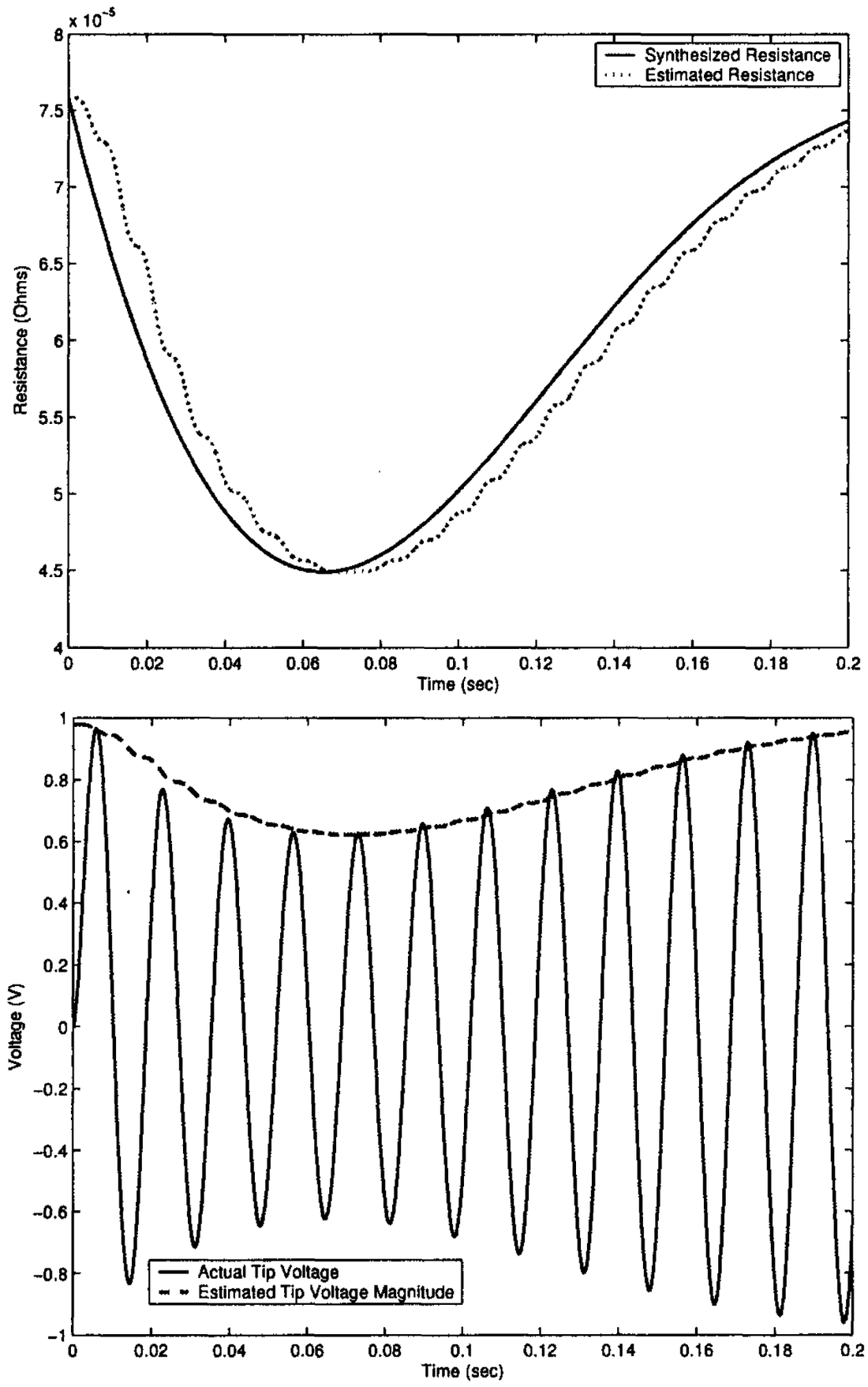

Figure 4.8: Estimates of dynamic resistance (above) and actual tip voltage magnitude (bottom) for a pure sinusoid input with zero term compensation

corresponding estimates of the dynamic resistance and the tip voltage magnitude are shown in Fig. 4.8. From the figure, we can see that with the zero term compensation, the transient responses are significantly reduced, the estimated resistance matches the known value with time delay less than $10ms$, and the estimated tip voltage magnitude tracks its known peak precisely.

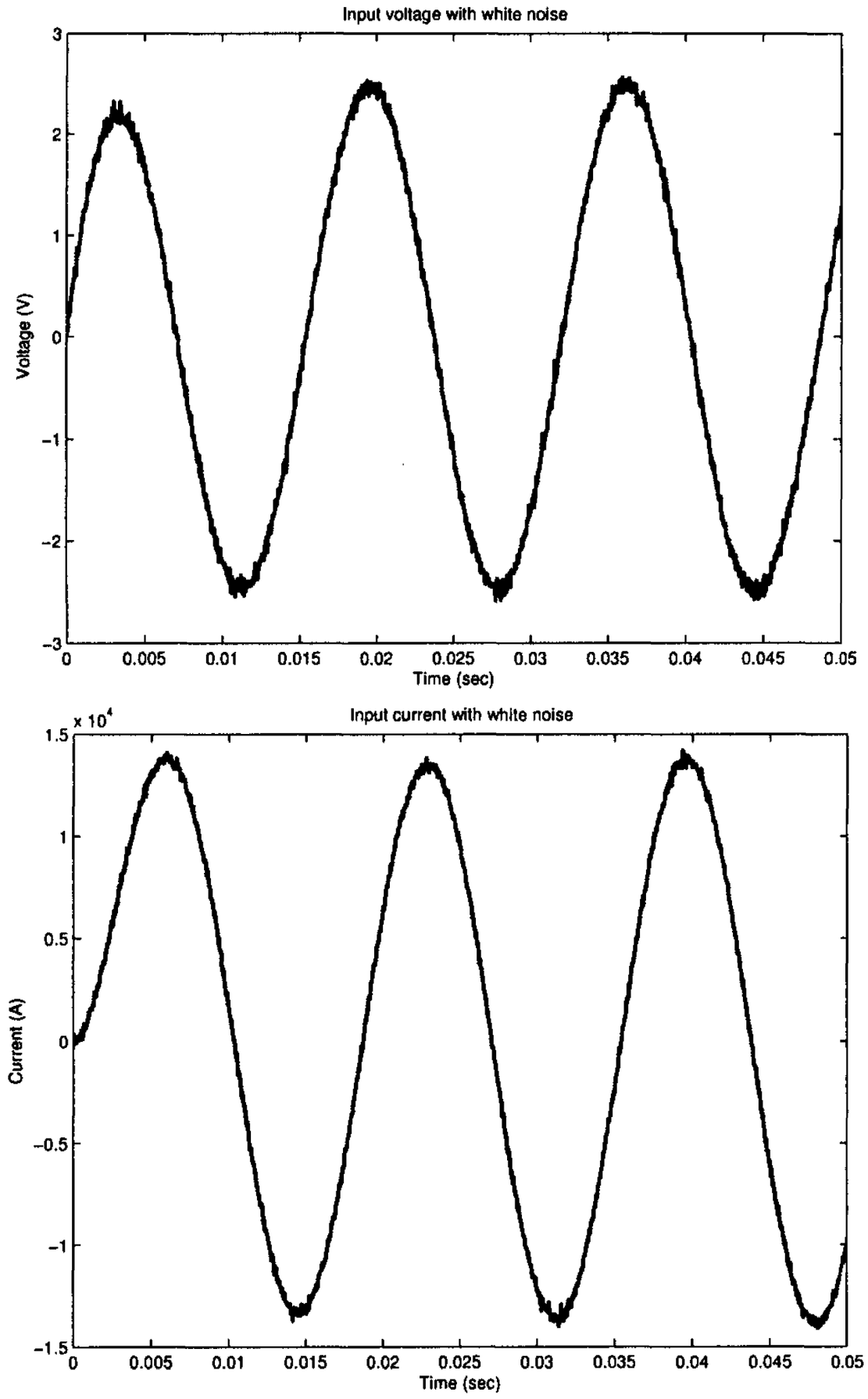

Figure 4.9: Measured tip voltage (above) and current (bottom) corrupted with white noise

Case 2: Input with Measurement Noise

To test the noise rejection performance of the algorithm, a low magnitude band limited white noise with a power spectral density (PSD) of 0.000001 was added to the measured tip voltage signal, while white noise with PSD of 1 was added to the measured current signal. This is equivalent to variation of 5% of the peak values of the measured signals. The corresponding measured tip voltage and current with the added measurement noises are shown in Fig. 4.9.

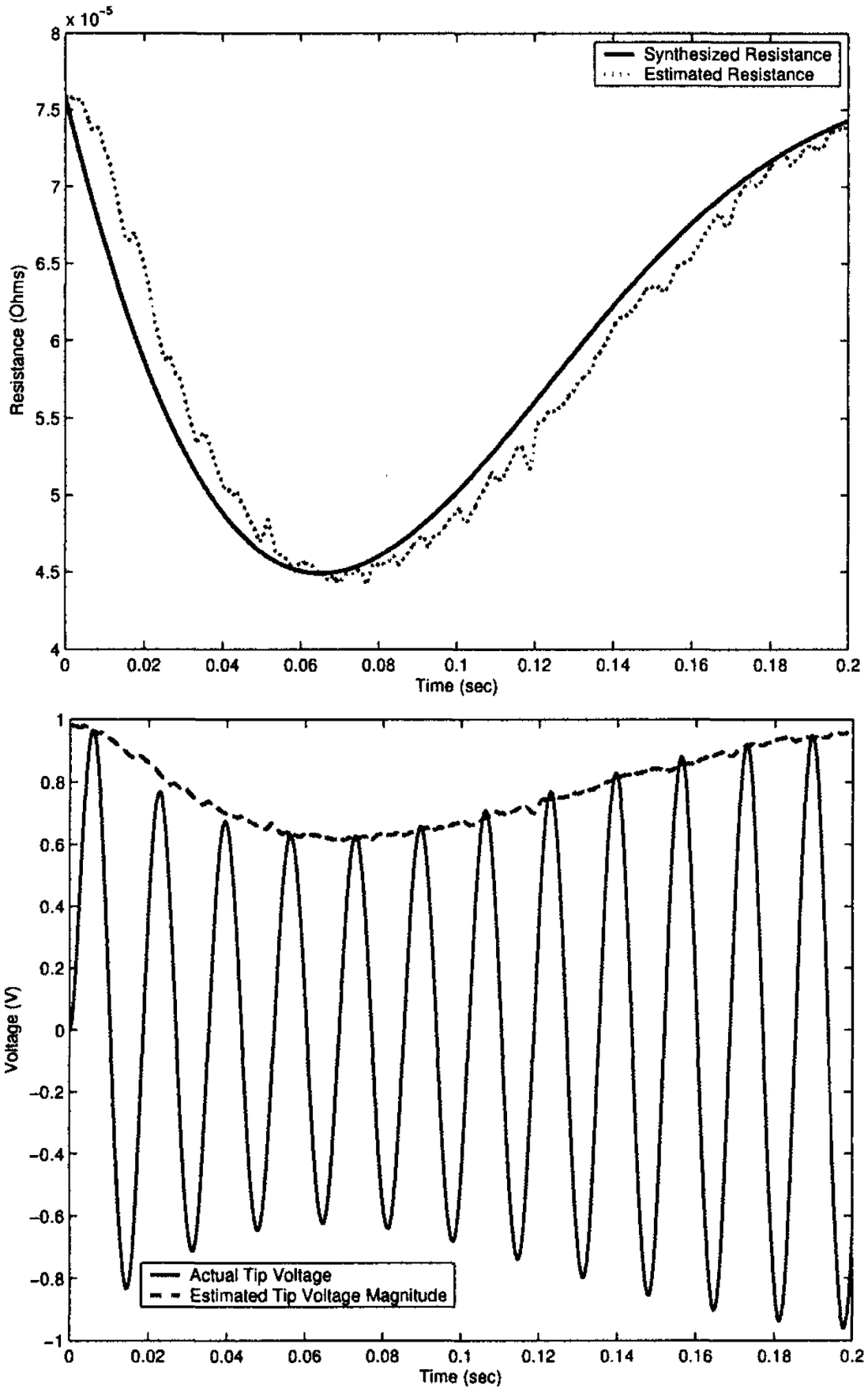

Figure 4.10: Estimates of dynamic resistance (above) and actual tip voltage magnitude (bottom) for input signals with white noise

The estimated dynamic resistance and tip voltage magnitude are shown in Fig. 4.10.

All the design parameters for the bandpass filter and the notch and the initial conditions for current and voltage decomposition routines remain same as the pure sinusoidal input case with the zero compensation. It can be seen from the results that the estimated resistance and the magnitude of tip voltage have very good tracking performance to their respective known values, with much less than 5% variation. The present algorithm has very high ability to reject noise.

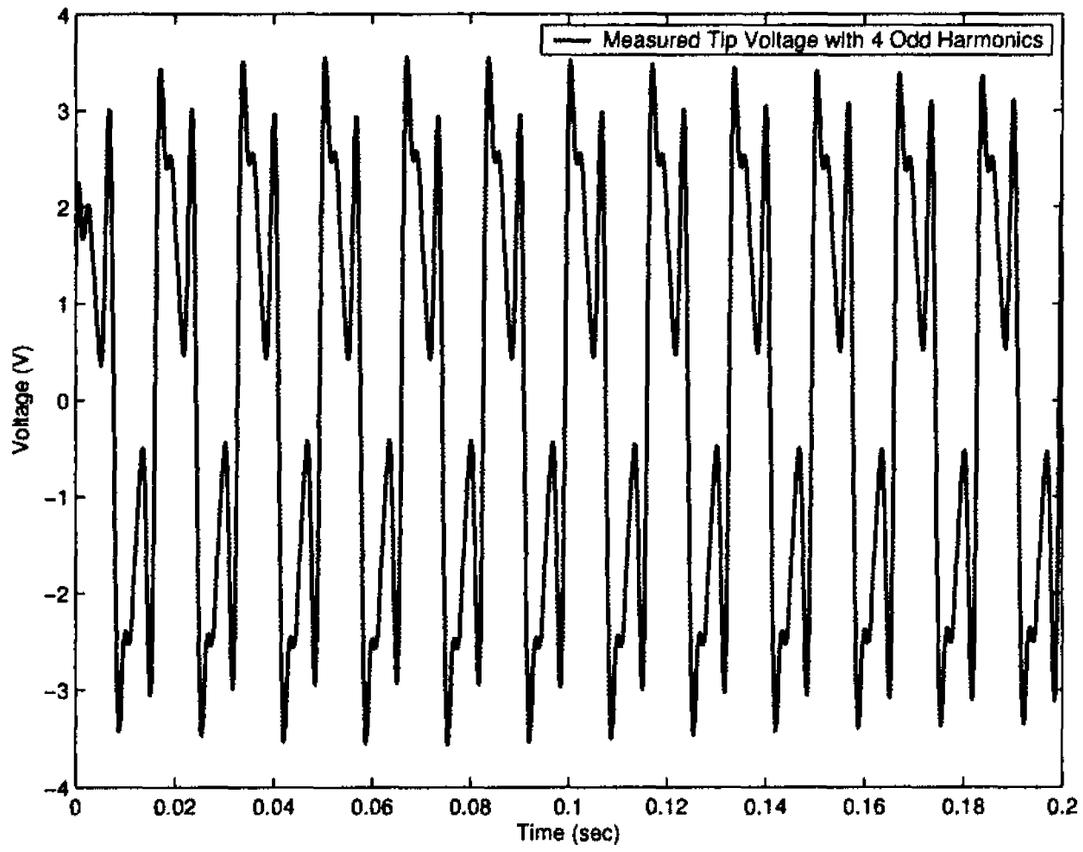

Figure 4.11: Measured tip voltage with 4 odd harmonics

Case 3: Input with Four Odd Harmonics

When the input secondary voltage signal contains harmonics, multiple IMs are incorporated in the estimation system to detect the fundamental component and each of the harmonics. The magnitudes and initial phases of the harmonics present in (4.19) are selected based on the best available estimates of the first four harmonics present in real weld data acquired from a welding machine. The number of the IMs should be identical to the number of the harmonics present in the input signal, in this case 4. The input secondary voltage signal is given by

$$\begin{aligned} v(t) &= 4.125\sin(2\pi 60t) + 1.887\sin(2\pi 180t - 0.0556) \\ &\quad + 1.2722\sin(2\pi 300t + 1.1403) + 0.4538\sin(2\pi 420t + 1.6834) \end{aligned} \tag{4.19}$$

The measured tip voltage generated by this secondary voltage is plotted in Fig. 4.11. It still does not reflect the real data as the real data is composed of lots of significant harmonics.

Table 4.3: State feedback gains and the initial conditions for current and voltage for 4 IMs

	K_{1i}	K_{2i}	x_{1i}	x_{2i}	x_{1iv}	x_{2iv}
1^{st}	0.16504	-2.3063	3869.6	4025.1	0.99592	−0.37024
2^{nd}	0.38589	0.016238	−6662.4	2566.5	0.83875	3.6831
3^{rd}	0.47363	0.11731	−1045.7	2137.4	1.7861	1.0746
4^{th}	0.42723	-0.13905	367.51	555.58	0.70666	−0.40689

The desired estimation system behaves as a bandpass filter with four notches and an added zero term. The design parameters for the second order bandpass filter with four notches are given as: $BW = 2\pi 600$, $\omega_0 = 2\pi 300$, $\varepsilon_1 = 0.35$ and $\varepsilon_2 = \varepsilon_3 = \varepsilon_4 = 0.2$. The transfer function of $L(s)$ and the value of K_p solved from (C.11) and (C.12) are given as: $L(s) = \frac{1.567\times10^7 s^2}{s^3+6246s^2+4.068\times10^7 s+3.019\times10^{10}}$, and $K_p = 1.8104$, respectively. Meanwhile, (C.12) gives the solutions of the state feedback gains (K_{1i}, K_{2i}) $(i = 1,2,\cdots,4)$ as well. The initial conditions of the current and voltage for each IM incorporated in the system are calculated separately by (4.15) and (4.16). Table 4.3 gives all the solutions of the state feedback gains and the initial conditions for the four IMs incorporated in the feedback loop of the estimation system. The initial conditions for the integrators of current and voltage of the zero term compensation are $11.339kA$ and $-2.7322V$, respectively.

The algorithm provides four estimates of the resistance and tip voltage magnitude corresponding to the harmonics present in the signals. The overall tip voltage magnitude is calculated by taking the RMS of the all estimates of the tip voltage magnitudes from the system. Fig. 4.12 shows the estimated dynamic resistance from 1^{st} pair of the internal models and the estimated tip voltage magnitude. The estimate of the tip voltage magnitude is compared with its theoretical value generated by the combined input sources. It can be

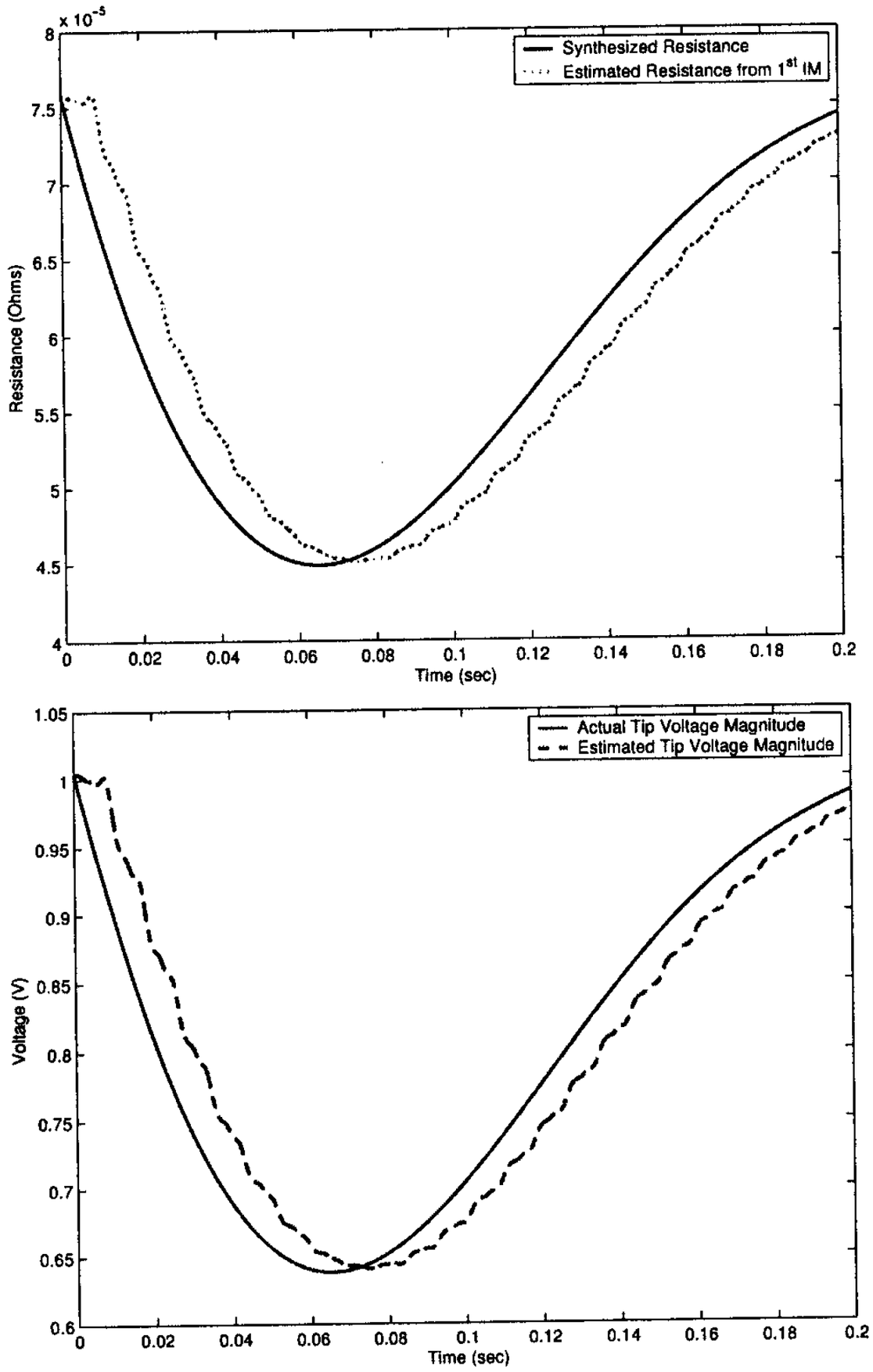

Figure 4.12: Estimates of dynamic resistance (above) and actual tip voltage (bottom) for a input with four odd harmonics

seen from the figures that the resistance and the tip voltage magnitude track nicely to their respective known theoretical values with time delay of $10ms$.

Case 4: Input with Four Odd Harmonics and a Step Change for Expulsion

A significant variation in the welding process that can occur is when the forces generated by the expanding metal exceed the force applied by the electrodes. When this occurs, the liquid metal shoots out between the work pieces. For galvanized steel, this can damage the finish, and for all materials, this loss of material can significant weaken the weld. This phenomenon is called expulsion. It is believed that there is a step change in the resistance when expulsion occurs. To demonstrate that the present algorithm can detect the change, a step function was added to the resistance when the secondary voltage signal contains four odd harmonics. The step function used to represent the expulsion effect occurs at $0.1s$ and is given by

$$H(t) = \begin{cases} 0 & t \leq 0.1s \\ -10^{-5} & t > 0.1s \end{cases} \tag{4.20}$$

The secondary voltage with four odd harmonics remains the same as the case stated earlier. All the other design parameters, such as parameters for the bandpass filter and the notches, transfer function of $L(s)$, state feedback gain K, and the initial conditions for each IM and integrators, remain the same as the case of input with four odd harmonics presented previously. The estimates of the dynamic resistance and the tip voltage magnitude demonstrate a step change due to expulsion are shown in Fig. 4.13. It is clearly shown in the figures that the estimated dynamic resistance and the tip voltage magnitude have detected the step change that represents the expulsion during the welding process with $10ms$ of time delay, as compared to their respective known values.

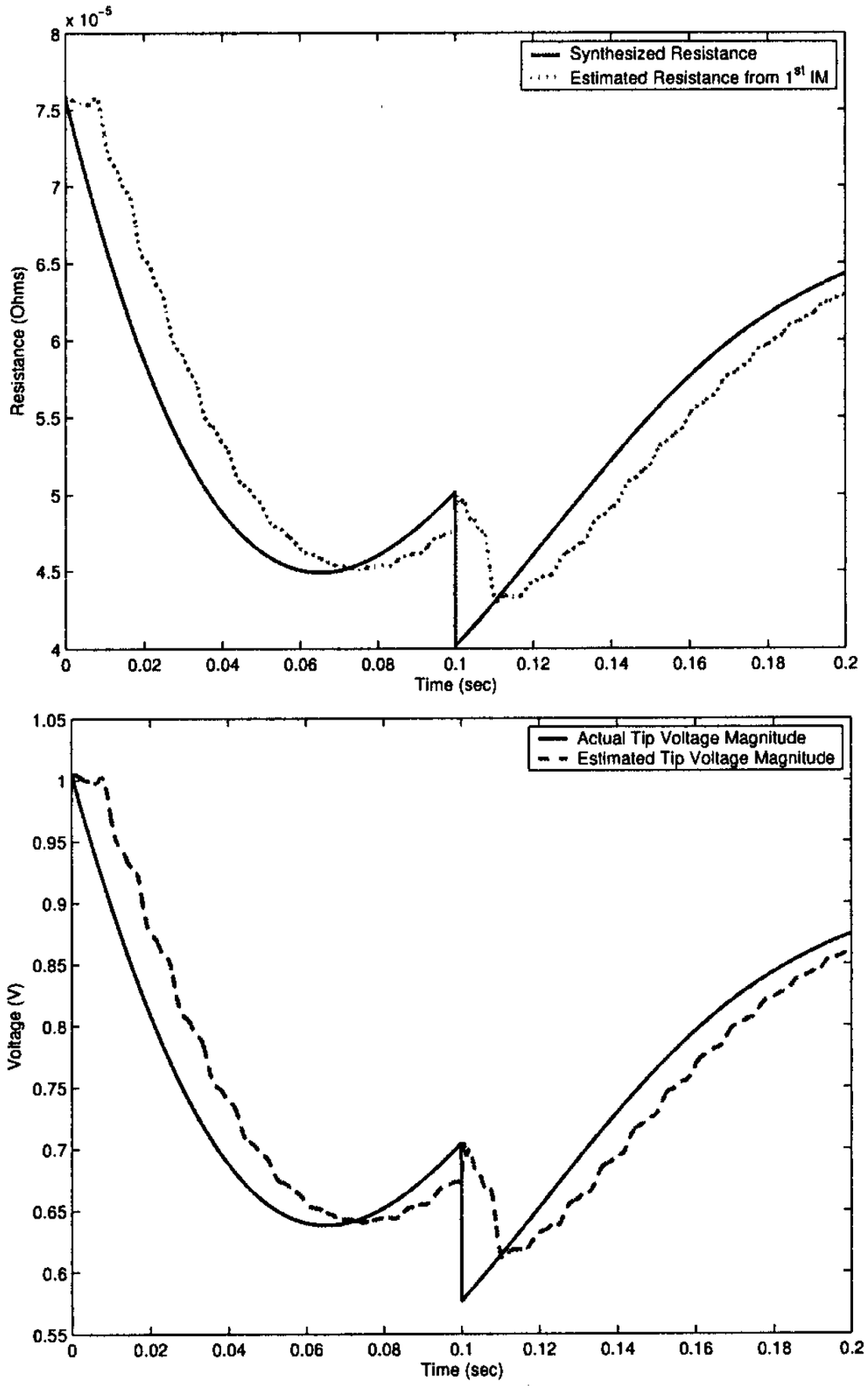

Figure 4.13: Estimates of dynamic resistance (above) and actual tip voltage magnitude (bottom) for a input with four odd harmonics and a step change for expulsion

Table 4.4: Values of $L(s)$, K_p, K_{11},K_{21}, K_{12} and K_{22}

$L(s)$	K_p	K_{11}	K_{21}	K_{12}	K_{22}
$\frac{5.641\times10^6 s^2}{s^3+3422s^2+1.9\times10^7 s+3.912\times10^9}$	0.13604	1.0585	-1.4635	0.65957	-0.16112

Case 5: Input with 3^{rd} Harmonic and $120Hz$ Ripple

To investigate the algorithm's ability to detect the effect of heating in the welding process, a low magnitude $3\mu\Omega$, $120Hz$ ripple is added to the dynamic resistance signal. In this case, the input secondary voltage signal used to generate the measured tip voltage and current signals contains 3^{rd} harmonic, which is given by

$$v(t) = 4.125\sin(2\pi 60t + 1.1636) + 1.887\sin(2\pi 180t - 0.3516) \tag{4.21}$$

Two internal models are incorporated in the estimation system to detect the fundamental component and 3^{rd} harmonic, respectively. The desired estimation system behaves as a bandpass filter with two notches. The design parameters for the second order bandpass filter with two notches are given as: $BW = 2\pi 360$, $\omega_0 = 2\pi 180$, $\varepsilon_1 = 0.9$ and $\varepsilon_2 = 0.3$. The values of $L(s)$, K_p for the zero term, and the state feedback gains $(K_{1i}, K_{2i})(\ i = 1,2)$ in the estimation system are given in Table 4.4. The initial conditions for the current and voltage are given in Table 4.5. The initial conditions for the integrators of current and voltage are $-2.6237kA$ and $0.30906V$, respectively.

The algorithm provides two estimates of the resistance and tip voltage magnitude corresponding to the harmonics present in the signal. The above figure in Fig. 4.14 shows the estimated dynamic resistances from 1^{st} and 2^{nd} pairs of the IMs. Fig. 4.14 shows that

Table 4.5: Initial conditions for current and voltage for 2 IMs

	x_{1i}	x_{2i}	x_{1iv}	x_{2iv}
1^{st}	7010.6	1393.8	0.77478	-1.118
2^{nd}	-3942.9	973.89	0.21101	2.1384

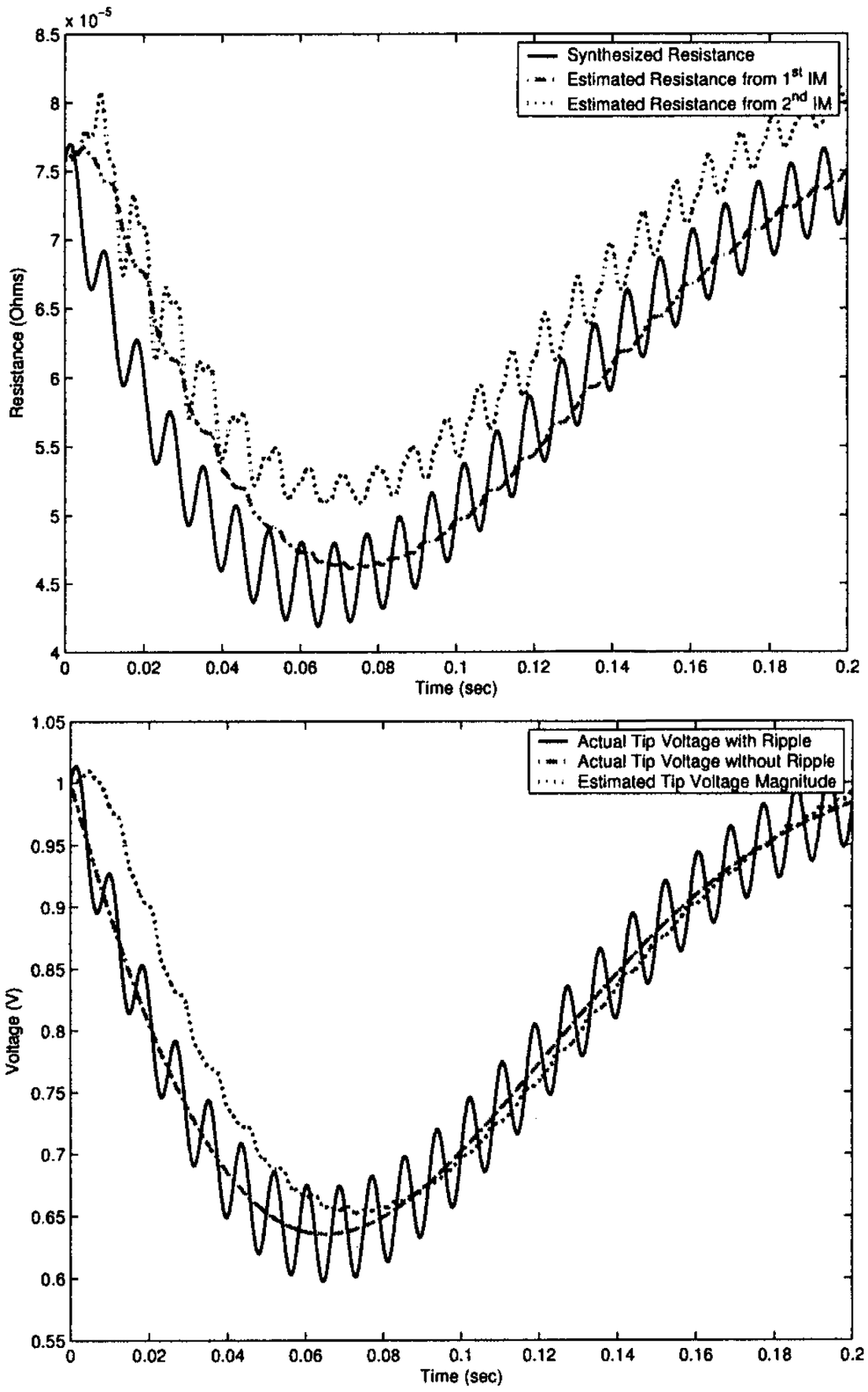

Figure 4.14: Estimated dynamic resistance from 1^{st} and 2^{nd} IM (above) and estimated tip voltage magnitude (bottom) for a input with 3^{rd} harmonic and $120Hz$ ripple

the estimate from the 1^{st} IM gives good low frequency component, however, the estimate from the 2^{nd} IM gives better result demonstrating the $120Hz$ component, but it has greater bias. To extract the most useful information from the two estimates, it is necessary to take these two estimates into account to find a equivalent resistance, i.e., a frequency weighted value of the two estimates. The bottom figure in Fig. 4.14 shows the estimated tip voltage magnitude comparing to the known values with ripple added in and without ripple. It is clearly shown that the estimated tip voltage magnitude is closer to the known value without ripple added in the known resistance. This shows that the present algorithm does not tell much information about ripple from the estimated tip voltage magnitude, on the other hand, it shows that the algorithm has a very good ability to reject noise.

4.5.1.4 Simulation Results for Synthesized Input Created by SCR Model

Though DC power controlled spot welding is commercially available, most of the spot welding processes generate AC power. The AC power supplies for the spot welding are primarily SCR source. The input current is usually controlled by holding the conduction angle constant or by adjusting it to hold measured current constant [5]. A model created in the SIMULINK environment tries to generate the chopped voltage and current signals that are as close to the ones generated by SCR controlled power supplies in practice as possible. Fig. 4.15 shows the current and voltage signals generated by the model. The duty cycle remained fixed at 80%.

It can be seen from Fig. 4.15 that the chopped waveforms of current and voltage created by SCR controlled model are zero for significant amount of time during the crossovers, and contain infinite odd harmonics. General speaking, for identifying infinite harmonics,

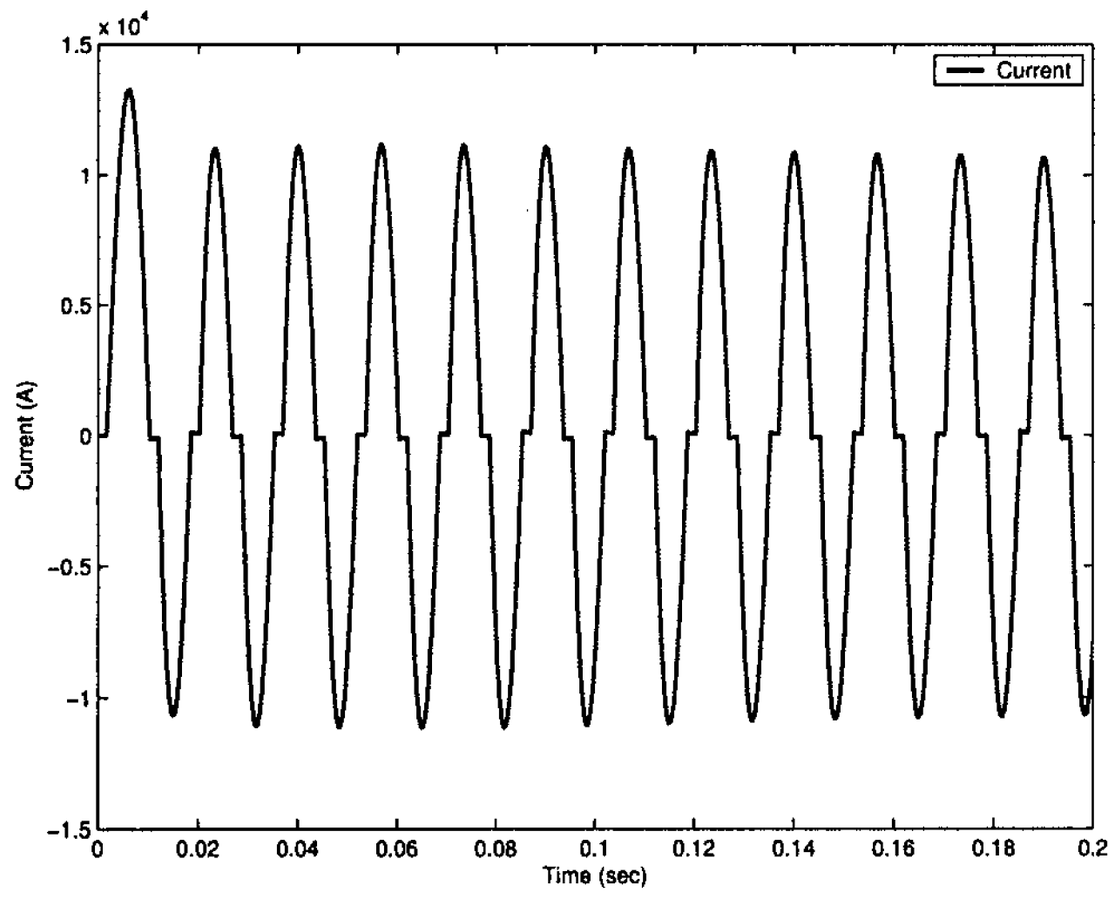

Figure 4.15: Input current (above) and voltage (bottom) generated from SCR controlled model

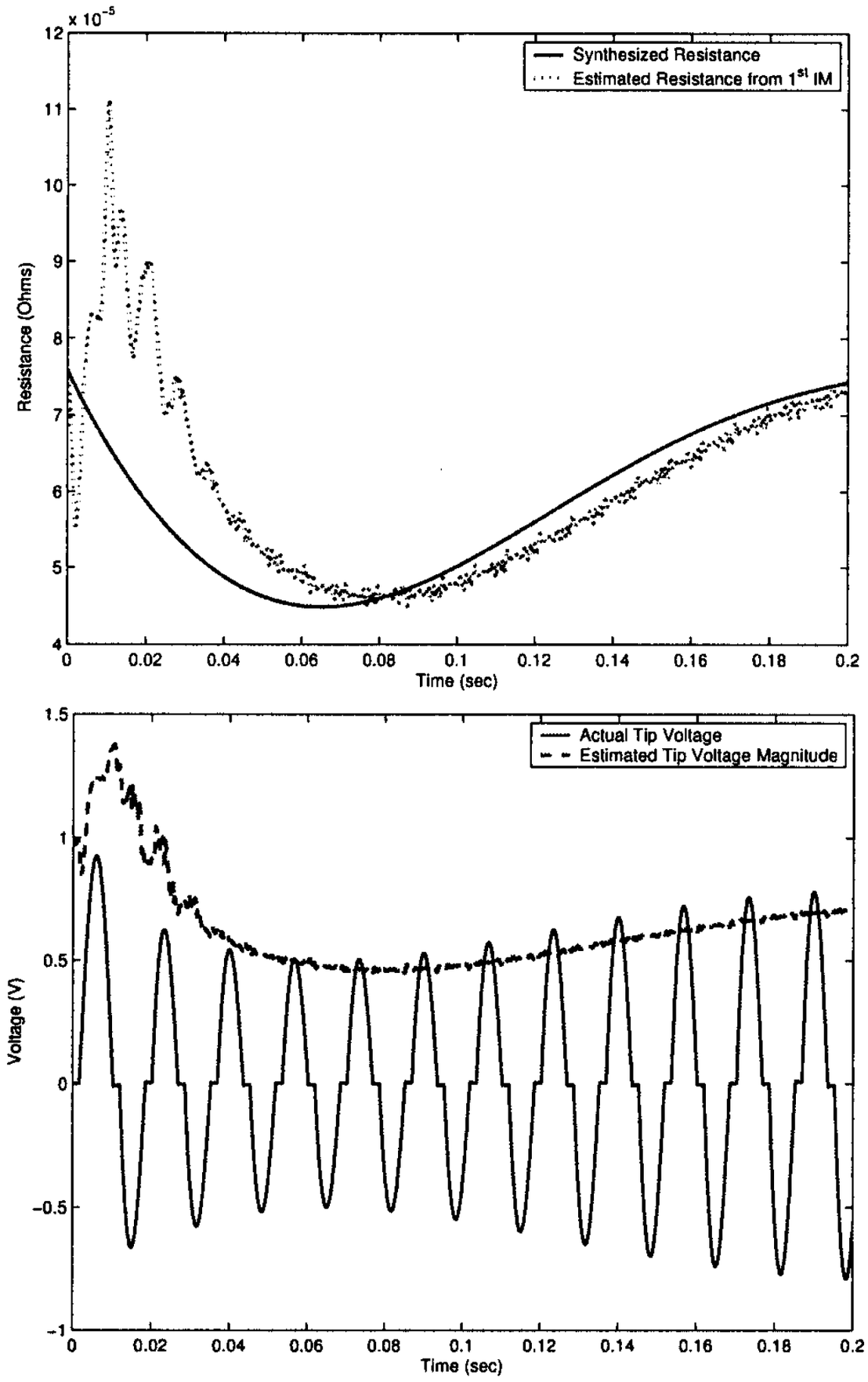

Figure 4.16: Estimated dynamic resistance from 1^{st} IM (above) and estimated tip voltage magnitude (bottom) for SCR controlled input sources

the more IMs that are incorporated in the estimation system, the better the performance will be. Since the power spectral energy of the higher order harmonics contained in the signals is usually significantly decreased after certain orders, only finite IMs are necessarily incorporated in the system. In this case, four IMs are applied to identify the fundamental component ($60Hz$) and its first three odd harmonics. Fig. 4.16 shows the estimated results of the dynamic resistance and the actual tip voltage magnitude. It can be seen from the figures that the estimated results have transient responses with big overshoots. It takes a

Table 4.6: State feedback gains and the initial conditions for current and voltage for 4 IMs

	K_{1i}	K_{2i}	x_{1i}	x_{2i}	x_{1iv}	x_{2iv}
1^{st}	388.21	−55.485	−18.362	27.324	0.0033771	0.0052765
2^{nd}	−155.25	486.23	0	10^{-12}	0	10^{-12}
3^{rd}	−517.25	686.58	0	10^{-12}	0	10^{-12}
4^{th}	−632.03	1032.8	0	10^{-12}	0	10^{-12}

certain amount of time for these two signals to reach their steady state values. Besides, the initial conditions for each of the four pairs of IMs affect the transient responses as well. Since it is not feasible to get the magnitude of each harmonic contained in the input signals, the reasonable initial conditions for each IM used to identify the odd harmonics were chosen as 0, only the initial conditions for the 1^{st} pair of IM that is used to identify the fundamental component are available to be obtained by solving (4.15) and (4.16) once the design parameters for the system are determined. The design parameters for the second order bandpass filter and four notches are given as: $BW = 2\pi 360$, $w_0 = 2\pi 180$, $\varepsilon_1 = 0.35$, $\varepsilon_2 = \varepsilon_3 = \varepsilon_4 = 0.2$. $L(s) = \frac{5.641\times10^6 s^2}{s^4+5009s^3+1.668\times10^7 s^2+7.388\times10^9 s+1.636\times10^{12}}$. The state feedback gains and initial conditions for each pair of the IM are listed in Table 4.6. Note that, in practice, the initial conditions of x_{2i} and x_{2iv}, where $i = 2,3,4$, were chosen as a very small positive constant (10^{-12}) rather than 0 to avoid the issue of calculating $0/0$ at $t = 0$.

To better understand how well the algorithm works for this case, the estimated dynamic resistance and the tip voltage magnitude shown in Fig. 4.16 are redrawn by taking the time delay into consideration. Fig. 4.17 shows the plots after shifting the 300 points to the left. This is equivalent to $12ms$ of time delay which is very close to that of the previous cases presented in subsection 4.5.1.3. Fig. 4.18 shows the estimated result closely matches

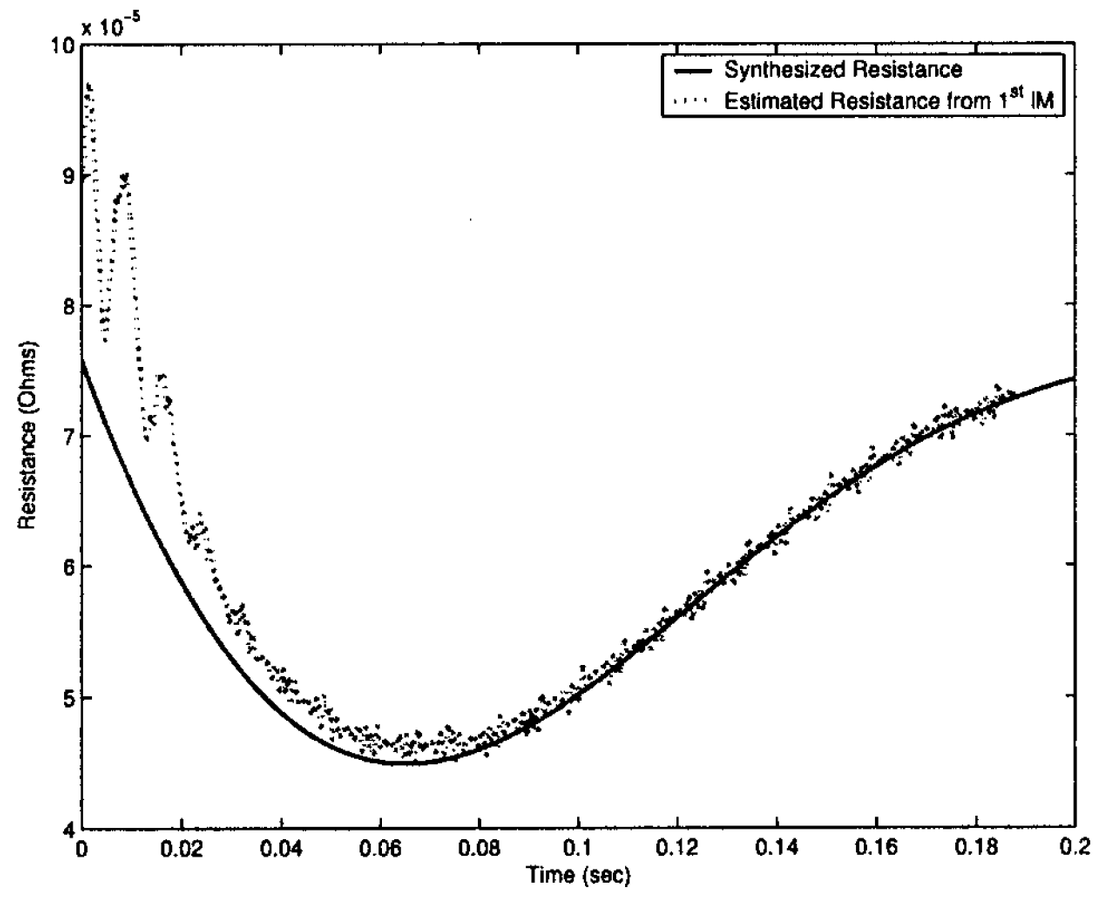

Figure 4.17: Estimated dynamic resistance (above) and tip voltage magnitude (bottom) after 300 points shifting for SCR controlled input sources

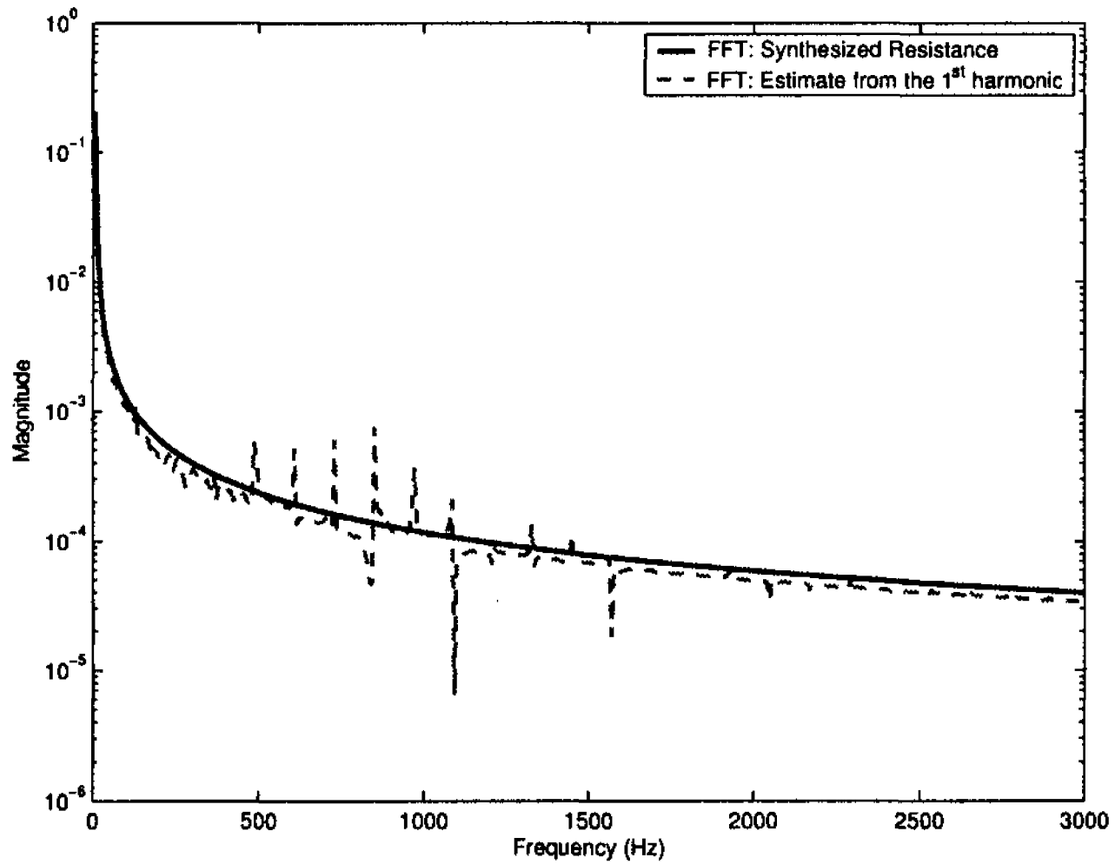

Figure 4.18: The magnitude of the Fourier transform of the synthesized known resistance and the estimate from the 1^{st} IM

the actual resistance in the frequency domain except at the odd harmonic of $60Hz$ beginning with the 9^{th}. This is not surprising because these are the frequencies that were chosen not to be modelled.

4.5.2 Results for Experimental Weld Data

In this subsection, the present algorithm is applied to the experimental data collected from the welding machines located at The University of Waterloo. The data acquisition system is described in detail in [5]. Fig. 4.19 shows the acquired current and voltage data that were applied to the algorithm for the estimation of the dynamic resistance and tip voltage magnitude. Fig. 4.20 gives the corresponding estimates when four IMs are applied to the estimation system with the same parameters stated in **Case 5**. For comparison purposes, Fig. 4.21 displays our estimated resistance with the resistance calculated by V/I at the peak currents and the state of the art measurement achieved by subtracting a scaled version of the derivative of the current. The state of the art measurement appears to have variations

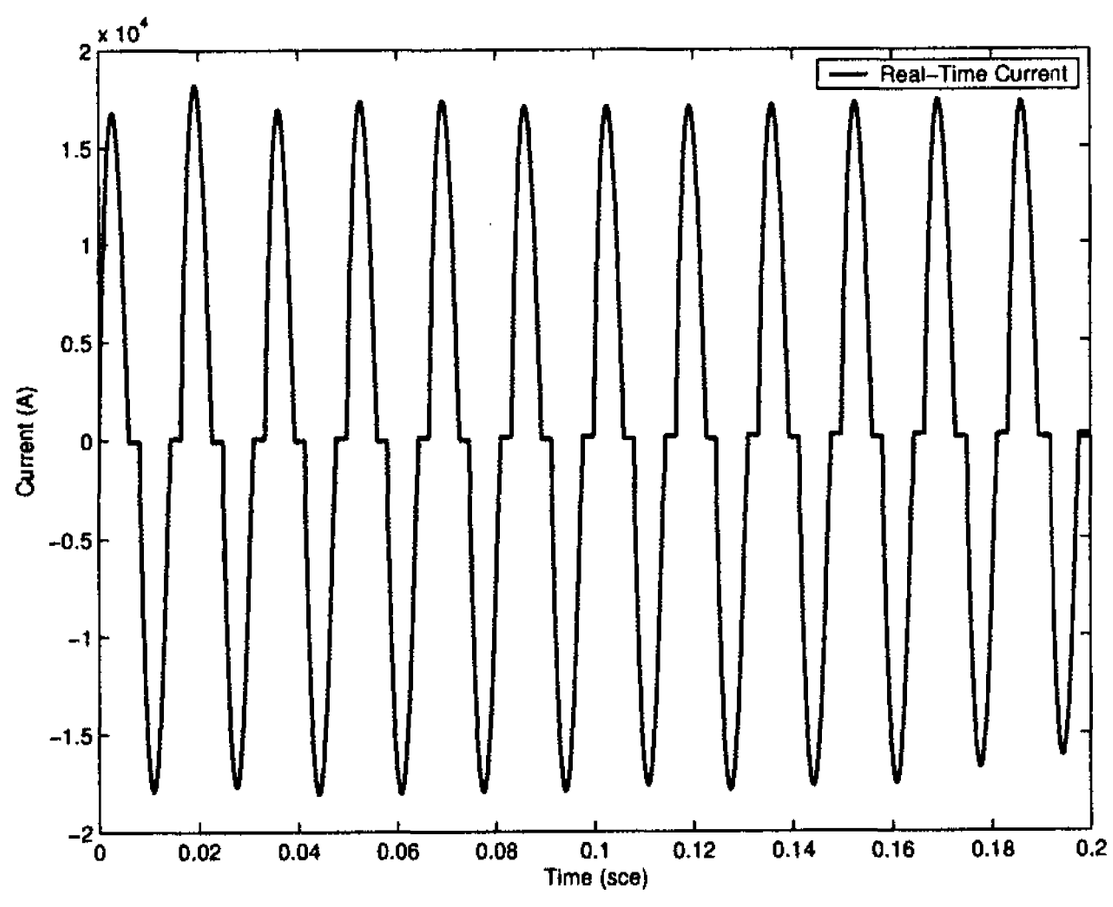

Figure 4.19: The acquired current (above) and voltage (bottom) data as the inputs of the algorithm

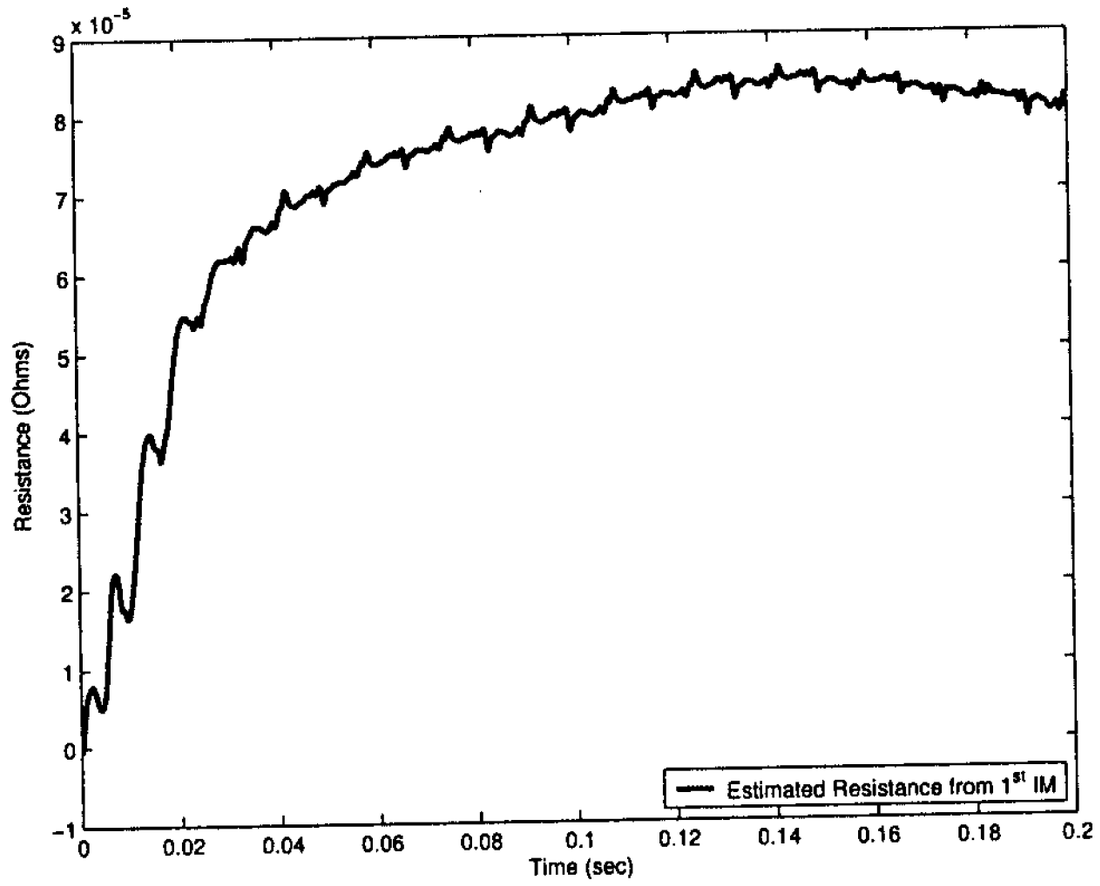

Figure 4.20: Estimated dynamic resistance (above) and tip voltage magnitude (bottom) from the shop floor data

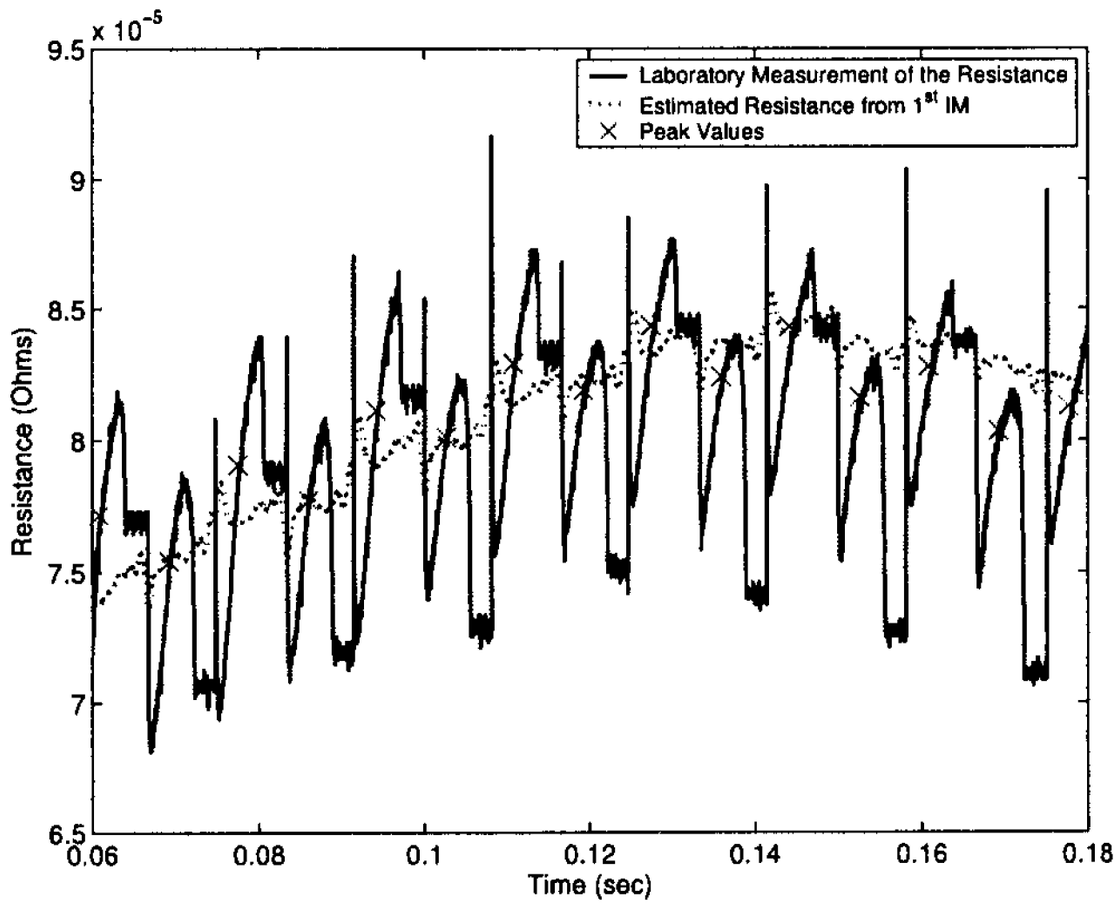

Figure 4.21: Estimated dynamic resistance and laboratory measurement of the resistance

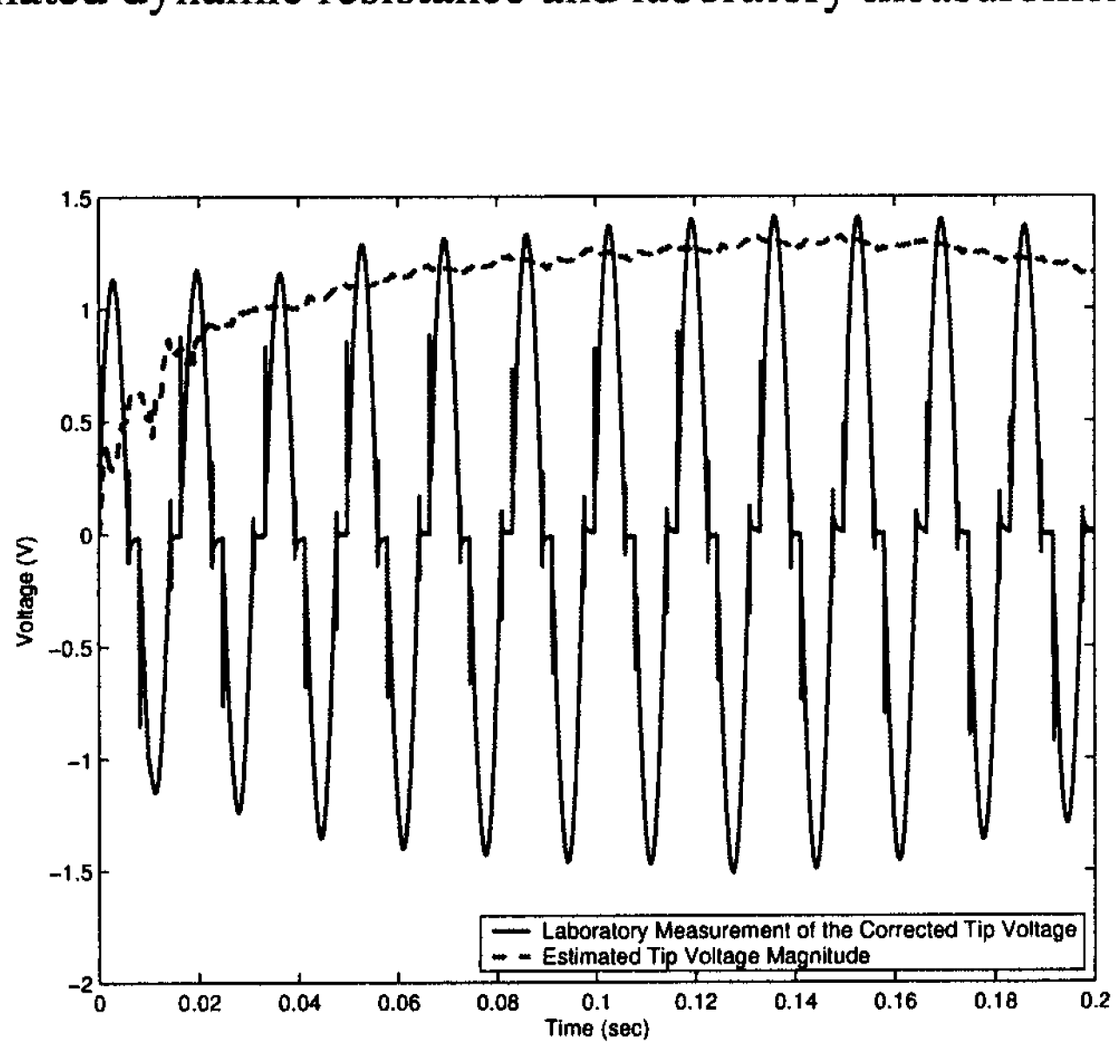

Figure 4.22: Estimated tip voltage magnitude and laboratory measurement of the corrected tip voltage

that are not consistent with the physics of the problem. Since energy is input into the system with a 120Hz fundamental frequency, and resistance increases with temperature, some 120Hz variance in the resistance is to be expected. However, the fluctuation seen here is greater than expected and the resistance is sometimes seen to be increasing when power is zero and decreasing at periods of high instantaneous power. Thus the laboratory measurement of the dynamic resistance is not acceptable. Fig. 4.22 compares the proposed algorithms estimate of the root mean square voltage times the square root of two with the voltage achieved by subtracting the scaled version of the current derivative from the measured voltage. We do not know what the exact resistance and tip voltage look like. We believe that the proposed algorithm provides better and more reasonable measurement of the resistance, and the estimated tip voltage magnitude tracks the peak value of the corrected tip voltage as shown in Fig. 4.22 .

4.6 Conclusion

In this chapter, an internal model based instantaneous Fourier decomposition algorithm has been applied to a real time resistance spot welding process. The algorithm can not only identify the input signals, eliminate the induced noise from the measured inputs, but also decompose a multi-tone signal into single-tone signals, in other words, Fourier Series representation, thereby providing estimates of the time varying resistance and the tip voltage magnitude. Simulations using computer generated data show that the algorithm is reliable and can be applied to the real data. Also, the algorithm can detect resistance variations, such as expulsion and heating occurring in the welding process.

Chapter 5

Conclusions and Future Work

Two applications of the internal model based estimation algorithm have been presented. Modifications to the basic algorithm are appropriately made to achieve the desired performances for different systems: active noise control and spot welding monitoring. Design methods of the improved algorithms are presented. Simulations are conducted under Mathworks SIMULINK environment for algorithm validation.

5.1 Conclusions

Application on an acoustic duct is firstly presented. A design method which is equivalent to placing an adaptive PD controller in series with the original internal model in the feedback loop is proposed. The improvement of the basic algorithm is made to increase the stable frequency band for a widely phase varying system by adaptively tuning the two control gains with the estimated frequency. Simulations have been conducted on both independent sinusoidal signals and a chirp signal corrupted with Gaussian white noise. Excellent results are obtained on both increasing the working frequency band and decreasing the worst case error with minimum loss of speed for the system which previously was stable only for a very narrow band of disturbance frequency.

The modification to the basic algorithm to decompose a multi-tone signal into single-tone signals, generating a instantaneous Fourier series representation is presented next. The coefficients of the Fourier series represent the magnitude of the measured signal. The improved algorithm is then applied to real time dynamic resistance estimation in resistance spot welding process. The time varying dynamic resistance is calculated by the division of the magnitude of voltage and the magnitude of current. The induced voltage noise is eliminated by projecting the measured tip voltage on current. The transfer function of the tuning function and the state feedback gains are determined by the design of the overall estimation system as a bandpass filter with notches. The initial conditions for each internal model incorporated in the system and the initial values for integrators where applicable are given. Simulations on synthesized data of pure sinusoidal input, input with finite harmonics, and input with infinite harmonics are conducted under Mathworks SIMULINK environment. Results show that the improved algorithm provides fairly accurate estimation of the dynamic resistance and tip voltage magnitude with ability to detect expulsion and heating during welding process without any calibration. It is efficient and practical. Analysis on real data shows that the algorithm is more reliable and achievable than any other existing approaches and makes application of the previous academic literature to shop floor more likely to succeed.

5.2 Future Work

Though the modified methods have achieved excellent performance on each individual system, more work is still needed to be done, particularly on RSW process. Issues that

need to be further investigated in the future are as follows:

- The algorithm can clearly demonstrate whether there is an occurrence of expulsion during the welding process from the estimated dynamic resistance. However, it does not contain much information about $120Hz$ variation from the estimate of the 1^{st} IM. Though estimate of the dynamic resistance from each IM is of the same physical property, the results show that the 1^{st} IM gives better low frequency behavior, the higher order IMs provide more information of behaviour of the even harmonics, but they are noisy and biased. Finding suitable techniques to combine all available resistance estimates is the biggest issue in the future.

- Increasing the number of IMs should enable us to more accurately model the signal. However, this also increases the order of the bandpass filter, which can degrade the convergence speed of our states to their steady state trajectories. In practice, the present simulations with their tuning parameters show that the best results occur with four IMs. Investigation of the best parameters for the closed loop bandpass filter is needed. Faster convergence, so as to enable tracking of resistance during the first half cycle, as well as improving the ability to track $120Hz$ variation may call for raising the lower cutoff frequency of the bandpass filter, and placing its poles as far into the left half plane as possible.

- Estimation performance is significantly affected by the initial conditions of each IM. The closer the initial conditions to their ideal values, the better the performance is. When the input contains uncertain components where the corresponding initial conditions are impossible to be obtained, it takes time for the estimation system to

respond. Work on initialization for infinite harmonic case is another issue to be addressed in the future.

BIBLIOGRAPHY

[1] L. J. Brown and Q. Zhang, "Identification of periodic signal with unknown frequency," *IEEE Transactions on Signal Processing*, vol. 51, no. 6, pp. 1–9, June 2003. 1, 3, 14

[2] Z. Zhao and L. J. Brown, "Musical pitch tracking using internal model control based frequency cancellation," in *Proceedings of the 42nd IEEE Conference on Decision and Control*, vol. 5, Dec. 9–12, 2003, pp. 5544–5548. 1

[3] ——, "Fast estimation of power system frequency using adaptive internal-model control technique," in *Proceedings of the 43rd IEEE Conference on Decision and Control*, vol. 1, Bahamas, Dec. 14–17, 2004, pp. 845–850. 1

[4] L. J. Brown and J. Lu, "Internal model based adaptive algorithm for noise cancellation," in *Twelfth International Congress on Sound and Vibration*, Lisbon, Portugal, July 2005. 1, 14, 16, 19, 21, 24

[5] N. Malhotra, "Online tip voltage and dynamic resistance measurement in RSW process," M. E.Sc. thesis, The University of Western Ontario, London, Ontario, Canada, 2005. 1, 2, 8, 31, 71, 76

[6] Q. Zhang, "Periodic disturbance cancellation with uncertain frequency," M. E.Sc. thesis, The University of Western Ontario, London, Ontario, Canada, 2001. 3, 5

[7] L. J. Brown and Q. Zhang, "Periodic disturbance cancellation with uncertainty frequency," *Automatica*, vol. 40, pp. 631–637, 2004. 3, 5, 14, 16

[8] B. A. Francis and W. M. Wonham, "The internal model principle of control theory," *Automatica*, vol. 12, pp. 457–465, 1976. 3, 14

[9] A. N. Akansu and R. A. Haddad, *Multiresolution Signal Decomposition*, 2nd ed. San Diego, CA: Academic Press, 2001. 5, 6

[10] P. Bremaud, *Mathematical principles of signal processing : Fourier and wavelet analysis*. New York, NY: Springer, 2002. 5

[11] R. S. Stankovic, C. Moraga, and J. Astola, *Fourier Analysis on Finite Groups with Applications in Signal Processing and System Design.* Publisher Piscataway, NJ; Hoboken, NJ: IEEE Press; Wiley-Interscience, 2005. 5

[12] L. Cohen, *Time Frequency Analysis.* Englewood Cliffs, NJ: Prentice Hall, 1995. 5

[13] Z. Leonowica, T. Lobos, and P. Schegner. (2002, June 24–28,) Modern spectral analysis of non-stationary signals in electrical power systems. 14th PSCC Conference. Sevilla. [Online]. Available: http://www.eeh.ee.ethz.ch/pscc02/papers/s28p03.pdf 6

[14] H. K. Kwok and D. J. Jones, "Improved instantaneous frequency estimation using an adaptive shot-time fourier transform," *IEEE Transactions on Signal Processing*, vol. 48, no. 10, pp. 2964–2972, Oct. 2000. 6

[15] J. O. Chapa and R. M. Rao, "Algorithms for designing wavelets to match a specified signal," *IEEE Transactions on Signal Processing*, vol. 48, pp. 3395–3406, Dec. 2000. 6

[16] I. Daubechies, "The wavelet transform, time-frequency localization and signal analysis," *IEEE Transactions on Information Theory*, vol. 36, pp. 961–1005, Sept. 1990. 6

[17] A. Graps, "An introduction to wavelets," *IEEE Computational Science and Engineering*, vol. 2, pp. 50–61, 1995. 6

[18] M. Sadiku, C. Akujuobi, and R. Garcia, "An introduction to wavelets in electromagnetics," *IEEE Microwave Magazine*, vol. 6. 6

[19] Z. He, Q. Qian, and Z. Wang, "Wavelet analysis and electric power market e-commerce," in *Proceedings of the Fourth International Conference on PDCAT'2003*, Aug.27–29, 2003, pp. 725–729. 7

[20] N. E. Huang, S. R. Long, M. C. Wu, H. H. Shih, Q. Zheng, N. C. Yen, C. C. Tung, and H. H. Liu, "The empirical mode decomposition and the hilbert spectrum for nonlinear and nonstationary time series analysis," in *Proceedings of the Royal Society*, vol. 454, London, 1998, pp. 903–995. 7, 29, 30

[21] N. E. Huang, M. Wu, W. Qu, S. R. Long, S. S. P. Shen, and J. E. Zhang, "Applications of hilbertchuang transform to non-stationary financial time series analysis," *Applied Stochastic Models in Business and Industry*, vol. 19, pp. 245–268, 2003. 7, 29

[22] Z. Yang, D. Qi, and L. Yang, "Signal period analysis based on hilbert-huang transform and its application to texture analysis," in *Proceedings of The Third International Conference on Image and Graphics 2004*, Dec.18–20, 2004, pp. 430–433. 7, 29

[23] R. Messler and M. Jou, "Review of control systems for resistance spot welding: past and current practices and emerging trends," *Science and Technology of Welding and Joining*, vol. 1, no. 1, pp. 1–9, 1996. 8, 41

[24] S. R. Lee, Y. J. Choo, T. Y. Lee, M. H. Kim, and S. K. Choi, "A quality assurance technique for resistance spot welding using a neuro-fuzzy algorithm," *Journal of Manufacturing Systems*, vol. 20, no. 5, pp. 320–328, 2001. 8, 9, 10

[25] Y. Cho and S. Rhee, "Primary circuit dynamic resistance monitoring and its application to quality estimation during resistance spot welding," *Welding Journal*, pp. 104–111, June 2002. 8, 9

[26] ——, "New technology for measuring dynamic resistance and estimating strength in resistance spot welding," *Measurement Science and Technology*, vol. 11, pp. 1173–1178, May 2000. 8, 9

[27] F. Garza and M. Das, "On real time monitoring and control of resistance spot welds using dynamic resistance signatures," in *Proceedings of the 44th IEEE 2001 Midwest Symposium on Circuits and Systems*, vol. 1, Aug. 14–17, 2001, pp. 41–44. 8, 45

[28] D. E. Destefan, "Calibration and testing facility for resistance welding current monitors," *IEEE Transactions on Instrumentation and Measurement*, vol. 45, no. 2, pp. 453–456, Apr. 1996. 8

[29] T. C. Manjunath, S. Janardhanan, and N. S. Kubal, "Simulation, design, implementation and control of a welding process using micro-controller," in *2004 5th Asian Control Conference*, vol. 2, July 20–23, 2004, pp. 828–836. 8

[30] K. Haefner, B. Carey, B. Bernstein, K. Overton, and M. D'Andrea, "Real time adaptive spot welding control," *Journal of Dynamic Systems, Measurement, and Control*, vol. 113, pp. 104–112, Mar. 1991. 8

[31] J. Xiao, "Intelligent monitoring of electrode condition in resistance spot welding process: A machine learning perspective," M. E.Sc. thesis, The University of Western Ontario, London, Ontario, Canada, 2004. 8

[32] W. Li, "Modeling and on-line estimation of electrode wear in resistance spot welding," *Journal of Manufacturing Science and Engineering*, vol. 127, no. 4, pp. 709–717, Nov. 2005. 8

[33] J. D. Brown, M. G. Rodd, and N. T. Williams, "Application of artificial intelligence techniques to resistance spot welding," *Ironmaking and Steelmaking*, vol. 25, no. 3, pp. 199–204, 1998. 8

[34] Z. Lin, Y. Zhang, G. Chen, and Y. Li, "Study on real-time measurement of nugget diameter for resistance spot welding using a neuro-fuzzy algorithm," in *Proceedings of the 21st IEEE IMTC 04*, vol. 3, May 18–20, 2004, pp. 2230–2233. 8

[35] W. Li, S. J. Hu, and J. Ni, "On-line quality estimation in resistance spot welding," *Journal of Manufacturing Science and Engineering*, vol. 122, no. 3, pp. 511–512, Aug. 2000. 8, 9

[36] S. C. Wang and P. S. Wei, "Modeling dynamic electrical resistance during resistance spot welding," *Journal of Heat Transfer*, vol. 123, no. 3, pp. 576–585, June 2001. 8

[37] M. Hao, K. A. Osman, D. R. Boomer, C. J. Newton, and P. G. Sheasby, "On-line nugget explusion detection for aluminum spot welding and weldbonding," *Journal of Materials and Manufacturing*, vol. 105, no. 5, pp. 209–218, 1996. 9

[38] A. G. Livshits, "Universal quality assurance method for resistance spot welding based on dynamic resistance," *Welding Journal*, vol. 76, no. 9, pp. 383s–390s, Sept. 1997. 9

[39] W. L. Roberts, "Resistance variations during spot welding," *Welding Journal*, vol. 30, no. 11, pp. 1004s–1019s, 1951. 9

[40] K. A. Osman, M. Hao, C. J. Newton, and D. Boomer, "A comprehensive approach to the monitoring of aluminium spot welding," in *AWS Detroit Section VII Sheet Metal Welding Conference*, Oct.9–11, 1996, pp. 1–18. 9, 45

[41] M. Hao, K. Osman, and N. Holden, "A data acquisition and signal processing system for aluminum spot welding," in *Proceedings of the 3rd Internationl Conference on Sheet Metal*, 1995. 10, 45

[42] F. Garza and M. Das, "Identification of time varying resistance during welding," in *IEEE IMTC Conference*, 2000, pp. 1534–1539. 10

[43] X. Chen and K. Araki, "Fuzzy adaptive process control of resistance spot welding with a current reference model," in *Proceedings of IEEE International Conference on Intelligent Processing Systems, 1997*, vol. 1, Oct.28–31, 1997, pp. 190–194. 10

[44] R. Hashemian, K. Golla, S. Kuo, and A. Joshi, "Design and construction of an active periodic noise canceling system using fpgas," *Circuits and Systems*, vol. 2, pp. 891–894, 1993. 13

[45] C. Fuller and A. von Flutow, "Active control of sound and vibration," *IEEE Control Systems Magazine*, vol. 15, pp. 9–19, 1995. 13

[46] F. B. Amara, P. Kabamba, and A. Ulsoy, "Adaptive band-limited disturbance rejection in linear discrete-time systems," in *Proceedings of the American Control Conference*, Seattle, WI, 1995, pp. 582–586. 14

[47] A. Kelkar and H. Pota, "Robust broadband control of acoustic duct," in *Proceedings of the 39th IEEE Conference on Decision and Control*, vol. 5, Sydney, 2000, pp. 4485–4490. 16

[48] F. B. Amara, R. Venugopal, P. Kabamba, A. Ulsoy, and D. Bernstein, "A comparison of two adaptive algorithms for disturbance cancellation," *Annual Reviews in Control*, vol. 21, pp. 67–78, 1997. 16, 19, 21

[49] V. K. Madisetti. (1995, Jan.) Signal decomposition. [Online]. Available: http://users.ece.gatech.edu/~vkm/nii/node35.html 28

[50] C. S. Ltd. Fourier spectral processing. [Online]. Available: http://www.clecom.co.uk/science/autosignal/help/Fourier_Spectral_Processing.htm 28

[51] Q. Zhang, "Time-varying frequency estimation and periodic disturbance cancellation," Ph.D Dissertation, The University of Western Ontario, London, Ontario, Canada, 2004. 29, 30, 35

[52] R. L. Stratonovich, *Topics in the Theory of Random Noise*. New York, NY: Gordon and Breach Science Publishers, 1967. 30

[53] Q. Zhang and L. Brown, "Designing of adaptive bandpass filter with adjustable notch for frequency demodulation," in *Proceedings of the 2003 American Control Conference*, vol. 4, Denver, 2003, pp. 2931–2936. 35, 102

[54] Spot welding. [Online]. Available: http://en.wikipedia.org/wiki/Resistance_spot_welding 41

[55] F. Garza and M. Das, "Identification of time-varying resistance during welding," in *Proceedings of the 17th IEEE Conference on Instrumentation and Measurement Technology*, vol. 3, May1–4, 2000, pp. 1534–1539. 42

[56] D. A. Ward and J. L. T. Exon, "Using rogowski coils for transient current measurements," *Engineering Science and Education Journal*, pp. 105–114, June 1993. 44

[57] S. Gedeon, C. Sorensen, K. Ulrich, and T. Eagar, "Measurement of dynamic electrical and mechanical properties of resistance spot welds," *Welding Journal*, pp. 378s–385s, Dec. 1987. 44, 46, 47

[58] D.Watney and G. Nagel, "Forms of dynamic resistance curves generated during resistance spot welding," in *Proceedings of the Sheet Metal Welding Conference*, Dearbom, MI, Oct. 1984, pp. 1–8. 47

[59] K. L. Su, *Analog Filters*. London, Glasgow: Chapman & Hall, 1996. 101

Appendix A

Responses of the Improved Adaptive Control System to Disturbances

Figure A.1: Response to a pure sinusoidal disturbance: $\omega_d = 100$ rad/sec

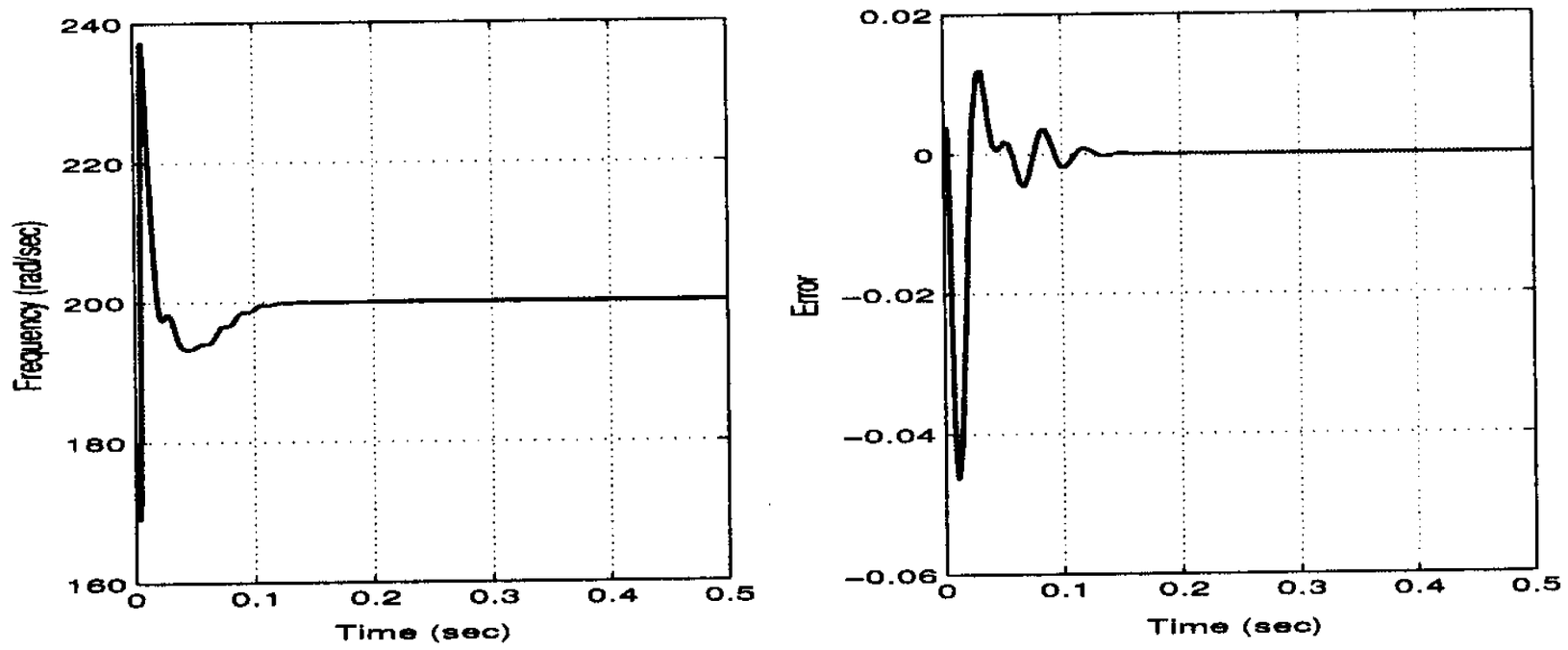

Figure A.2: Response to a pure sinusoidal disturbance: $\omega_d = 200$ rad/sec

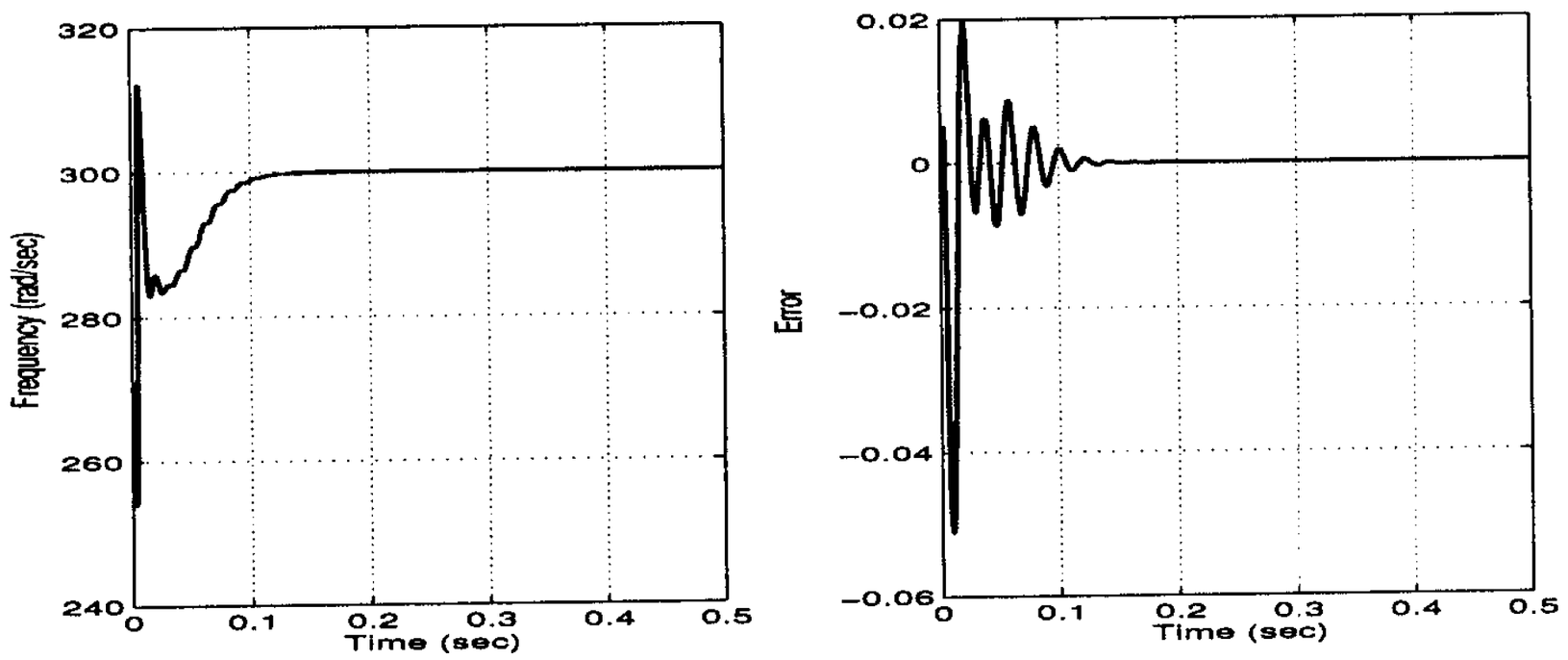

Figure A.3: Response to a pure sinusoidal disturbance: $\omega_d = 300$ rad/sec

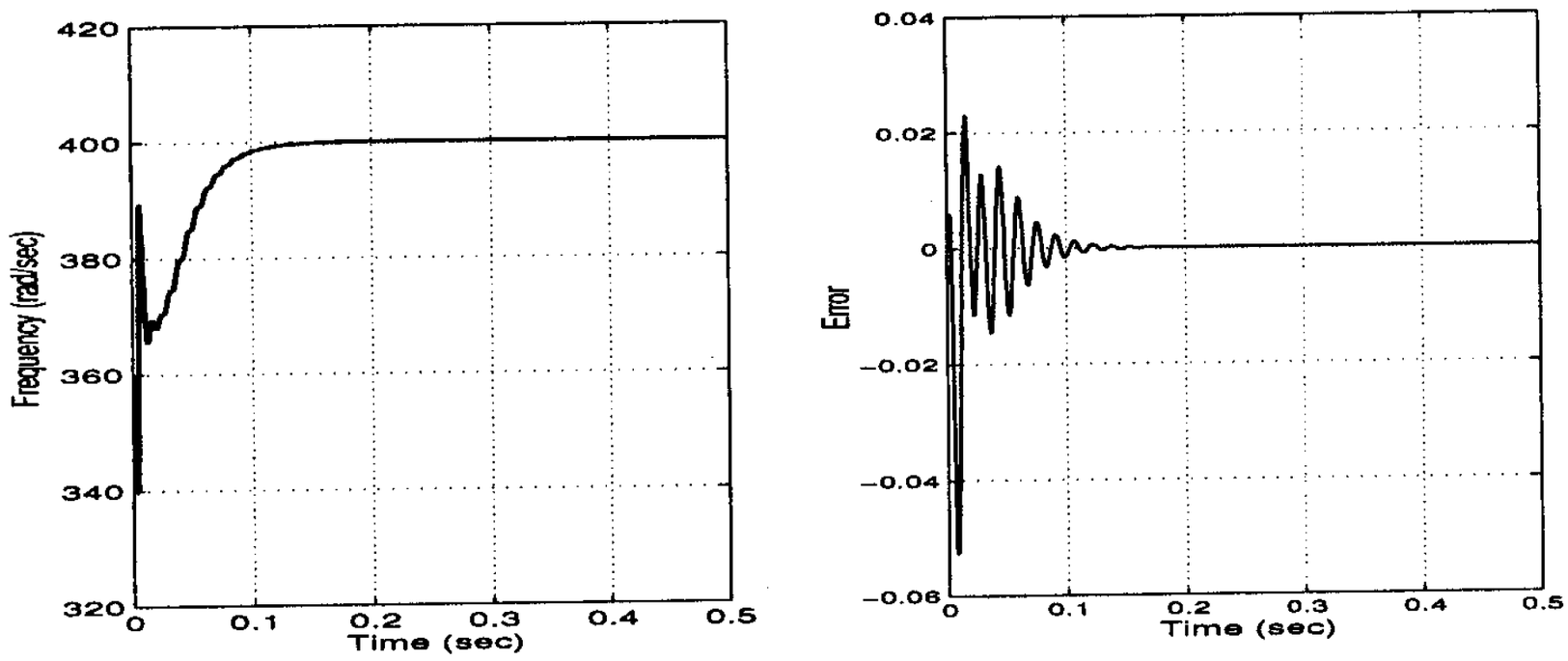

Figure A.4: Response to a pure sinusoidal disturbance: $\omega_d = 400$ rad/sec

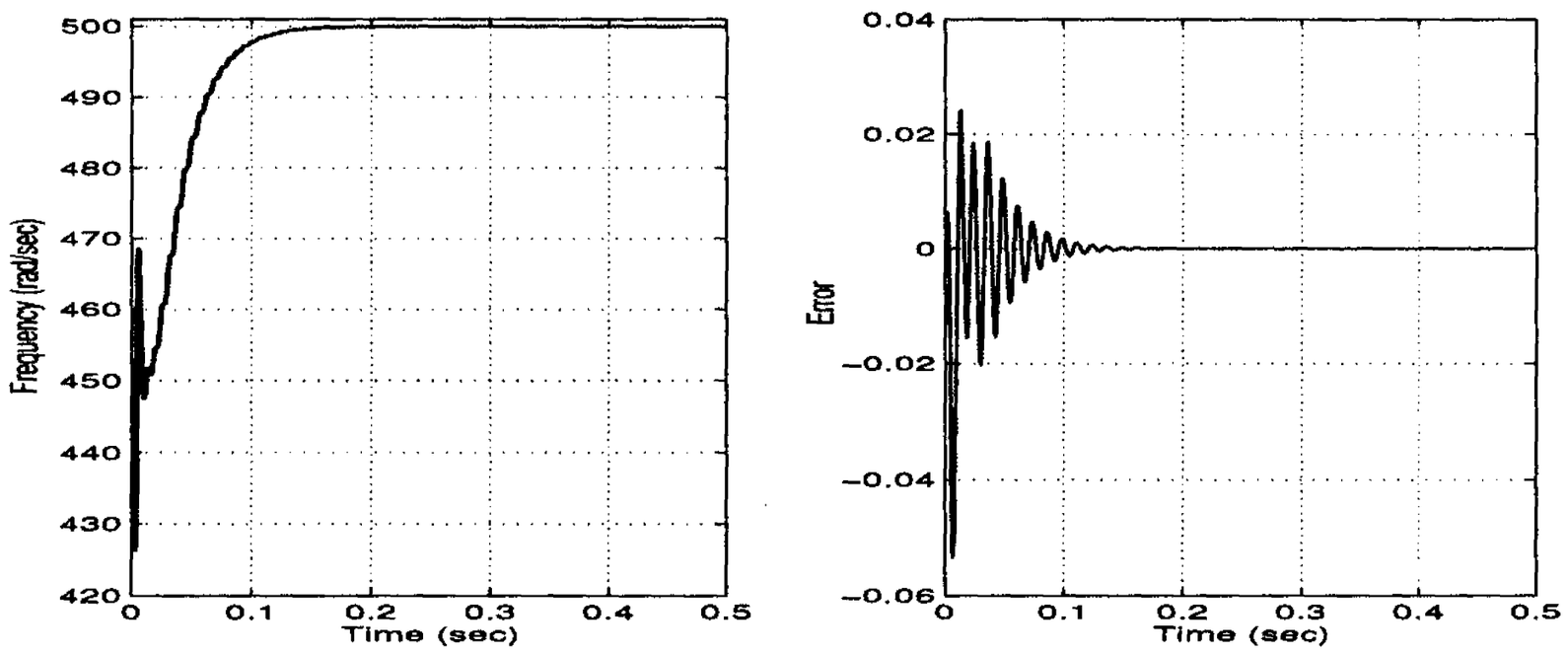

Figure A.5: Response to a pure sinusoidal disturbance: $\omega_d = 500$ rad/sec

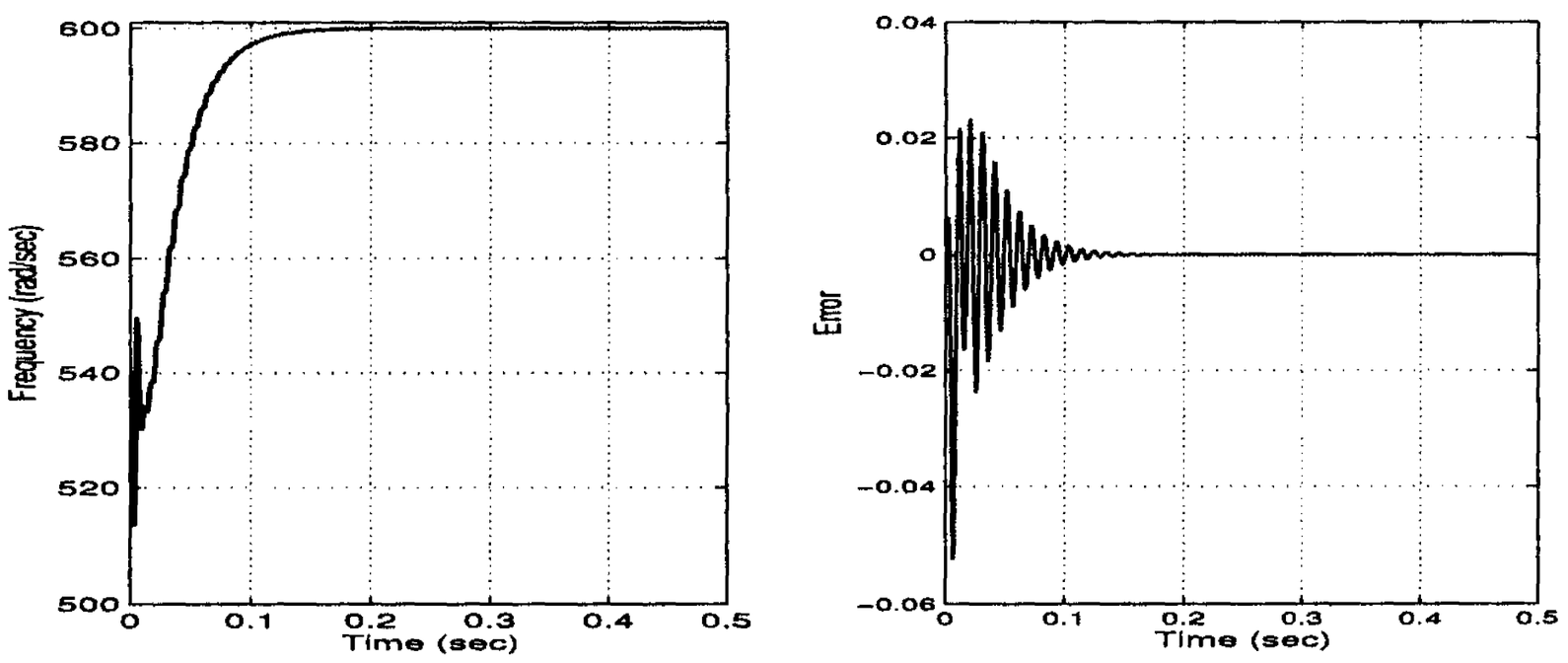

Figure A.6: Response to a pure sinusoidal disturbance: $\omega_d = 600$ rad/sec

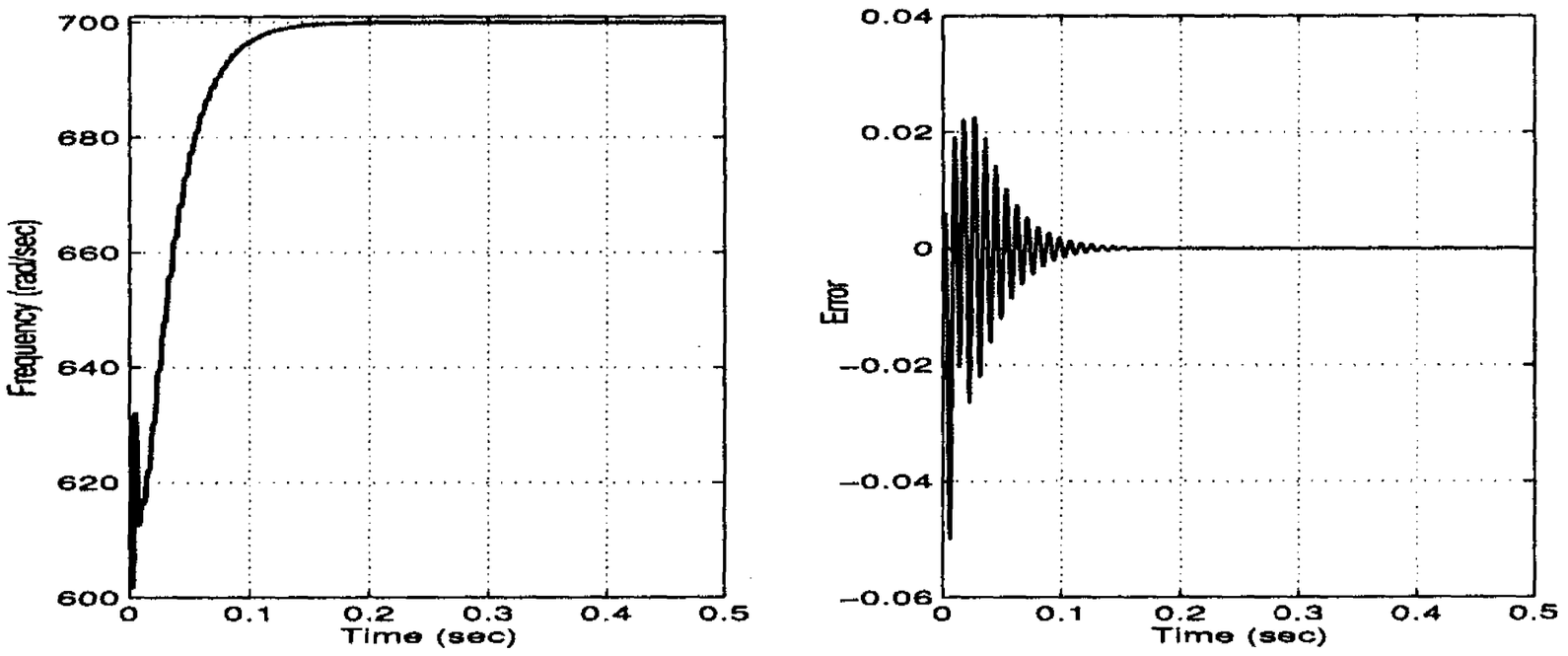

Figure A.7: Response to a pure sinusoidal disturbance: $\omega_d = 700$ rad/sec

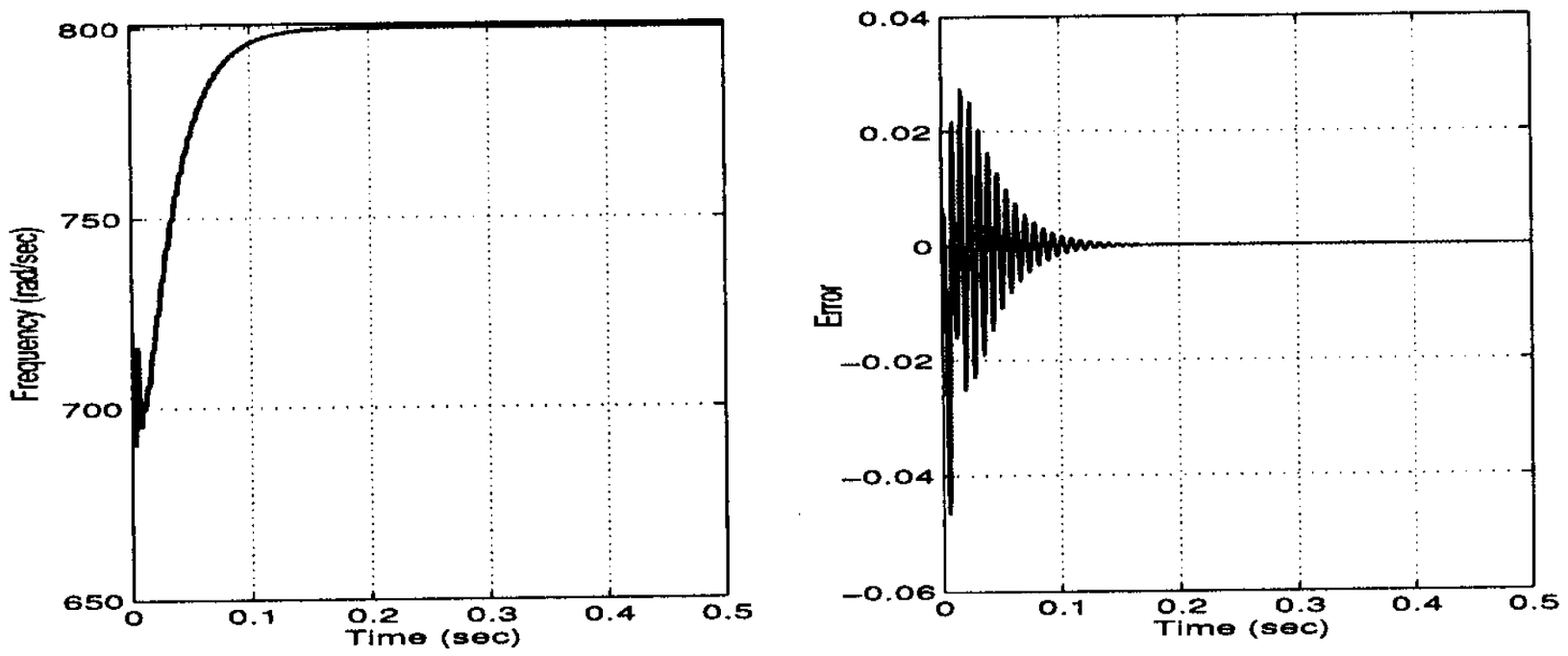

Figure A.8: Response to a pure sinusoidal disturbance: $\omega_d = 800$ rad/sec

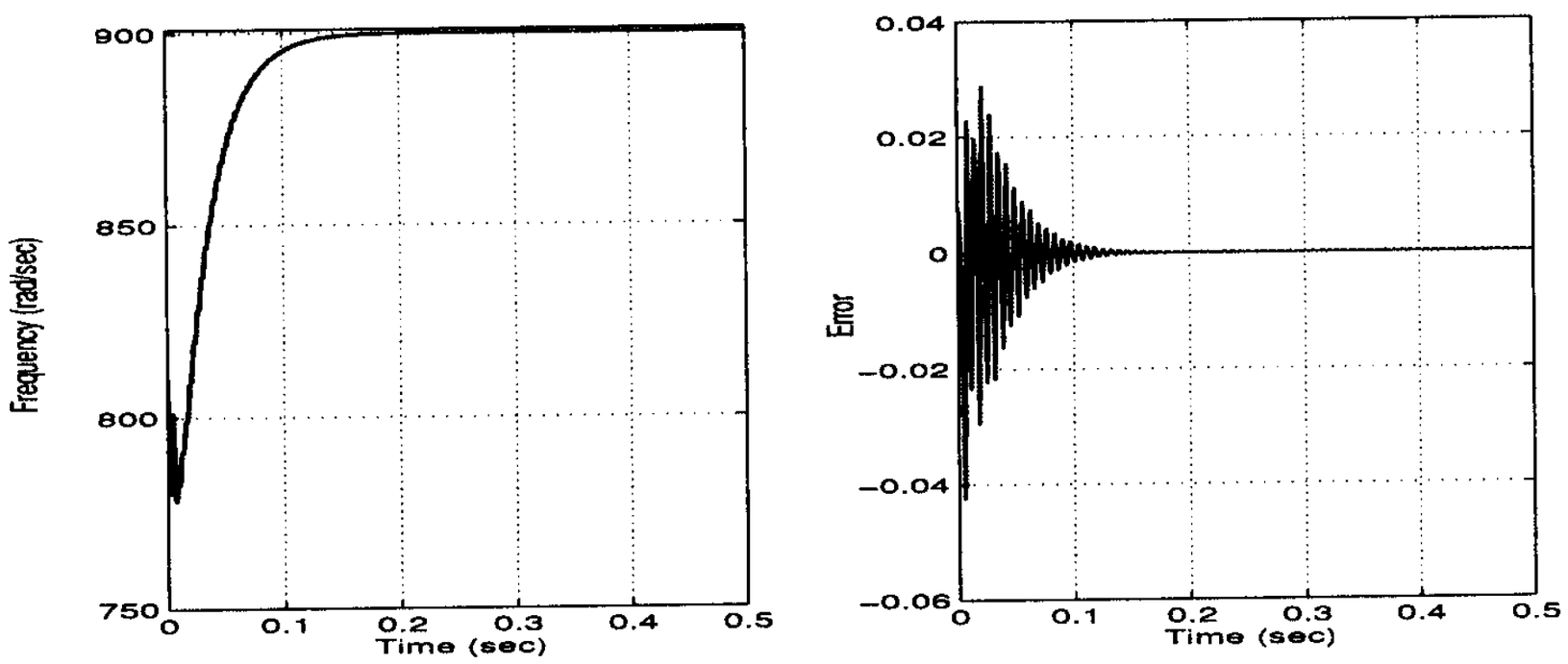

Figure A.9: Response to a pure sinusoidal disturbance: $\omega_d = 900$ rad/sec

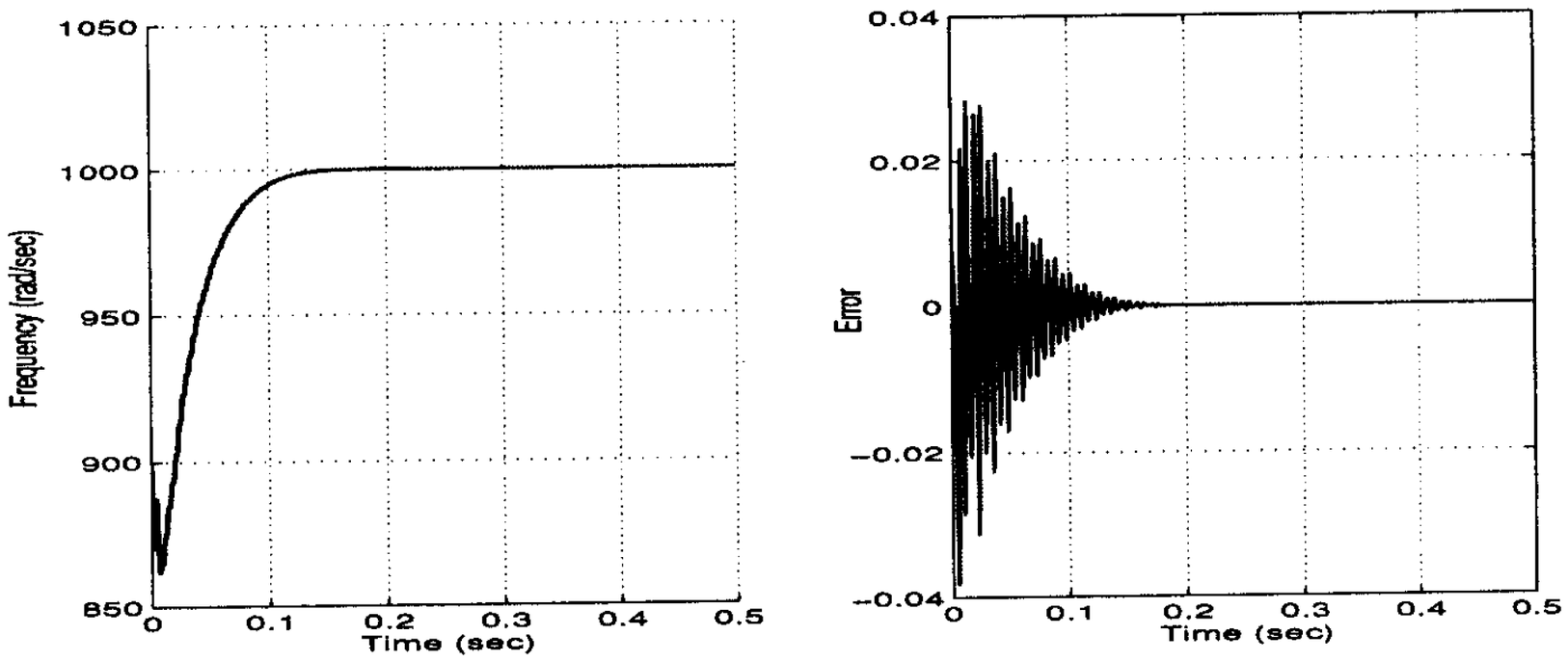

Figure A.10: Response to a pure sinusoidal disturbance: $\omega_d = 1000$ rad/sec

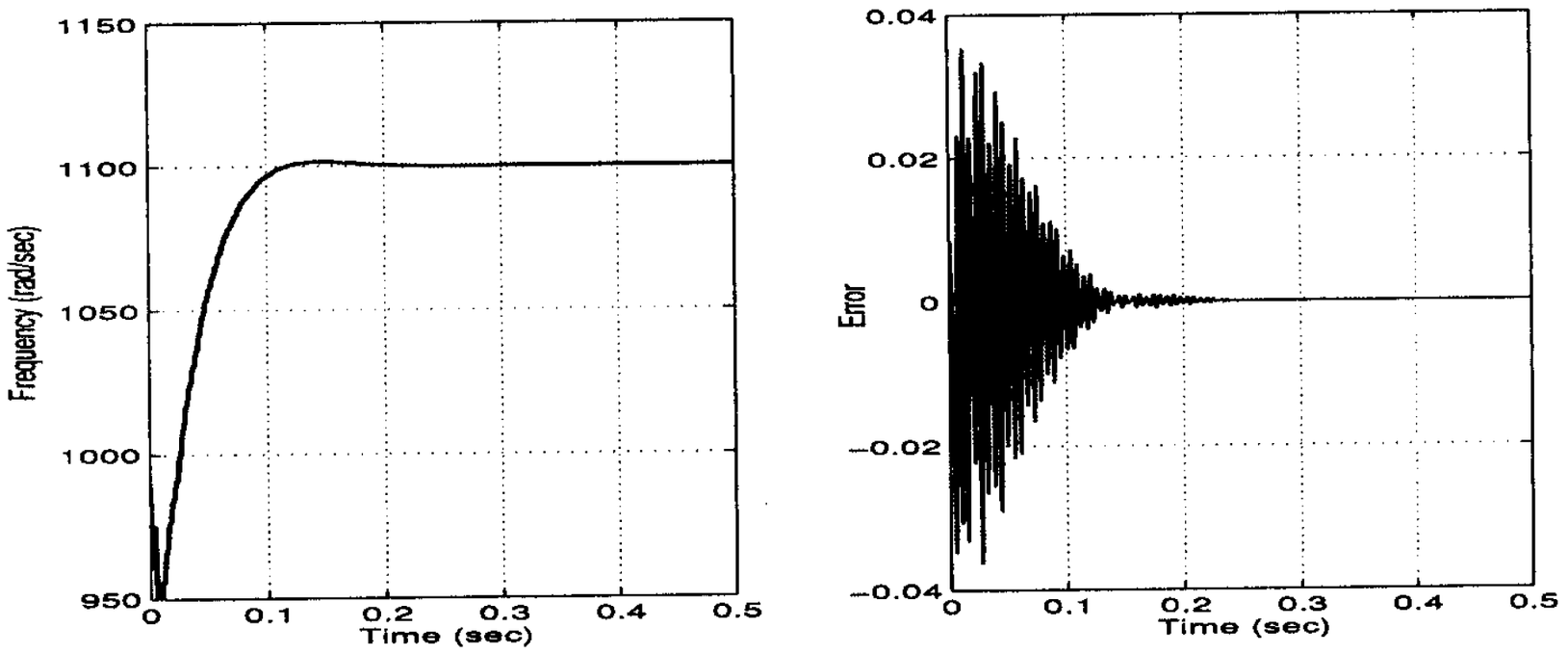

Figure A.11: Response to a pure sinusoidal disturbance: $\omega_d = 1100$ rad/sec

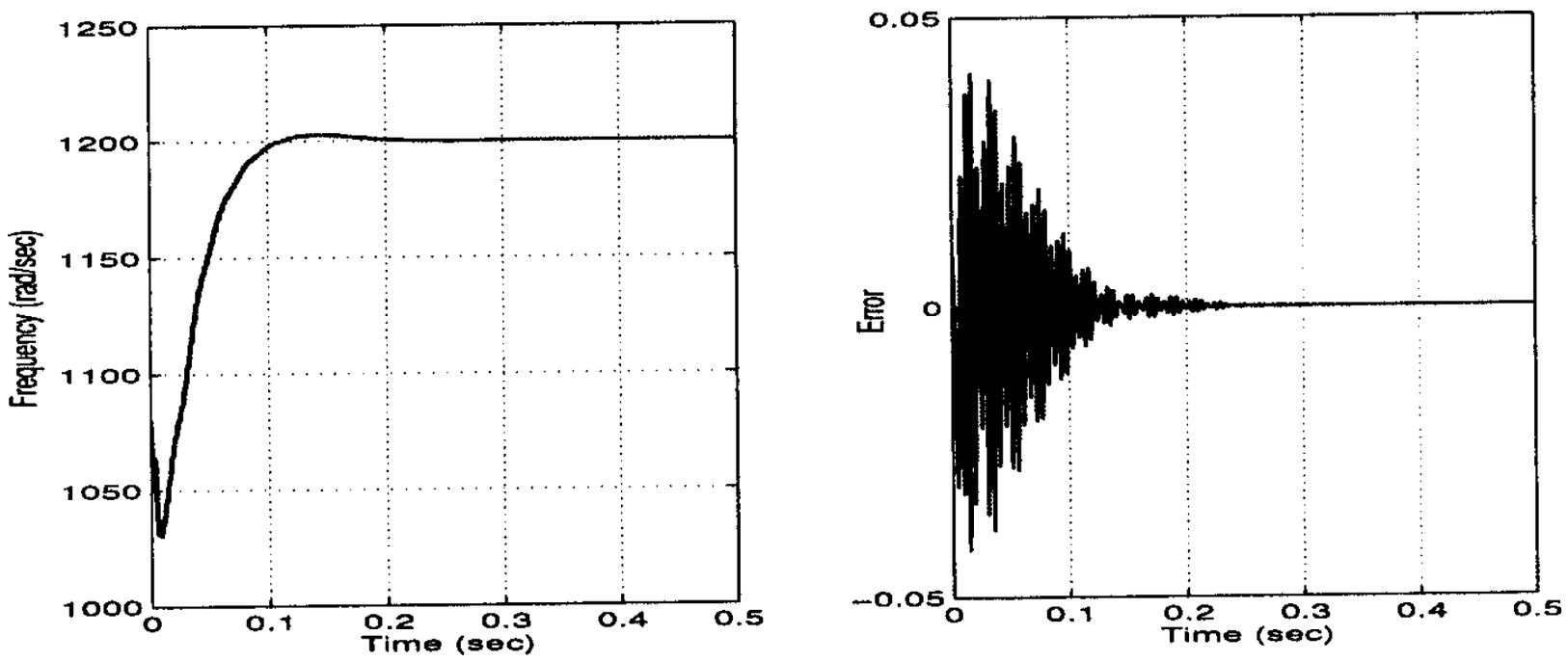

Figure A.12: Response to a pure sinusoidal disturbance: $\omega_d = 1200$ rad/sec

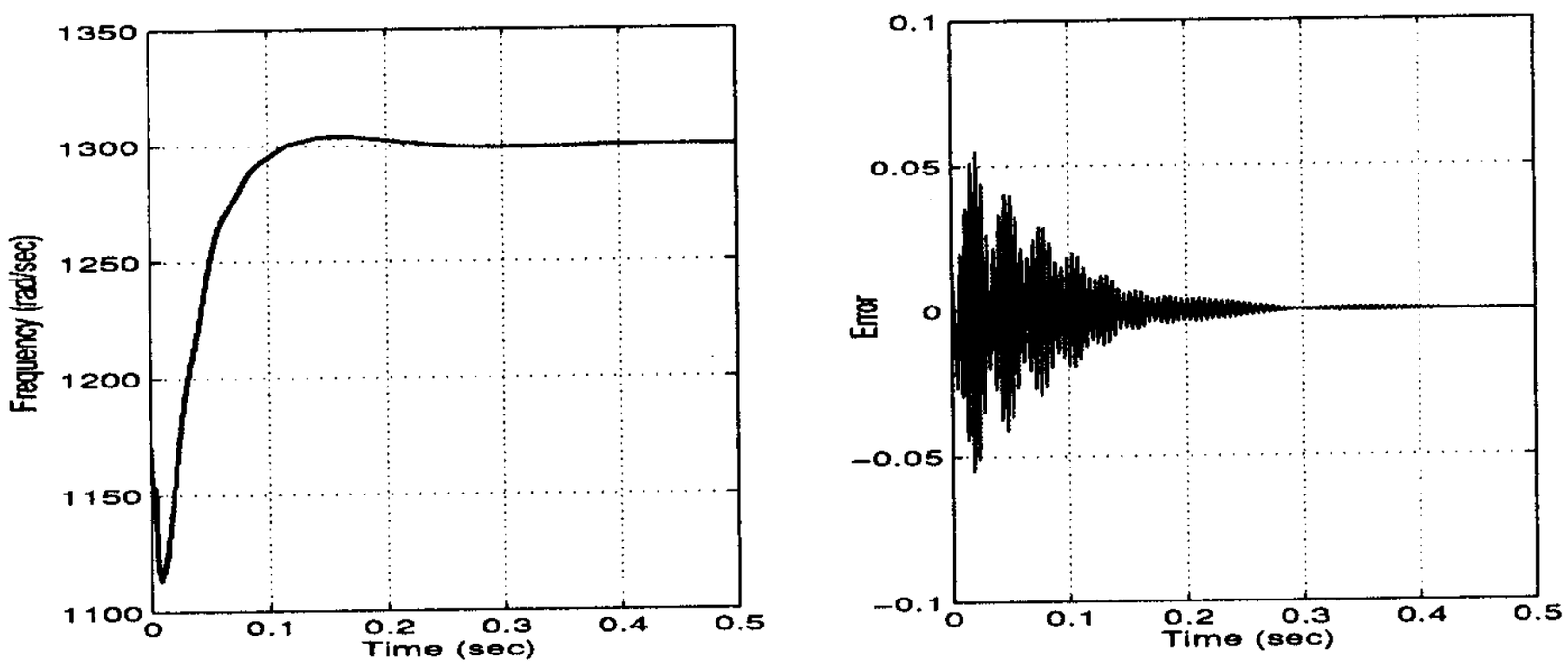

Figure A.13: Response to a pure sinusoidal disturbance: $\omega_d = 1300$ rad/sec

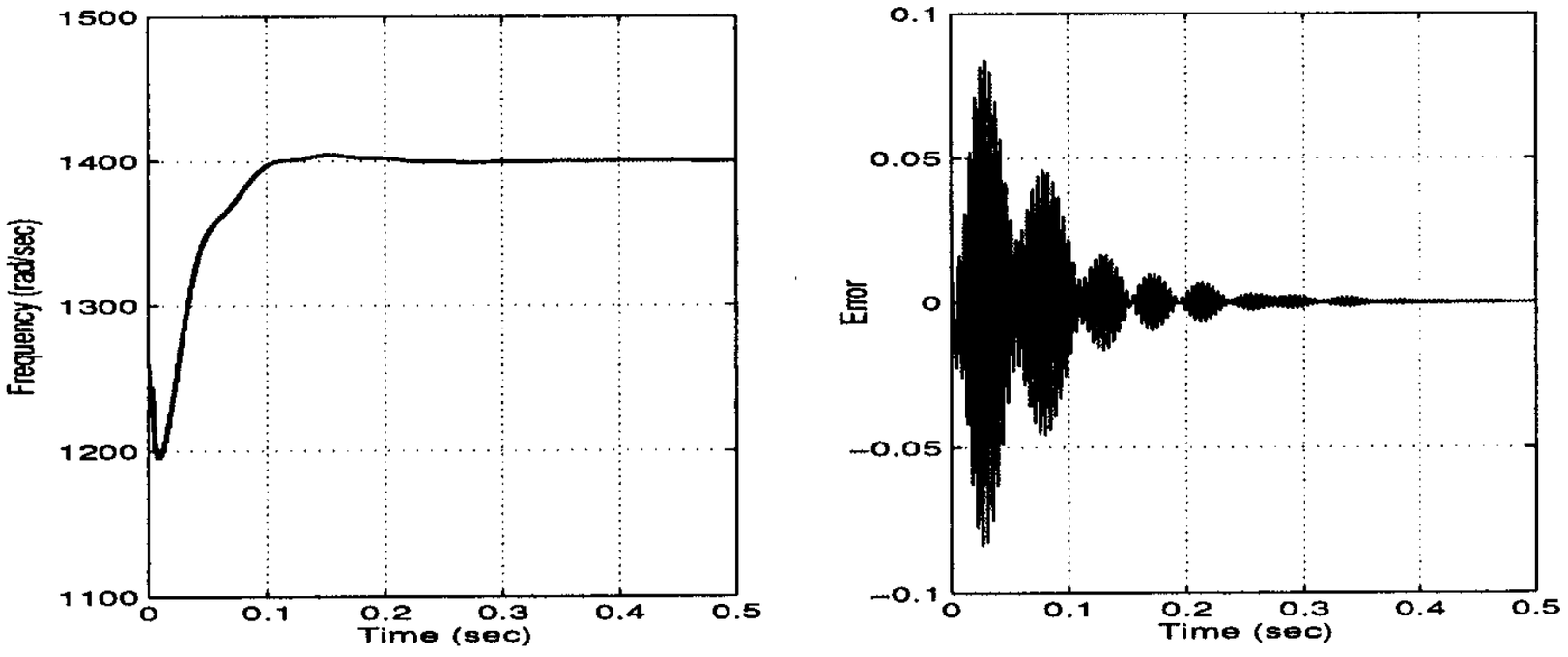

Figure A.14: Response to a pure sinusoidal disturbance: $\omega_d = 1400$ rad/sec

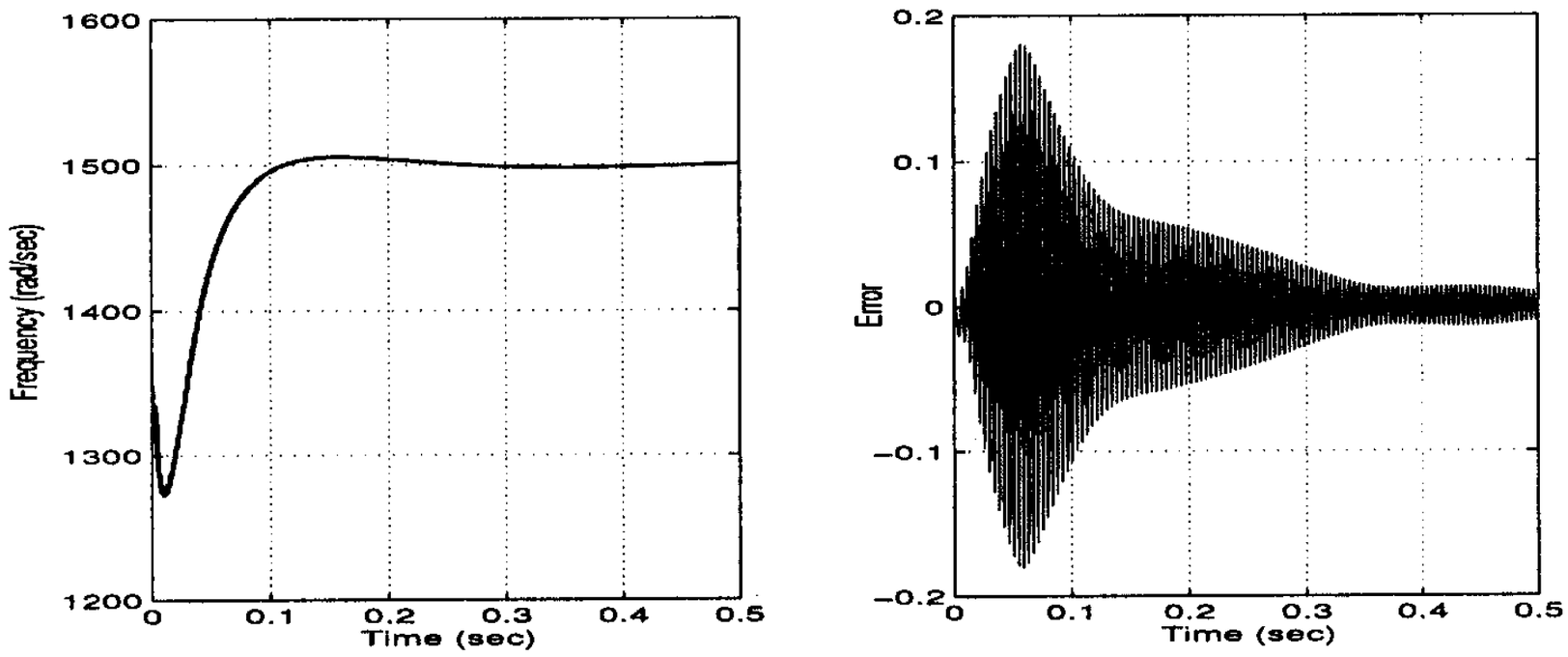

Figure A.15: Response to a pure sinusoidal disturbance: $\omega_d = 1500$ rad/sec

Appendix B

Analysis of RSW Circuit with Exponential Resistance

Fig. B.1 shows the equivalent electrical schematic of the secondary AC circuit in RSW. The dynamic resistance $R(t)$ here is exponential represented by $R_1 e^{-\sigma t}$. The solutions of the current $i(t)$ and the voltage $v(t)$ are given below.

The governing differential equation of this RL circuit is given by

$$L\frac{di(t)}{dt} + (R_c + R(t))i(t) = u(t) \qquad t > 0 \tag{B.1}$$

where $R(t) = R_1 e^{-\sigma t}, \quad u(t) = V_m \sin \omega t.$

Assuming $x(t) = i(t)$, (B.1) can be written in the form of

$$\dot{x}(t) = a(t)x(t) + b(t)u(t) \tag{B.2}$$

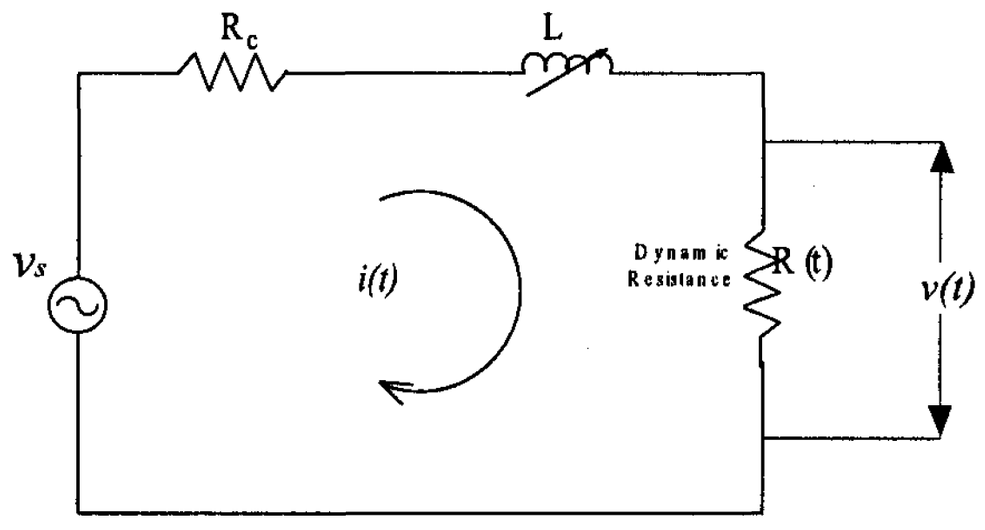

Figure B.1: Electrical circuit of the secondary loop in RSW with exponential resistance

where $a(t) = -\frac{1}{L}(R_c + R_1 e^{-\sigma t}), \quad b(t) = \frac{1}{L}.$

Linear system theory gives the complete solution of (B.2) as

$$x(t) = \Phi(t,0)x_0 + \int_0^t \Phi(t,\tau)b(\tau)u(\tau)d\tau \tag{B.3}$$

where

$$\Phi(t,0) = e^{\int_0^t a(\tau)d\tau} = e^{-\frac{1}{\sigma L}(\sigma R_c t - R_1(e^{-\sigma t}-1))} \tag{B.4}$$

$$\Phi(t,\tau) = e^{\int_\tau^t a(z)dz} = e^{-\frac{1}{\sigma L}(\sigma R_c (t-\tau) - R_1(e^{-\sigma t}-e^{-\sigma \tau}))} \tag{B.5}$$

Therefore,

$$\begin{aligned}
&\int_0^t \Phi(t,\tau)b(\tau)u(\tau)d\tau \\
&= \frac{V_m}{L}\int_0^t e^{-\frac{1}{\sigma L}(\sigma R_c(t-\tau) - R_1(e^{-\sigma t}-e^{-\sigma\tau}))}\sin\omega\tau d\tau \\
&= \frac{V_m}{j2L}\int_0^t e^{-\frac{1}{\sigma L}(\sigma R_c(t-\tau) - R_1(e^{-\sigma t}-e^{-\sigma\tau}))}\cdot(e^{j\omega\tau} - e^{-j\omega\tau})d\tau
\end{aligned} \tag{B.6}$$

Since

$$\begin{aligned}
&\int_0^t e^{-\frac{1}{\sigma L}(\sigma R_c(t-\tau) - R_1(e^{-\sigma t}-e^{-\sigma\tau}))}\cdot e^{j\omega\tau}d\tau \\
&= \frac{L(R_c + R_1 e^{-\sigma t} - j\omega L)}{(R_c + R_1 e^{-\sigma t})^2 + \omega^2 L^2}e^{j\omega t} - \frac{L(R_c + R_1 - j\omega L)}{(R_c + R_1)^2 + \omega^2 L^2}e^{-\frac{\sigma R_c t - R_1(e^{-\sigma t}-1)}{\sigma L}}
\end{aligned} \tag{B.7}$$

and

$$\int_0^t e^{-\frac{1}{\sigma L}(\sigma R_c(t-\tau)-R_1(e^{-\sigma t}-e^{-\sigma\tau}))} \cdot e^{-j\omega\tau} d\tau$$

$$= \frac{L(R_c+R_1e^{-\sigma t}+j\omega L)}{(R_c+R_1e^{-\sigma t})^2+\omega^2L^2}e^{-j\omega t} - \frac{L(R_c+R_1+j\omega L)}{(R_c+R_1)^2+\omega^2L^2}e^{-\frac{\sigma R_c t-R_1(e^{-\sigma t}-1)}{\sigma L}} \quad \text{(B.8)}$$

Substituting (B.7) and (B.8) into (B.6), we have

$$\int_0^t \Phi(t,\tau)b(\tau)u(\tau)d\tau$$

$$= \frac{(R_c+R_1e^{-\sigma t})V_m}{(R_c+R_1e^{-\sigma t})^2+\omega^2L^2}\sin\omega t - \frac{\omega LV_m}{(R_c+R_1e^{-\sigma t})^2+\omega^2L^2}\cos\omega t$$
$$+\frac{\omega LV_m}{(R_c+R_1)^2+\omega^2L^2}e^{-\frac{\sigma R_c t-R_1(e^{-\sigma t}-1)}{\sigma L}} \quad \text{(B.9)}$$

Substituting (B.4) and (B.9) into (B.3), we have the complete solution of $x(t)$

$$x(t) = e^{-\frac{1}{\sigma L}(\sigma R_c t-R_1(e^{-\sigma t}-1))}x_0 + \frac{\omega LV_m}{(R_c+R_1)^2+\omega^2L^2}e^{-\frac{\sigma R_c t-R_1(e^{-\sigma t}-1)}{\sigma L}}$$
$$+\frac{(R_c+R_1e^{-\sigma t})V_m}{(R_c+R_1e^{-\sigma t})^2+\omega^2L^2}\sin\omega t - \frac{\omega LV_m}{(R_c+R_1e^{-\sigma t})^2+\omega^2L^2}\cos\omega t \quad \text{(B.10)}$$

In this case, $x_0 = 0$, $x(t)$ can be simply represented by

$$x(t) = \frac{\omega LV_m}{(R_c+R_1)^2+\omega^2L^2}e^{-\frac{\sigma R_c t-R_1(e^{-\sigma t}-1)}{\sigma L}}$$
$$+\frac{(R_c+R_1e^{-\sigma t})V_m}{(R_c+R_1e^{-\sigma t})^2+\omega^2L^2}\sin\omega t - \frac{\omega LV_m}{(R_c+R_1e^{-\sigma t})^2+\omega^2L^2}\cos\omega t \quad \text{(B.11)}$$

Therefore, the time varying $i(t)$ is

$$i(t) = \frac{\omega LV_m}{(R_c+R_1)^2+\omega^2L^2}e^{-\frac{\sigma R_c t-R_1(e^{-\sigma t}-1)}{\sigma L}}$$
$$+\frac{(R_c+R_1e^{-\sigma t})V_m}{(R_c+R_1e^{-\sigma t})^2+\omega^2L^2}\sin\omega t - \frac{\omega LV_m}{(R_c+R_1e^{-\sigma t})^2+\omega^2L^2}\cos\omega t \quad \text{(B.12)}$$

When $t = 0$, the initial condition of $i(0)$ is

$$i(0) = 0 \tag{B.13}$$

When $t \to \infty$, in steady state, $i(\infty)$ is

$$i(\infty) = \frac{R_c V_m}{R_c^2 + \omega^2 L^2} \sin \omega t - \frac{\omega L V_m}{R_c^2 + \omega^2 L^2} \cos \omega t \tag{B.14}$$

The voltage across $R(t)$ is

$$v(t) = R_1 e^{-\sigma t} i(t) \tag{B.15}$$

Appendix C

Design of An Bandpass Filter with Notches

The desired internal model based estimation system for the dynamic resistance measurement behaves as a bandpass filter with notches.

C.1 Design of An Bandpass Filter $T_{bp}(s)$

The transfer function of the desired bandpass filter T_{bp} can be obtained from a normalized lowpass prototype filter T_{lp} by the transformation

$$T_{bp}(s) = T_{lp}(s)\Big|_{s=\frac{s^2+\omega_0^2}{BWs}} \tag{C.1}$$

where ω_0 is the center frequency, and BW is the bandwidth of the desired bandpass filter. In this thesis, the prototype of the normalized lowpass filter T_{lp} is chosen as a second order Chebyshev lowpass filter with 1-dB ripple given in [59] as

$$T_{lp}(s) = \frac{1.102510}{s^2 + 1.097734s + 1.102510} \tag{C.2}$$

The transfer function of the desired bandpass obtained by the transformation (C.1) is

$$T_{bp}(s) = \frac{1.102510BW^2s^2}{s^4 + c_1s^3 + c_2s^2 + c_3s + c_4} \tag{C.3}$$

where

$$\begin{aligned} c_1 &= 1.097734BW \\ c_2 &= 2\omega_0^2 + 1.102510BW^2 \\ c_3 &= 1.097734\omega_0^2 BW \\ c_4 &= \omega_0^4 \end{aligned} \tag{C.4}$$

C.2 Design of L, K for Single Tone Case

For a pure sinusoidal input, only one IM is incorporated in the estimation system. The system is designed to behave as a bandpass filter with a notch. The transfer function of a notch filter is in the form of

$$T_n = \frac{s^2 + \omega^2}{s^2 + 2\varepsilon\omega s + \omega^2} \tag{C.5}$$

where ε is a small real number and ω is the notch frequency.

Multiplying (C.3) and (C.5), the desired bandpass filter with a notch can be given by

$$\begin{aligned} T_{bpn} &= T_{bp} \times T_n \\ &= \frac{1.102510BW^2 s^2 (s^2 + \omega^2)}{(s^4 + c_1 s^3 + c_2 s^2 + c_3 s + c_4)(s^2 + 2\varepsilon\omega s + \omega^2)} \end{aligned} \tag{C.6}$$

We assume the tuning function $L(s)$ in the form of $L(s) = \frac{M(s)}{N(s)} = \frac{b_1 s^2}{s^4 + a_1 s^3 + a_2 s^2 + a_3 s + a_4}$ [53]. The transfer function of an IM is $\frac{K_2 s + K_1 \omega}{s^2 + \omega^2}$. Thus, the transfer function from the input $d(s)$ to the output $e(s)$ in Fig. 3.1 when $n = 1$ is

$$\begin{aligned} T_{de} &= \frac{L(s)}{1 + L(s)\left(\frac{K_2 s + K_1 \omega}{s^2 + \omega^2}\right)} \\ &= \frac{M(s)(s^2 + \omega^2)}{N(s)(s^2 + \omega^2) + M(s)(K_2 s + K_1 \omega)} \end{aligned} \tag{C.7}$$

By setting the numerators and denominators in (C.7) and (C.6) to be equal, we have

$$\begin{aligned} b_1 &= 1.102510BW^2 \\ a_1 &= c_1 + 2\varepsilon\omega \\ a_2 &= c_2 + 2\varepsilon\omega c_1 \\ a_3 &= c_3 + \frac{2\varepsilon c_4}{\omega} \\ a_4 &= c_4 \\ K_1 &= -2\varepsilon\omega\frac{\omega^2 c_1 - c_3}{b_1} \\ K_2 &= -2\varepsilon\frac{\omega^4 - \omega^2 c_2 + c_4}{\omega b_1} \end{aligned} \tag{C.8}$$

C.3 Design of L, K for Multiple-Tone Case

When the input signal contains harmonics, multiple IMs are incorporated in the estimation system. Correspondingly, the desired system is expected to behave as a bandpass filter with multiple notches. In this case, the transfer function of the closed-loop feedback system as shown in Fig. 3.1 is as follows

$$T_{de} = \frac{L(s)}{1 + L(s)\sum_{i=1}^{n}\left(\frac{K_{2i}s + K_{1i}\omega_i}{s^2 + \omega_i^2}\right)} \tag{C.9}$$

The desired bandpass notch filter has the form as

$$T_{bpn} = \frac{1.102510BW^2 s^2}{(s^4 + c_1 s^3 + c_2 s^2 + c_3 s + c_4)} \prod_{i=1}^{n} \frac{(s^2 + \omega_i^2)}{(s^2 + 2\varepsilon_i\omega_i s + \omega_i^2)} \tag{C.10}$$

By matching the coefficients of the numerators and denominators in (C.9) and (C.10), we can obtain the unique solutions of b_1 and $a_k (k = 1, \cdots, 4)$ for $L(s)$, and the feedback gains

$(K_{1i},\ K_{2i})(i = 1, \cdots, n)$ for each IM.

C.4 Design of $L,\ K$ for Nonperiodic Input

When the input signal is nonperiodic as described in section 3.3, Fig. 3.2 is applied to estimate the dynamic resistance in RSW. In this case, a zero will be added in the desired estimation system which was previously designed as a bandpass filter with notches. The corresponding transfer function is

$$T_{bpn} = \frac{1.102510BW^2 s^2(s+\sigma)}{(s^4 + c_1 s^3 + c_2 s^2 + c_3 s + c_4)} \prod_{i=1}^{n} \frac{(s^2 + \omega_i^2)}{(s^2 + 2\varepsilon_i \omega_i s + \omega_i^2)} \tag{C.11}$$

Accordingly, the form of the tuning function $L(s)$ is modified as $L(s) = \frac{M(s)}{N(s)} = \frac{b_1 s^2}{s^3 + a_1 s^2 + a_2 s + a_3}$.

The transfer function of the closed-loop feedback system as shown in Fig. 3.2 is then given by

$$T_{de} = \frac{L(s)}{1 + L(s)\left(\frac{K_p}{s+\sigma} + \sum_{i=1}^{n}\left(\frac{K_{2i}s + K_{1i}\omega_i}{s^2 + \omega_i^2}\right)\right)} \tag{C.12}$$

By matching the coefficients of the numerators and denominators in (C.12) and (C.11), we can obtain the unique solutions of b_1 and $a_k(k = 1, \cdots, 3)$ for $L(s)$, and the feedback gains K_p and $(K_{1i},\ K_{2i})\ (i = 1, 2, \cdots, n)$ for each IM.

Appendix D

Relevant Data Signals and Peak Values

The following relevant data signals and corresponding peaks values were extracted from the shop-floor data after noise filtration using FFT techniques.

Primary Current:	142.56 A
Secondary Current:	16 kA
Primary Voltage:	462 V
Secondary Voltage:	4.125 V
Measured Tip Voltage:	1.42 V
Corrected Tip Voltage:	1.23 V
Current Derivative:	2.55 V
R_c:	161.5 $\mu\Omega$
L:	0.5675 μH
Turn Ratio:	112

Appendix E

MATLAB Code Listing

The gain of the state feedback K and the coefficients of the transfer function for the tuning function L are calculated based on the desired estimation system behaves as a bandpass filter with notches. Each harmonic contained in the input measured signal corresponds to one internal model in the estimation system. As an example, following MATLAB codes give the solutions of state feedback gain and tuning function as well as all the initial conditions for the internal models and the integrators incorporated in the system.

```
%%%%%%% Generate synthesized resistance %%%%%%%%%%
res=[70e-6 67e-6 62e-6 57e-6 52e-6 49e-6 46e-6 45e-6 44e-6
     44e-6 45e-6 47e-6 51e-6 57e-6 64e-6 68e-6 69e-6 70e-6
     70e-6 70e-6 70e-6];
t1=(0:.01:0.2); p=polyfit(t1,res,3); res2=polyval(p,t1);
y=interpft(res2, 25*200+1); t2=0:1/25000:.2; pf=polyfit(t2,y,5);
r=polyval(pf,t2);
%%%%%% Generate the measured signals from the model %%%%%%%%
sim('siggen_pure')
%%%%%%%%%%%% Parameters setup %%%%%%%%%%%%%%%%
R0=rtip(1); %R0=7.5816e-005
Rc=161.5e-6; L=0.5675e-6; R=Rc+R0; v_1=4.125; Ksc=.5556*0.8333e-6;
w=2*pi*60; phi=w*L/(R0+Rc);
Ieo_1=v_1/sqrt((R0+Rc)^2+(w*L)^2)*sin(-atan(phi));
Ideo_1=v_1/sqrt((R0+Rc)^2+(w*L)^2)*cos(-atan(phi));
```

```
%%%%%%%%%%%%% Designed a bandpass filter %%%%%%%%%%%%%%%%%%
w0=2*pi*80; ep=.75; BW=2*pi*160; c1=1.097734*BW;
c2=2*w0^2+1.102510*BW^2; c3=1.097734*BW*w0^2; c4=w0^4;
%%%%%%%%%%%%% Coefficients of L(s) %%%%%%%%%%%%%%%%%%
b1=1.102510*BW^2; a1=-(-c1*L-2*ep*w*L+R)/L;
a2=L*(2*c4*ep*R+c3*w*R-c4*L*w)/(R^2*w); a3 = c4*L/R;
%%%%%%%%%%%%%%%% Kp and K %%%%%%%%%%%%%%%%%
Kp=(2*L^4*c3*ep*w*R^2+L^4*c2*w^2*R^2+R^6-2*L^5*w*c4*ep*R
    -L^5*w^2*c3*R+L^6*w^2*c4-L^3*c1*w^2*R^3+L^2*R^4*w^2
    +2*R^4*w*c1*ep*L^2-2*R^5*w*ep*L-2*R^3*w*L^3*c2*ep
    +R^4*c2*L^2-R^3*L^3*c3+R^2*L^4*c4
    -R^5*c1*L)/(b1*L^2*R^2*(w^2*L^2+R^2));
K(1)=-2*w*L*ep*(-c2*w^2*L+w^2*c1*R+L*w^4-c3*R+c4*L)
     /(b1*(w^2*L^2+R^2));
K(2)=-2*L*ep*(-c2*w^2*R+w^4*R+c4*R-w^4*L*c1+c3*w^2*L)
     /(b1*w*(w^2*L^2+R^2));
K(1)=K(1)/w;
%%%%%%%%%%%%%% Initial values %%%%%%%%%%%%%%%%%%
x1_0=-(K(2)*Ideo_1-Ieo_1*K(1))/(K(1)^2+K(2)^2);
x2_0=(K(2)*Ieo_1+Ideo_1*K(1))/(K(1)^2+K(2)^2);
x1v_0=(Ieo_1*R0*K(1)+Ksc*w*Ideo_1*K(1)-Ideo_1*R0*K(2)
      +Ksc*w*Ieo_1*K(2))/(K(2)^2+K(1)^2);
x2v_0=-(-K(1)*Ideo_1*R0+K(1)*Ksc*w*Ieo_1-K(2)*Ieo_1*R0
     -K(2)*Ksc*w*Ideo_1)/(K(2)^2+K(1)^2);
numim=1;
```

The states of the internal models in the algorithm provide the instantaneous Fourier series representation of the current and voltage signal. The MATLAB codes for calculation the tip voltage magnitude and the dynamic resistance are given as follows.

```
for k=1:numim
    sx(:,2*k-1)=K(2*k-1)*u(:,2*k-1)+K(2*k)*u(:,2*k);
    sx(:,2*k)=-K(2*k)*u(:,2*k-1)+K(2*k-1)*u(:,2*k);
    sxv(:,2*k-1)=K(2*k-1)*uv(:,2*k-1)+K(2*k)*uv(:,2*k);
    sxv(:,2*k)=-K(2*k)*uv(:,2*k-1)+K(2*k-1)*uv(:,2*k);
    smagi(:,k)=sqrt(sx(:,2*k-1).^2+sx(:,2*k).^2);
    stip(:,k)=dot([sx(:,2*k-1) sx(:,2*k)],
                  [sxv(:,2*k-1) sxv(:,2*k)],2)./smagi(:,k);
    sdr(:,k)=stip(:,k)./smagi(:,k);
end
%%%%%%%%%%%% ESTIMATE OF RESISTANCE %%%%%%%%%%%%
sdr(:,numim+1)=nanmean(sdr(:,1:numim)')';
figure
plot(tout,rtip,tout,sdr(:,1),':m')
%%%%%%%%%%%% OVERALL TIP VOLTAGE MAGNITUDE %%%%%%%%%%%%
tip=0;
for n=1:numim
    tip=tip+stip(:,n).^2;
end stip(:,numim+1)=sqrt(tip); figure
plot(tout_rl,vtip_mag,tout,stip(:,numim+1),'--r')
```